A STUDY OF THE PROCESS $e^+e^- \rightarrow$ HADRONS AT HIGH ENERGIES.

by

MOURAD DHINA

D. E. S, Université des Sciences et de la Technologie d'Alger, Algeria
(June 1983)

M.S.(Physics), Massachussets Institute of Technology
(December 1985)

Submitted to the Department of Physics in partial
fulfillment of the requirements
for the degree of

DOCTOR OF PHILOSOPHY

at the

MASSACHUSETTS INSTITUTE OF TECHNOLOGY

April 1987

Signature of Author_____
Department of Physics, April 1987

Certified by____
Min Chen, Thesis supervisor

Accepted by____
George F. Koster
Chairman, Department Committee

A Study of the process $e^+e^- \rightarrow$ hadrons

at high energies.

by

MOURAD DHINA

Submitted to the Department of Physics on April 30, 1987
in partial fulfillement of the requirements of the degree of
Doctor of Philosophy.

ABSTRACT

This thesis is devoted to the study of hadronic final states in e^+e^- annihilations over the center of mass energy range $22\ GeV \leq \sqrt{s} < 47\ GeV$. We use two independent methods to determine the strong coupling constant of QCD: the Asymmetry of the energy-energy correlations function, and the planar triple energy correlations function. Our resutlts for the first method are:

$$\alpha_s(35\ GeV) = 0.129 \pm 0.004 \pm 0.012,$$

$$\alpha_s(44\ GeV) = 0.108 \pm 0.007 \pm 0.010\ ;$$

whereas the second method yields:

$$\alpha_s(35\ GeV) = 0.137 \pm 0.004 \pm 0.015,$$

$$\alpha_s(44\ GeV) = 0.108 \pm 0.007 \pm 0.012.$$

We observe that the largest source of systematic errors is due to the fragmentation process for which a consistent theory is yet to be developed. Using the variation of α_s with the center of mass energy, we determine the QCD scale parameter Λ in the minimal subtraction scheme:

$$\Lambda_{\overline{MS}} = 100 \pm 20 \,^{+80}_{-52} \; MeV.$$

Combining our results with those from lower energy experiments we conclude that a running strong coupling constant is strongly favored over a constant strong coupling constant.

Finally, we present tests of cluster fragmentation models. We show that such models give better fits to the data when used with fixed order matrix element QCD calculations than with LLA calculations (parton showers).

Thesis Supervisor: Min Chen
Title: Professor of Physics

Acknowledgement

It is a pleasure to thank my thesis advisor, Professor Min Chen, for his help, guidance and advice during all my graduate studies at MIT. I have learned a lot about high energy physics while working with him. My thanks also go to Prof Samuel C. C. Ting for his help and support.

I also thank Profs. U. Becker and L. Rosenson for their careful reading of this thesis and their numerous and useful comments. I have greatly benefited from discussions with Prof. J. Branson.

This work would not have been possible without the participation of all the members of the MarkJ collaboration. In particular, I want to thank L. Garrido, J. Rose, J. Schug and H. Stone for the many discussions we had. I thank P. Slade and J. Donahue for their help and support.

The continuous support of the Algerian Ministry for Higher Education is greatly appreciated. Last, but not least, I thank my family members for their patience and support during this work.

Contents

Chapter 1 INTRODUCTION 7

Chapter 2 Theoretical Concepts 9

2.1 Introduction 9

2.2 The Fields and Lagrangian of QCD 10

2.3 QCD and e^+e^- jets 12

2.4 Fragmentation 16

2.4.1 Independent Jet Fragmentation (IJ) 16

2.4.2 The Color String Model (Lund) 17

2.4.3 Cluster models 17

Chapter 3 The Experiment 19

3.1 Petra 19

3.2 The Mark-J detector 20

Chapter 4 Data Manipulation 23

4.1 Introduction 23

4.2 Online data reduction 24

4.3 Offline event selection 25

4.4 Detector calibration 27

Chapter 5 Measurement of the Strong Coupling Constant 30

5.1 Implementation of the models 30

5.1.1 MarkJ 2^{nd} order QCD calculation 31

5.1.2 Detector Simulation 32

5.2 Choice of variables 33

5.2.1 Energy-Energy Correlations 35

5.2.2 Triple Energy Correlations 36
5.3 Determination of α_s from the ASY function 38
5.4 Determination of α_s from the PTC function 42
5.5 Comparison between the two methods 45
5.6 Running of α_s 46
Chapter 6 Conclusions 48
Appendix A Comparison with other experiments 51
Appendix B Tests of Cluster Models 54
B.1 LLA Parton showers 55
B.2 String evolution and Hadronization 56
B.3 Tests of the Model 57
B.3.1 LLA+CIT Model 57
B.3.2 ERT+CIT Model 58
B.4 Conclusions 58

Chapter 1

INTRODUCTION

In the last decade, our understanding of the nature of strong interactions has increased considerably. Indeed, we have now a wealth of data, from both collider and fixed target experiments, that clearly support our best candidate for a theory of strong interactions: Quantum Chromodynamics (QCD). From the conceptual point of view, QCD provides a comprehensive and well defined theory of the strong force. This is mainly due to its fullfilment of the two basic requirements of a field theory: *Renormalizability* and *Local gauge invariance.*

However, unlike Quantum Electrodynamics (QED) or the Glashow-Weinberg-Salam (GSW) theory of electromagnetic and weak forces, QCD has not yet yielded unambiguous quantitative predictions which can be confronted with experimental data. This has its origin in the hierarchal relationship between observed particles (mesons and baryons) and the fundamental constituents (quarks and gluons); in other words, the basic fields of the QCD lagrangian *are not directly observed in nature.* They undergo a hadronization process, not described by QCD, that confines them into hadrons, see Fig. 1.1.

QCD, as a field theory, has basically only one paramater which determines the strength of quark-gluon and gluon-gluon interactions. At large momentum transfers, QCD exhibits the so-called *asymptotic freedom* or vanishing of the coupling constant. This is precisely what makes QCD pertubative calculations legitimate. One should bear in mind that even for nowadays experiments, for which the momentum transfer is of the order of tens of GeV's, the strong coupling constant, commonly noted α_s, is big (compared, e.g to $\alpha_{QED} = \frac{1}{137}$) with a value of ~ 0.1. In perturbative series, this implies that high order terms are important. To date, many complete 2^{nd} order QCD calculations exist, as well as semi-phenomenological hadronization models.

It is the goal of this thesis, to use high energy e^+e^-collisions data, taken with the MarkJ detector at PETRA, to make measurements of α_s at various center of mass energies, as well as a systematic study of the dependence of such measurements on different QCD calculations and hadronization models.

The thesis is organized as follows. In chapter 2 we present the basic theoretical concepts necessary for this work. Chapter 3 and 4 are devoted to a description of the experimental set-up, data manipulation and event selection. In Chapter 5, we determine the strong coupling constant α_s. A conclusion of this work is given in Chapter 6.

We compare our results with other experiments in Appendix A. Finally, we present various tests of cluster fragmentation models in Appendix B.

Chapter 2

Theoretical Concepts

2.1 Introduction

Quarks were introduced by Gell-Mann and Zweig [2-1], as spin $\frac{1}{2}$ basic building blocks of the numerous strongly interacting particles discovered between the 1940s and 1960s. This followed the suggestion by Gell-Mann and Ne'eman (Eightfold way) [2-2] that hadrons with the same spin and parity were related to each other through a global SU(3) symmetry, in the same fashion as the SU(2) isospin symmetry was invoked to explain the electric charge independence of the strong force.

Quarks were subsequently identified with the *partons* observed in the deep inelastic lepton-nucleon scattering experiments [2-3] performed at SLAC. These experiments established that quarks carried the expected spin and fractional charges. Furthermore, the observed *scale invariance* [2-4] showed that, within the energy scale being probed, quarks

were point-like. However, this picture has been confronted with a serious dilemma: it was able to predict the existence of a new particle Ω^-, but violated at the same time one of the fundamental laws of physics, the Pauli principle. Ω^- was a baryon built from 3 quarks being in the same quantum state. To solve this puzzle, a new degree of freedom for hadrons was postulated: *color* [2-5]. Irrefutable experimental evidence for color came from measurements of the decay rate of $\pi^\circ \rightarrow 2\gamma$, and the total hadronic cross section in e^+e^-annihilations. These data show that there are 3 color states, commonly referred to as: Red, Blue and Green. At present, 5 quarks flavors, u(up), d(down), s(strange), c(charm), b(bottom) have been discovered. In table 2.1 we show the quantum numbers of quarks.

Quarks	I	I_3	s	c	b	Q	B
u	1/2	1/2	0	0	0	2/3	1/3
d	1/2	-1/2	0	0	0	-1/3	1/3
s	0	0	-1	0	0	-1/3	1/3
c	0	0	0	1	0	2/3	1/3
b	0	0	0	0	-1	-1/3	1/3

Table 2.1 Isospin,strangeness,charm,bottomness,charge,baryon number of quarks.

In addition, massless vector particles, called *gluons*, are believed to hold the quarks together inside hadrons. There are 8 types of gluons which are flavor neutral and do not participate in electro-weak interactions. The observation of 3-jet events [2-6],[2-7] at Petra was a direct evidence for gluons, and at the same time a major success of QCD.

2.2 The Fields and Lagrangian of QCD

QCD [2-8] is a Yang-Mills [2-9] (local) gauge theory based on the $SU(3)_{color}$ symmetry: it describes the interaction of a triplet of colored quarks and an octet of vector gluons. Quark fields Ψ_α^{ar}, carry a Dirac index (α), a color label (a) and a flavor label (r). They transform according to the fundamental $\underline{3}$ representation of $SU(3)_{color}$ as:

$$\Psi_\alpha^{ar}(x) \rightarrow \sum_b U^{ab}(\omega(x))\Psi_\alpha^{br}(x) \tag{2.1}$$

with

$$U^{ab}(\omega(x)) = \left[e^{i\frac{\lambda^i}{2}\omega^i(x)}\right]_{ab} \quad ,$$

where the λ^i are the usual Gell-Mann matrices [2-9], satisfying $[\lambda^i, \lambda^j] = 2if^{ijk}\lambda^k$, f^{ijk} being the structure constants of $SU(3)_{color}$. Similarly, the gluon fields $A_\mu^i(x)$ (μ being a four-vector index and i a color label) transfrom as:

$$A_\mu(x) \rightarrow UA_\mu(x)U^\dagger - \frac{i}{g}(\partial_\mu U)U^\dagger \tag{2.2}$$

where $A_\mu(x)$ is the hermitian matrix:

$$A_\mu(x) = \sum_{i=1}^{8} \frac{\lambda^i}{2} A_\mu^i(x) \quad .$$

Introducing the field strength tensor

$$F_{\mu\nu} = \partial_\mu A_\nu - \partial_\nu A_\mu - i.g[A_\mu, A_\nu] \tag{2.3}$$

and the covariant derivative

$$D_\mu = \partial_\mu - i.g(\frac{\lambda^i}{2})A_\mu$$

one gets the following lagrangian density for QCD:

$$\mathcal{L} = -\frac{1}{4}F_{\mu\nu}F^{\mu\nu} + \bar{\Psi}^r(i\gamma_\mu D_\mu - m_r)\Psi^r \tag{2.4}$$

g is the bare coupling constant of the theory and m_r is the mass of flavor r. This lagrangian is written in terms of the *unrenormalized* fields Ψ^r and A_μ and is not yet properly quantized, therefore it cannot be used as such to compute scattering matrix elements.

One way to overcome this difficulty [2-10], is to redefine the fields as: $\Psi^r \rightarrow Z_2^{\frac{1}{2}}\Psi^r$ and $A_\mu \rightarrow Z_3^{\frac{1}{2}}A_\mu$ (Z_2 and Z_3 being the renormalization constants) and introduce gauge and ghost terms (in order to remove unphysical states) as follows:

$$\mathcal{L} \rightarrow \mathcal{L} + \mathcal{L}_{gauge} + \mathcal{L}_{ghost}$$

with

$$\mathcal{L}_{gauge} = -\frac{1}{2\lambda}\left[\partial_\mu A_\mu^i\right]^2, \qquad (covariant\ gauge),$$

and

$$\mathcal{L}_{ghost} = 2tr\{\partial_\mu \bar{\eta} \mathcal{D}_\mu \eta\}$$

where

$$\mathcal{D}_\mu \eta = \partial_\mu \eta - i.g[A_\mu, \eta],$$

η is the ghost field. From this complete lagrangian, one can read off the Feynman rules necessary to do any QCD calculation. These are given in Fig. 2.1.

2.3 QCD and e^+e^- jets

One of the biggest advantages of e^+e^-collisions is the simplicity of the initial state which consists of pointlike particles. Electrons and positrons annihilate through a photon or Z° into $f\bar{f}$, the cross section at a center of mass energy $\sqrt{s}$ being given by the Electroweak theory [2-11]:

$$\sigma_{EW} = N_c \sum_f [Q_f^2 + 2Q_f \chi_W s g_V^e g_V^f + \chi_W^2 s^2 (g_V^{e2} + g_A^{e2})(g_V^{f2} + g_A^{f2})], \qquad (2.5)$$

$$where\ \chi_W = [sin^2\theta_W cos^2\theta_W (M_{Z^\circ}^2 - s)]^{-1},$$
$$g_V^i = T_{3L}^i - 2Q_i sin^2\theta_W \quad is\ the\ weak\ vector\ coupling,$$
$$g_A^i = T_{3L}^i \quad is\ the\ weak\ axial\ coupling,$$

T^i_{3L} is the third component of the weak isospin of the produced fermion, θ_W the weak mixing angle, M_{Z° the Z° mass, $N_c = 3$ the number of colors, and Q_f the electric charge of flavor *f*.

Two different procedures are used to formulate the perturbative approximation for the final state. In "fixed order QCD", every term in an expansion is retained up to a certain order (to date, up to the 2^{nd}), while neglecting higher oder terms. In "leading-log QCD (LLA)", one sums the largest contributions from all orders, while neglecting non-leading terms at each stage. In this study, we will consider only "fixed order QCD".

To 0^{th} order in QCD, the total cross section for $e^+e^- \rightarrow$ *hadrons* is given by the quark-parton model:

$$\sigma^\circ = 3.\sigma_{\mu\mu} \sum_f Q_f^2 \tag{2.6}$$

where $\sigma_{\mu\mu} = \frac{4}{3}\pi\alpha^2/s$ is the 1^{st} order cross section for the process $e^+e^- \rightarrow \mu^+\mu^-$, α being the fine structure constant. This cross section describes the process shown in Fig. 2.2a.

The 1^{st} order cross section can be expressed as:

$$\sigma^1 = |A|^2 + |B|^2 + |A \otimes C|$$

where $|A|^2$ refers to the contribution from Fig. 2.2a (0^{th} order), $|B|^2$ comes from the bremsstrahlung diagrams in Fig. 2.2b, whereas $|A \otimes C|$ refers to the interference of the virtual diagrams 2.2c with the 0^{th} order diagram 2.2a. Each of the diagrams 2.2c diverges as the momentum of the virtual gluon increases ("ultraviolet divergence"). However, these divergences cancel when the three terms are summed. The total cross section is found to be [2-12]:

$$\sigma^1 = \sigma^\circ \left[1 + \frac{\alpha_s}{\pi}\right] \tag{2.7}$$

One can also express the three parton cross section [2-13]:

$$\frac{1}{\sigma^\circ}\frac{d^2\sigma(e^+e^- \to q\bar{q}g)}{dx_q dx_{\bar{q}}} = \frac{\alpha_s}{2\pi}C_f\frac{x_q^2 + x_{\bar{q}}^2}{(1-x_q)(1-x_{\bar{q}})}, \qquad x_{q,\bar{q}} = \frac{2P_{q,\bar{q}}}{\sqrt{s}} \tag{2.8}$$

where $C_f = (N_c^2 - 1)/2N_c = 4/3$ is the Casimir operator. The two poles in the denominator reveal the presence of infrared ($x_q = 1$ *and* $x_{\bar{q}} = 1$) and colinear ($x_q = 1$ *or* $x_{\bar{q}} = 1$) singularities. These singularities reflect the physical impossibility of distinguishing an isolated quark from a quark which has emitted an arbitrarily soft gluon, or a gluon along its direction of motion.

In order to reject such singularities from the three parton phase space, ***resolution*** cuts are introduced. Two sets of cuts are commonly used, the scaled parton-parton invariant mass cut (Y cut):

$$Y_{ij} \equiv 2\min_{i\neq j}\frac{P_iP_j - \vec{P}_i.\vec{P}_j}{(\sum_k P_k)^2} \geq Y_{cut}, \tag{2.9}$$

and the Sterman-Weinberg cuts [2-14] ($\epsilon - \delta cut$):

$$\epsilon \equiv \min_i \frac{P_i}{(\sum_k P_k)} \geq \epsilon_{cut} \qquad and \qquad cos(2\delta) \equiv \max_{i\neq j}\frac{\vec{P}_i.\vec{P}_j}{P_iP_j} < cos(2\delta_{cut}), \tag{2.10}$$

where $\vec{P}_i$, P_i are respectively the momentum vector and magnitude of parton i. Usual cutoff values are 0.2 to 0.5 for Y_{cut}, corresponding to an invariant mass of 3.5 GeV to 5.5 GeV at $\sqrt{s} = 35$ GeV, $cos(2\delta_{cut}) = 0.9$ and ϵ ranging from 0.07 to 0.15. A three parton event containing a parton pair which fails the cut is substracted from the three parton sample and treated as a two parton event. This procedure explicitly removes the divergences from the three parton cross section.

Finally the 2^{nd} order corrections are given by summing the following contributions:

i) : 4-parton events $e^+e^- \to q\bar{q}q\bar{q}$ and $e^+e^- \to q\bar{q}gg$ given by the diagrams of Fig. 2.2d.

ii) : Interference of the diagrams of 2.2a with the two-loop corrections of Fig. 2.3b to $e^+e^- \rightarrow q\bar{q}$.

iii) : Interference of diagrams 2.2b with the one-loop corrections of Fig. 2.3a to $e^+e^- \rightarrow q\bar{q}g$.

However, the total cross section to 2^{nd} order has not yet been computed from the sum of the dressed* 2, 3 and 4 parton cross sections. Instead, it has been related to the imaginary part of the inverse photon propagator [2-15]. Furthermore, 2^{nd} order QCD calculations depend on the particular method to renormalize α_s. In the $\overline{MS}$ scheme ("modified minimal subtraction") [2-16], and assuming five quark flavors, the total hadronic cross section is given by:

$$\sigma^2 = \sigma^\circ \left[1 + (\frac{\alpha_s}{\pi}) + 1.405(\frac{\alpha_s}{\pi})^2\right], \tag{2.11}$$

with the coupling strength α_s is given by:

$$\alpha_s = \frac{2\pi}{b_\circ log(s/\Lambda^2) + (b_1/b_\circ).log(log(s/\Lambda^2))}, \tag{2.12}$$

where $b_\circ = \frac{23}{6}$ and $b_1 = \frac{29}{3}$. The parameter Λ has its origin in the summation of the infinite series of single loop corrections (*cf* [2-12]). It defines the scale of the coupling and has to be determined experimentally.

A cutoff procedure is again implemented for removing infrared divergences. The two cutoff procedures yield different expressions for the individual two and three parton cross sections. However they were shown to converge to identical limits in the case of vanishing cutoff values [2-17]. The three parton cross section has been calculated by several groups [2-18]. In this study, we use a calculation, based on Ref. 18a, which uses a Monte Carlo integration of the phase space [2-19].

---

* By dressed n parton event, we mean the total contribution to this class of events from genuine n parton events and (n+1) parton events which failed resolution cuts.

2.4 Fragmentation

As already pointed out, QCD does not provide a description of the fragmentation process through which partons dress themselves up into observed hadrons. To make any confrontation between experimental data and theory, various fragmentation models have been developed. In this study, we consider three of them. In this section, we describe them in order of increasing sophistication, starting with the Independent Jet (IJ) model, then the string and parton showers models.

2.4.1 Independent Jet Fragmentation (IJ)

Originally introduced by Field and Feynman [2-20a] for $e^+e^- \rightarrow q\bar{q}$, this model was extended to $e^+e^- \rightarrow q\bar{q}g$ by Hoyer *et al.*[2-20b] and Ali *et al.*[2-20c]. The principle is sketched in Fig. 2.4a. Each jet is an independent $q \rightarrow q' + meson$ cascade repeating until there is insufficient energy to continue. All needed quarks are pulled from the vacuum. This model implicitly fails to conserve energy and momentum. This is fixed by a suitable Lorentz boost of the jets of hadrons. Gluon jets are handled as $q\bar{q}$ pairs. This model uses three parameters:

a). σ_q, the width of the distribution of the transverse momenta k_T of the quarks in the jets, assumed to be gaussian $\sim exp(-k_T^2/2\sigma_q^2)$,

b). P/(P+V), P/V being the ratio of primordial pseudoscalar mesons to vector mesons,

c). The fragmentation function $f_q^h(z)$, of flavor q into a hadron,

$$f_q^h(z) = 1 - a_F + 3a_F(1-z)^2 \qquad for\ u,\ d,\ s\ quarks,$$

$$f_q^h(z) = \frac{C}{z\left(1 - \frac{1}{z} - \frac{\epsilon_q}{1-z}\right)^2} \qquad for\ b,\ c\ quarks,$$

where,

$$z = \frac{(E + P_{||})_{hadron}}{(E + P_{||})_{quark}}$$

E being the energy and $P_{||}$ the component of the momentum P along the direction of the primordial quark. The function $f^h(z)$ determines the likelihood of the hadron carrying off a fraction z of the parent quark's initial $E + P_{||}$.

2.4.2 The Color String Model (Lund)

In this model [2-21], a light $q\bar{q}$ pair is produced at $(t = 0, x = 0)$ and the particles travel out along the light-cone, losing energy to the color field between them (the stored energy is about 1 GeV/fm), see Fig. 2.4b. $q\bar{q}$ pairs are born in this color field at random points and eventually form bound states. The quark pair production points P_o, P_1, P_2, etc..., are required to lie on hyperbolae defined by $x^2 - t^2 = M_n^2/K^2$, where M_n give energy levels and K a constant. Lorentz invariance is a natural property of string fragmentation and the fragmentation function is fixed by demanding that the creation points be independent. Left-right symmetry imposes a fragmentation function given by:

$$f^h(z) = (1 - z)^a z^{-1} exp(-bM_\perp^2/z),$$

where $M_\perp^2 \equiv M^2 + P_\perp^2$ is the "transverse mass" of the produced hadron and the two parameters a and b are constants determined from data. This model produces jets which are shifted from the original parton directions, particularly distorting three jet events, where one observes more particles on the side of the event opposite the $q\bar{q}$ region, see Fig. 2.5a. In this thesis, we use the Lund fragmentation Monte Carlo, version 6.3 [2-21b], with $a = 1.0$ and $b = 0.7$.

2.4.3 Cluster models

These models have been introduced more recently [2-22]. In this approach, quark pairs are generated and initiate parton showers by radiating gluons. These gluons can split again into gluon pairs, and less frequently into quark pairs. The process is terminated when the virtual mass of the initial parton reaches a cut-off value and colorless clusters are formed. In the Gottschalk model that we use, the cutt-off value is set at $1.0GeV^2$. Figures 2.5b,c give a description of these processes. Cluster models have fewer parameters than the previous two and are usually used together with LLA parton generation. However, in this study we

also use our fixed order QCD calculation. We will not attempt fits to α_s with these models, but rather investigate on their ability to describe various measured distributions. This will be done in Appendix B.

The IJ and Lund models are the two extreme cases. In the former, the interaction between partons is assumed to be negligible until the end of the fragmentation process. In the latter, maximal interaction between partons through strings is assumed. For pure $q\bar{q}$ events, the two models do agree however. Cluster models lie somewhere in between these two approaches, depending on the momentum region being considered.

Chapter 3

The Experiment

3.1 Petra

The e^+e^-storage ring PETRA [3-1] (Positron Elektron Tandem Ringbeschleuniger Anlage) with its four experiments and its injection apparatus is shown in Fig 3.1a and 3.1b. The ring, with a circumference of 2.3 kilometers, has eight long straight sections, two of which are reserved for the RF accelerating cavities. Electrons are injected from Linac I into DESY (Deutsches Elektronen Synchrotron), accelerated to 7 GeV, and injected into the PETRA ring to form two bunches of 3–5 mA each. Each bunch has a length of, approximately, 1.3 cm in r.m.s, and tranverse dimensions σ_x and σ_y of respectively $500\mu m$ and $100\mu m$. Positrons, produced by scattering electrons off lead targets, are accelerated in Linac II, accumulated in PIA (Positron Intensity Accumulator), and further accelerated in DESY before being injected into PETRA. The two pairs of counter–circulating bunches are further accelerated and focused to collide inside the four experiments. PETRA has been providing luminosity runs at various center of mass energies, ranging from 13 GeV at its beginning in November

1978, up to 46.78 GeV in spring of 1984. Mini–β quadrupoles were installed in 1981 about 4 meters from the interaction regions in order to increase the luminosity by a strong focusing of the electron and positron beams. The maximum instantaneous luminosity collected with the MARK–J detector was $1.6 \cdot 10^{31}/\mathrm{cm}^2/\mathrm{sec}$. In this thesis, we use all the data taken, through an eight year period, with the MarkJ detector. The bulk of this data is at a center of mass energy $\sqrt{s} \sim 35$ GeV.

3.2 The Mark-J detector

The MARK–J detector, Fig 3.2a and 3.2b, consists mainly of three parts: a high resolution inner vertex detector, electromagnetic and hadron calorimeters, and a muon spectrometer. For its last year of data taking, Mark–J has been modified, compared to its earlier configuration [3-2], by the introduction of a new high resolution vertex detector: the TEC (Time Expansion Chamber), Fig. 3.3. Particles leaving the e^+e^-interaction region traverse the detector layers shown schematically in Fig 3.4. Outside of the beampipe is the vertex detector, the TEC, followed by arrays of drift tubes (labelled DT in Fig 3.3) to measure the z coordinate along the beam axis. The next layers are the lead scintillation counters (A,B,C) for electromagnetic shower detection, surrounded by the inner drift chambers of the muon spectrometer (S,T,U,V). Proceeding radially outwards, four layers of scintillation counters (K), dedicated to hadronic energy deposit measurements, are imbedded in the magnetized iron of the toroidal magnet. The outermost part of the detector completes the muon spectometer with trigger counters (D,E), and more drift chambers half way through (Q) and outside (P,R) of the magnet.

The vertex detector, TEC, Fig 3.5a, is a drift chamber based on a time expansion principle [3-3], and has the following features:

(a) : A low field drift region (drift velocity of $\sim$ *7 microns/nsec*), separated from a small, high field, detection region, Fig. 3.5b.

(b) : A "cool" gas (CO_2 with i–C_4H_{10} as quencher) to get the lowest possible diffusion.

(c) : 100 MHz Flash–ADC system to sample the pulses and allow for drift time determination by a center of gravity method.

More details on this chamber can be found in Ref. [3-4]. TEC is glued onto a 10 cm diameter beam pipe whose thickness amounts in total to 3% radiation length. The chamber itself consists of 12 segments having 12 sense wires each. In order to solve the left–right ambiguity, the sense wire planes were tilted with respect to the radial direction by an angle of 4°. The average resolution achieved on single tracks was ~ 40 μ, whereas the two–track separation ability was tested to be ~ 400 μ. For this analysis, we do not use the information provided by the TEC due to problems encountered with its calibration. Instead, we used the set of 2600 drift tubes. These surround TEC and were used for the z coordinate measurement, Fig. 3.6a. They cover the polar angle from $\theta = 10°$ to 170° and the entire azimuth less 7° in each corner. The resolution per tube is 0.03 cm. Figure 3.6b shows the reconstructed z vertex position using the DT for Bhabha events. The 1.3 cm resolution is in agreement with the beam characteristics of Petra.

Both endcap regions are covered by 24 scintillation counters H and 48 G lead glass counters covering the small angle region $5° \leq \theta \leq 10°$, as shown in Fig. 3.7. The information from these counters was used only for the data taken in 1986 in order to study the effect of a closer to 4π detector acceptance.

The inner calorimeter provides most of the information about hadronic events. It is subdivided into three azimuthally segmented layers of shower counters (A,B,C in Fig 3.3). Each counter is made up of 0.5 cm thick pieces of scintillator alternated with 0.5 cm thick lead plates. At normal incidence this yields 3, 3 and 12 radiation lengths or a total of 1 absorbtion length. The 20 A counters are arrayed parallel to the beamline outside of an iron box which surrounds the vertex detector. They cover the polar angle $\theta = 12°$ to 168° with no azimuthal holes. The 24 B and 16 C counters are arranged similarly to the A counters, but are offset in ϕ and shorter, covering $\theta = 16°$ to 164°. Each of these sixty counters is instrumented with a phototube at each end. The time and magnitude of both phototube pulses are digitized with TDCs and ADCs and recorded. The longitudinal hit position is measured by a weighted average of the positions determined from the time difference between the two pulses and from their relative magnitude. The energy deposited in each counter is determined from the two pulse heights corrected for attenuation. The leakage of electromagnetic showers from electrons and gamma rays into the outer calorimeter is less than 4%. In figures 3.8 we show the energy distributions for each counter type separately.

On average, a hadronic event deposits 75% of its energy in this inner calorimeter.

The outer calorimeter (K), absorbs the remaining 25% of the energy from a hadronic event. The 192 scintillation counters are arranged in four layers interleaved with 2.5 to 10 cm of iron for a total of 2 absorbtion lengths at normal incidence. The two inner (outer) layers cover the polar range $\theta = 43°$ to 137° (26° to 154°) with azimuthal holes of 10° (4°). In this calorimeter the ϕ resolution is $\sim 2°$ better than in the inner calorimeter because of the finer segmentation. The longitudinal resolution is worse because only one end of each counter is viewed by a phototube. Energy distributions for each of the K counters are shown in figures 3.9. The active solid angle for this outer calorimeter is 95% of 4π. The hadronic energy resolution is about 17% at $\sqrt{s}$=35 GeV.

The inner part of the muon spectrometer consists of twelve planes of drift chambers (S,T) enveloping the inner calorimeter (A,B,C), and ten similar planes (U,V) covering the endcap regions. Following are the magnetized iron plates, two plane drift chambers (Q), the scintillation counters (K) and the TOF trigger counters (D). The magnet provides a minimum bending power of 1.7 Tesla–m. Muons are identified by their ability to penetrate the 5.4 hadronic interaction lengths of material in the toroidal magnet. The ten (P) and twelve (R) outer, large area drift chambers complete the spectrometer and are mainly used to measure the muon tracks angles. All drift chambers are of similar construction and permit to solve left–right ambiguity by a system of displaced layers of cells. Individual cells have a resolution of 0.4 mm for perpendicular tracks. More details on these chambers as well as the rest of the Mark–J detector can be found in Ref. [3-2].

Chapter 4

Data Manipulation

4.1 Introduction

Every 3.8 μs electrons and positrons collide in the central region of the MarkJ detector. However, only a small fraction of these events can be used for physics analysis. Indeed, with a luminosity of $10^{31} cm^{-2} s^{-1}$, one expects approximately 13 hadronic events per hour at $\sqrt{s}$ ~35 GeV: the majority of the signals from the detector components are background signals originating in beam-gas and cosmic ray events. Furthermore, such a high event rate (260,000 events/sec) cannot be handled by the data acquisition system. It is therefore imperative to perform a data reduction. This is achieved by a two-stage procedure, the first being *online* and the second *offline*.

4.2 Online data reduction

The online data reduction is arranged in three stages: a fast electronic trigger, a total energy trigger, and a final selection assigned to a Microprogrammable Branch Driver (MBD). The goal of this system is to reduce the data taking rate from 260 kHz to 1 Hz at the time of dumping out the event on magnetic tape. Evidently, this data reduction is set up to take into account all kinds of possibly interesting events, not just those of hadronic nature. We describe here, however, only parts relevant to the hadronic event selection. More details on the whole system can be found in [4-1].

The hadron trigger relies mainly on information provided by the electromagnetic calorimeter (A, B and C counters in Fig. 3.2), namely on:

(a) : The number of A, B and C counter elements hit.

(b) : Total energy loss in A, B, C.

(c) : Energy balance between opposite quadrants of A, B, C counter arrays.

Practically, the first condition of this trigger requires that the event causes at least three A *and* three B counters to give signals. The last two conditions are satisfied by any *two* of the following requirements:

- $A_u \geq 50MeV$ and $A_d \geq 50MeV$
- $A_l \geq 50MeV$ and $A_r \geq 50MeV$
- $B_u \geq 50MeV$ and $B_d \geq 50MeV$
- $B_l \geq 50MeV$ and $B_r \geq 50MeV$
- $C_u \geq 50MeV$ and $C_d \geq 50MeV$
- $C_l \geq 50MeV$ and $C_r \geq 50MeV$

where A_u, A_d, A_l and A_r refer to the energy deposited in an A counter located respec-

tively in the upper, lower, left, and right quadrant of the detector. Similar definitions apply to B and C counters.

This first stage trigger is not sufficient for reducing the event rate which can still be high (during unfavorable beam conditions, it can reach 400 Hz). It is brought down further by the two last stages of the online data reduction system: the total energy trigger and the MBD filtering. At this level, a fast and conservative estimate of the total energy deposited in the counters is performed. The event is accepted if this total energy exceeds $\sqrt{s}/6$.

Approximately 15 hadronic event candidates, per minute, are finally written to magnetic tape via a PDP-11 online computer. Monte Carlo studies have shown that this online data reduction is practically 100% efficient.

4.3 Offline event selection

In a rather similar fashion, the offline data selection is reached in three steps. The goal of this selection being to reject any background signals while keeping the acceptance for hadronic events as high as possible. The major sources of background for hadronic events are the following:

- ♠ : Two photon events, mainly $e^+e^- \rightarrow e^+e^-f^+f^-$ and $e^+e^- \rightarrow e^+e^-q\bar{q}$ where the *f's* stand for fermions.
- ♠ : Tau events $e^+e^- \rightarrow \tau^+\tau^- \rightarrow hadrons$
- ♠ : Bhabha events $e^+e^- \rightarrow e^+e^-$
- ♠ : Beam-gas interactions.

The selection relies primarily on energy considerations. For convenience, we introduce here some notations concerning energy vectors. Each counter hit (i.e A, B, C and K's in Fig. 3.2) is assigned a unit vector $\vec{e}_i$ pointing to its position. The center of the reference frame being the center of the MarkJ detector. The energy vector associated with a counter hit i is therefore the vector: $E_i.\vec{e}_i$ where E_i is the energy measured by counter i. The total

measured, or *visible*, energy in an event is:

$$E_{vis} = \sum_i E_i$$

, whereas the total energy vector is:

$$\vec{E} = \sum_i E_i.\vec{e}_i.$$

For an ideal detector, one would expect $\vec{E} = \vec{0}$. In real life situations, it is used to study the energy imbalance of the event, namely by considering the longitudinal energy $E_l = |E_z|$ and the transverse energy $E_\perp = \sqrt{E_x^2 + E_y^2}$, E_x, E_y and E_z being the components of $\vec{E}$. For the final hadronic sample these quantities are shown in Figures 4.1 and 4.2.

The selection proceeds as follows:

1. $0.25\sqrt{s} \leq E_{vis} \leq 2.0\sqrt{s}$. The lower bound mainly rejects events with muons, and part of the two photon and beam-gas events. The upper bound rejects cosmic showers which can deposit large amounts of energy in the detector. At least 60% of the data sample is rejected at this first step.

2. $E_{vis} \geq 0.35\sqrt{s}$, $E_l \leq 0.70\sqrt{s}$ and $E_\perp \leq 0.70\sqrt{s}$. We shall refer to this cut as 35/70/70 cut. Furthermore, the energy deposited in the outer calorimeter (K counters, Fig. 3.2) is required to be in the range $0.05\sqrt{s}$ to $0.70\sqrt{s}$. Finally, a multiplicity cut imposing the number of tracks, within 10 cm of the interaction point, in the vertex detector (DT in Fig. 3.2), to be larger than three. This step rejects most of the τ pair events as well as part of the bhabha events. After this step, the sample is splitted in two parts: identified hadrons and ambiguous events. Typically, more than 80% of the hadronic events are identified at this stage.

3. This last stage involves visual scanning of the ambiguous events from step 2 above. Selection on this stage is based on energy distribution and balance, timing information from the counters, as well as the number of tracks fitted in the vertex detector. Figures 4.3, 4.4 and 4.5 show displays from various detector components of a selected hadronic event.

The sample gotten at the end of these steps is still not the final one that would be used for physics results. This is due to the rather approximate nature of the cuts applied. Indeed, before finalizing the sample, a detector calibration, which we describe later, is performed. The sample used in the analysis is required to satisfy:

$$E_{vis} \geq 0.7\sqrt{s}, \qquad E_l \leq 0.5\sqrt{s}, \qquad E_\perp \leq 0.5\sqrt{s}$$

. We shall refer to this cut as 70/50/50. In Fig. 4.6 we show the number of hadronic events, after all cuts, as a function of $\sqrt{s}$, from the eight year running period of MarkJ. The 31,500 events at $\sqrt{s} \sim 35GeV$ constitute the bulk of the total sample.

4.4 Detector calibration

There are two quantities that one seeks from the detector components: energy deposited and position of the hit. Hence, it is of primary importance to know continuously, in as much detail as possible, the response and the behavior of each of these components. Before describing the methods used for calibrating relevant parts of the MarkJ detector, we show first how position and energy are calculated. Each of the inner calorimeter counters (A, B, C) is viewed by two phototubes, whereas the outer calorimeter counters (K's) have only one phototube. Each phototube is connected to a TDC and ADC, as shown in Fig. 4.7a.

1. *Position Determination* : The x and y coordinates are taken as those of the center of the counter hit. The z position (along the beam) is calculated from both ADC information:

$$Z_A = \frac{\lambda}{2}.ln(\frac{ADC_2.Gain_2}{ADC_1.Gain_1})$$

and TDC information:

$$Z_T = \frac{v_c}{2}.((T_2 - T_{02}) - (T_1 - T_{01})) \quad ,$$

with λ being the light attenuation length in the counter, v_c the velocity of light in the counter, ADC_i and TDC_i the ADC and TDC readings (after pedestal substraction), and $Gain_i$ and T_{0i} the gain and zero timing for each phototube. The zero timing T_0 is identified with the electronics time, and can be expressed as:

$$T_0 = T - t_c - t_f = T - \frac{d}{v_c} - t_f$$

where t_c is the travel time of light in the scintillator, and t_f is the time of flight from the interaction point to the counter hit position (Fig. 4.7b).

The two formulae above are valid only for the two-phototube counters. For the single phototube counters (K), the z position is obtained either from the TDC information or from extrapolation of the A, B, and C counter tracks. The final z position assigned to a hit is a weighted sum of Z_A and Z_T, the weights being determined by an algorithm taking into account the counter type, the ADC and TDC readings.

2. *Energy Determination* : It is given by the following formula:

$$E = G_f(ADC_1.Gain_1.e^{(\frac{l}{2}+z)/\lambda} + ADC_2.Gain_2.e^{(\frac{l}{2}-z)/\lambda})$$

where l is the counter length and G_f is a factor depending on the geometry of the counter and the type of interaction (electromagnetic or hadronic).

The dependence of energy and position measurements on the above constants imposes a continuous monitoring of their values which are expected to vary with time due to the following reasons:

- Changes in the photomultiplier gains.
- Changes in the light propagation velocity and attenuation length.
- Changes in the electronics.

Two types of events are central to the detector calibration: cosmic rays and bhabha events. They are used to adjust the gain constants and the time zero constants T_0. Pedestal values are obtained by randomly opening the ADC gates (i.e with zero input charge to the ADC's). Cosmic rays provide a good source of energetic muons (minimum ionizing particles) which deposit a constant energy E_μ in the counters. A large number of such events is carefully selected and used to determine the gain constants from the relation:

$$Gain = \frac{E_\mu}{\overline{ADC} - Pedestal},$$

where $\overline{ADC}$ is the average ADC value for a given counter and *Pedestal* the corresponding pedestal.

On the other hand, bhabha events leave clean tracks in the drift tube arrays (DT). By comparing Z_{tu}, the expected counter hit position extrapolated from the DT track, to the position determined by the counter itself (Z_{TDC} or Z_{ADC}), one can determine T_0 and make a fine adjustment of the gains. In Fig. 4.8a and 4.8b we show the distributions for $Z_{tu} - Z_{TDC}$ and $Z_{tu} - Z_{ADC}$ for the inner A counters. These show that the resolution for Z_{TDC} and Z_{ADC} are respectively 19 mm and 46 mm. Another plot that would show systematic shifts in z position measurements is $Z_{tu} - Z_{ADC}$ or $Z_{tu} - Z_{TDC}$ versus Z_{tu}, see Fig. 4.9a and 4.9b.

Chapter 5

Measurement of the Strong Coupling Constant

In this chapter, we present measurements of the strong coupling constant α_s at various center of mass energies. We first describe the implementation of the models, in particular the MarkJ 2^{nd} order QCD calculation. Then, we define the variables used for the measurements, the Asymmetry (ASY) of energy-energy correlations (EEC) and Planar Triple Energy Correlations (PTC). Finally, by fitting the theoretical models to our data, we deduce α_s.

5.1 Implementation of the models

The complete Monte Carlo simulation of the process $e^+e^- \rightarrow$ *hadrons* proceeds in four main steps:

- Generation of two primary quarks through both virtual photons and Z^0. Radiative corrections are handled up to order $O(\alpha^3)$, using the code of Berends *et al.*, [5-1].
- Production of additional quarks and gluons from the primary quarks to 2^{nd} order in QCD. We describe this procedure below.
- Generation of primary hadrons and subsequent decay of the unstable ones among them. We already described this process in Chapter 2, (fragmentation).
- Simulation of the detector response to the events generated.

5.1.1 MarkJ 2^{nd} order QCD calculation

The MarkJ QCD calculation [2-19], uses the matrix elements of Eilis-Ross-Terrano, [2-18], with a prescription due to Kunszt [5-2], aimed at improving the convergence of the numerical computations. The cross sections for 2,3 and 4 jet * events, with jet resolution cuts imposed are:

$$\sigma_{3-jet} = \sigma_{3-Born} + \sigma_{3-vir} + \sigma_{4-soft} - \sigma_{3-soft}, \tag{5.1}$$

$$\sigma_{4-jet} = \sigma_{4-Born} - \sigma_{4-soft}, \tag{5.2}$$

$$\sigma_{2-jet} = \sigma^2 - \sigma_{3-jet} - \sigma_{4-jet} \tag{5.3}$$

where σ_{3-Born} and σ_{4-Born} are the the contributions of diagrams 2.2b and 2.2d respectively, σ_{3-vir} is the virtual correction to $e^+e^- \rightarrow q\bar{q}g$, namely the interference of diagrams 2.2b with 2.3a. σ_{3-soft} and σ_{4-soft} refer to contributions, which fail the resolution cuts, from, respectively, 3-jet and 4-jet events. σ^2 is the order $O(\alpha_s^2)$ total cross section given by equation (2.11). The $O(\alpha_s^2)$ corrections to 3-jet events is factorized as a two-dimensional function $R(x_g, x_q - x_{\bar{q}})$ in the Dalitz distribution:

---

* In this context, the word "jet" refers to the number of QCD partons.

$$\frac{1}{\sigma^\circ}\frac{d\sigma(e^+e^- \to q\bar{q}g)}{dx_g d(x_q - x_{\bar{q}})} = A_\circ \frac{\alpha_s}{\pi}\left\{1 + R(x_g, x_q - x_{\bar{q}})\frac{\alpha_s}{\pi}\right\}, \tag{5.4}$$

where $x_i = 2P_i/\sqrt{s}$ are the normalized momenta, and σ° the 0^{th} order total cross section, equation (2.6). The function R and the constant $A_\circ$ do not depend on α_s. However, R does depend on the resolution cut. It is fitted to a polynomial function of x_g and $x_q - x_{\bar{q}}$ which gives the $O(\alpha_s^2)$ correction to the 3-jet cross section. In table 5.1 below, we give the fractional partial cross sections for various values of the invariant mass cut-off Y_{cut}.

Y_{cut}	2 jets	3 jets $O(\alpha_s)$	3 jets $O(\alpha_s^2)$	4 jets
0.02	0.432	0.423	0.105	0.040
0.03	0.567	0.319	0.096	0.018
0.04	0.659	0.253	0.078	0.009
0.05	0.725	0.204	0.065	0.005

Table 5.1 Jet fractions at $\sqrt{s} = 35\ GeV$ with $\alpha_s = 0.12$.

5.1.2 Detector Simulation

After fragmentation of the generated parton events, the response of the detector to the produced hadrons is simulated. Particles are represented by energy vectors whose intersection points with the active parts of the detector are computed. Tabulated information, obtained from test beams, give, for each counter element, the energy deposited, penetration depth and angular position for each particle. To make comparison easier with data, all the hits are digitized in the form of ADC and TDC measurements. Care is taken to take into account the counters characteristics in this digitization, namely attenuation length, speed of light in the scintillator, time slewing due to varying pulse heights and multiple hits. Time of flight corrections are also included. The output of this detector simulation is compared directly to the data. We use this detector simulation to study the detector acceptance for hadronic events, as well as the background. The acceptance is computed by

a direct comparison of the number of generated events to the number of events "detected" by the simulation process. It is found to be 75% for the 70/50/50 cut (see Sec. 4.3). For the same cut, the background contribution from Bhabha, tau-pair and two-photon events is less than 4%.

The Monte Carlo prediction for any variable X is determined in the following manner. It is computed separately for each event type n (2-jet, 3-jet $O(\alpha_s)$, 3-jet $O(\alpha_s^2)$, or 4 jets) and then normalized to the corresponding number of events N_n:

$$X_n = \frac{1}{N_n} \sum_{i=1}^{N_n} X_{i,n}, \tag{5.5}$$

From this one can write the prediction for X, for a given α_s, as follows:

$$X^{MC}(\alpha_s) = \frac{\sum_{n=1}^{4} X_n A_n \sigma_n(\alpha_s)}{\sum_{n=1}^{4} A_n \sigma_n(\alpha_s)}, \tag{5.6}$$

where A_n and $\sigma_n(\alpha_s)$ are respectively the detector acceptance and fractional partial cross sections for event of type n. $X^{MC}(\alpha_s)$ as written above is compared directly to the data. α_s is then varied in order to perform the fit.

5.2 Choice of variables

As seen in Chapter 2, QCD describes the quark-gluon and gluon-gluon interaction, the scale of the coupling being given by α_s. Theferore, a first requirement on any variable used to determine α_s is the sensitivity to gluon emission. Such a phenomenon appears, in real life, as a deformation of the usual 2-jet event topology due to the underlying $e^+e^- \rightarrow q\bar{q}g$ process. Indeed, if one of the quarks emits a gluon, then one expects - for not a too energetic gluon - the corresponding jet to be broader than the one opposite it. If the quark, anti-quark and the gluon share equally the total energy, then the event topology becomes isotropic with three distinct jets arranged as a star *a la* "Mercedes-Benz". Genuine three jets lie on a plane, due to momentum conservation. A large number of variables aimed at measuring α_s have been proposed; only a few of them proved to be reliable. In addition to

the actual "experimental measurability" of any variable, it is required to fulfill the following criteria:

a) Small high order corrections from the QCD perturbative expansion.

b) Reasonably insensitive to the jet resolution criteria.

c) Small dependence on fragmentation effects.

The last criterion favors variables which are linear in the particle momenta. This is particularly important for the MarkJ detector where only energies deposited in counter elements (and not *momenta*) are measured. Furthermore, since fragmentation effects are supposed to decrease following an inverse power of s law, whereas QCD contributions vary as $\sim$ *logs*, then a relatively flat dependence on s for the variable would certainly be an advantage. Finally, one should bear in mind, that cuts are usually applied on the variable. Such cuts are adjusted, using Monte Carlo studies, so that a good selection of relevant events is achieved. Any dependence of a physics result, such as α_s, on these cuts is added to the systematic errors.

Amongst the first variables used are Thrust, and Oblateness [5-3]. The thrust value T is defined as:

$$T = \max_{\hat{t}} \frac{\sum_i |\vec{E}_i.\hat{t}|}{\sum_i E_i}, \tag{5.7}$$

where the $\hat{t}$ which maximizes the above expression is known as the thrust axis. On the other hand, the oblateness is given by:

$$Oblateness = O_b = Major - Minor, \tag{5.8}$$

where the Major and Minor are given by:

$$Major = \max_{\hat{m}} \frac{\sum_i |\vec{E}_i.\hat{m}|}{\sum_i E_i}, \qquad and \tag{5.9}$$

$$Minor = \frac{\sum_i |\vec{E}_i.\hat{n}|}{\sum_i E_i}, \qquad \hat{n} \perp \hat{t}, \text{ and } \hat{n} \perp \hat{m}, \tag{5.10}$$

where (5.9) is maximized while varying $\hat{m}$ and keeping $\hat{m} \perp \hat{t}$. The minor axis $\hat{n}$ approximates the axis of minimal energy flow. Since $q\bar{q}g$ events are expected to have a significantly larger Major than Minor, then a large oblateness will be a measure of "three jettiness". In the MarkJ analysis [5-4], α_s was first determined from fits to thrust distributions and to the fraction of events with $O_b > 0.3$. Both thrust and oblateness were shown to be non-reliable for α_s measurements. Thrust is dominated by $q\bar{q}$ events for which fragmentation effects are large. This is not the case for O_b, which was then preferred to thrust. In addition, thrust depends on the resolution cuts, as shown in Fig. 5.1a and 5.2a. The oblateness distribution of Fig. 5.1b is more stable, however its integrated contribution shows substantial variation for vanishing invariant mass cut, Fig. 5.2b. Furthermore, as shown in Ref. [2-18b], second order corrections to thrust and oblateness are important.

In this study, we use another class of variables, commonly referred to as the energy weighted cross sections, in order to determine α_s. We define them in this section and study their suitability for α_s measurements.

5.2.1 Energy-Energy Correlations

The Energy-Energy correlation function Σ^c, introduced by Basham *et al.*[5-5], is calculated as the energy weighted sum over pairs of particles i and j at an angle χ_{ij} between them:

$$\frac{1}{\sigma_{tot}} \frac{d\Sigma^c(\cos\chi)}{d\cos\chi} = \frac{1}{N_{ev}} \sum_{k=1}^{N_{ev}} \sum_{i,j} \frac{E_i^k E_j^k}{E_{vis}^2} \frac{1}{\Delta\cos\chi} \int_{\cos\chi-\Delta\cos\chi/2}^{\cos\chi+\Delta\cos\chi/2} \delta(\cos\chi_{ij} - \cos\chi') d\cos\chi', \tag{5.11}$$

N_{ev} is the total number of events. The inner sum extends over all pairs of particles in an event. Experimentally, it consists of plotting the pairwise products of fractional energy depositions versus the cosine of the angle between them. An immediate advantage of the

EEC is that it requires no detailed knowledge of individual events, such as determination of event axes. While pure two-jet events are expected to have entries only at the boundaries $\cos\chi = \pm 1$, three-jet events do have contributions in the region $-1 < \cos\chi < 1$. Four-jet events, due to their relative isotropy contribute symmetrically around $\cos\chi = 0$. An interesting feature of three-jet events, however, is that they contribute more at negative $\cos\chi$ than positive $\cos\chi$. This naturally suggests the introdution of a new variable, the Asymmetry (ASY) of the EEC:

$$A(\cos\chi) = \frac{1}{\sigma_{tot}}\left[\frac{d\Sigma^c(cos(\pi-\chi))}{dcos(\pi-\chi)} - \frac{d\Sigma^c(\cos\chi)}{d\cos\chi}\right], \qquad -1 \leq \cos\chi \leq 0. \tag{5.12}$$

In addition to being particularly sensitive to three-jet events, $A(\cos\chi)$ was shown to reduce fragmentation effects [5-6]. Figures 5.3 and 5.4 show the dependence of the EEC and ASY distributions on, respectively, $(\epsilon_{\rm cut}, \delta_{\rm cut})$ and $Y_{\rm cut}$. Although, the EEC does show some dependence on the cuts, it is clear that the ASY is practically stable against the cuts. In Fig. 5.5, we show the dependence of the integrated ASY:

$$ASY \equiv \int_{-0.72}^{0} A(\cos\chi) d\cos\chi, \tag{5.13}$$

on $Y_{\rm cut}$. The lower limit of integration is set to -0.72 instead of -1.0 in order to select the three-jet region. The integrated ASY is again seen to be stable and therefore we conclude that the ASY is an "infrared safe" variable. Both the EEC and ASY have been calculated to order $O(\alpha_s^2)$ [5-7]. The 2^{nd} order corrections have been found to be $\approx 30\%$ for the EEC and $\approx 10\%$ for the ASY. It is clear that the ASY fulfills the previously mentioned criteria. This makes it well adapted to measurements of α_s.

5.2.2 Triple Energy Correlations

For consistency checks, it would be helpful to have at hand another variable that could be used to measure α_s. The Triple Energy Correlation function just does that. It has been introduced by F. Csikor *et al.*[5-8] and is defined in the same spirit as the EEC, as follows:

$$\frac{1}{\sigma_{tot}}\frac{d\Sigma^{\rm TC}}{d\chi_1 d\chi_2 d\chi_3} = \frac{1}{\Delta\chi_1\Delta\chi_2\Delta\chi_3}\frac{1}{N_{ev}}\sum_{n=1}^{N_{ev}}\sum_{i,j,k}\frac{E_i^n E_j^n E_k^n}{E_{vis}^3}, \tag{5.14}$$

where the outer sum runs over all the events, and the inner sum runs over all triplets of particles. The angles χ_i are the relative angles between the three energy verctors. Of particular interest are planar events, in which case one has only two independent angles, the third one being fixed by the constraint $\sum_i \chi_i = 2\pi$. Experimentally, we select planar triplets by requiring $|2\pi - \chi_1 - \chi_2 - \chi_3| < \theta_p$, where θ_p is chosen to be 0.1 rad. One can therefore define the Planar Triple Energy Correlation function (PTC):

$$\frac{1}{\sigma_{tot}}\frac{d\Sigma^{\rm PTC}}{d\chi_1 d\chi_2} = \frac{1}{\Delta\chi_1\Delta\chi_2}\frac{1}{N_{ev}}\sum_{n=1}^{N_{ev}}\sum_{i,j,k}^{planar}\frac{E_i^n E_j^n E_k^n}{E_{vis}^3}, \tag{5.15}$$

Three jet events dominate the central region defined by $\chi_i < 180° - \beta$ *and* $\chi_1 + \chi_2 > 180° + \beta$. Monte Carlo studies show that for $\beta \approx 40°$, the contribution of three-jet events is more than 80%. The boundary regions, namely for $\chi_1 \to 180°$, $\chi_2 \to 180°$, and $\chi_3 \to 0°$ receive contributions mainly from $q\bar{q}$ events and $q\bar{q}g$ events where the emitted gluon is soft or collinear to one of the quarks. In figure 5.6, we show a "lego" plot of the PTC distribution for the 35 *GeV* data. The stability of the PTC against the resolution cuts is demonstrated in Figures 5.7 and 5.8, for respectively the Sterman-Weinberg $(\epsilon_{\rm cut}, \delta_{\rm cut})$ and invariant-mass $Y_{\rm cut}$ cuts. We also define the integrated PTC:

$$I(\beta) = \frac{1}{\sigma_{tot}}\int\int\frac{d\Sigma^{\rm PTC}}{d\chi_1 d\chi_2}d\chi_1 d\chi_2, \qquad with\ \chi_i < 180° - \beta,\ \chi_1 + \chi_2 > 180° + \beta, \tag{5.16}$$

which again shows stability against resolution cuts, Fig. 5.9. Order $O(\alpha_s^2)$ corrections to the PTC have been determined to be $\sim$ 20%. It is clear that the PTC is well adapted to α_s measurements. It is also a natural measure of three jet events since all three jets are treated equally, whereas in the ASY, one always integrates over one jet. This is illustrated by the following normalization:

$$\int \frac{d\Sigma^{\rm PTC}}{d\chi_1 d\chi_2} d\chi_2 + \int \frac{d\Sigma^{non-planar}}{d\chi_1 d\chi_2} d\chi_2 = \frac{d\Sigma^{\rm c}}{d\chi_1}, \tag{5.17}$$

where $\Sigma^{\rm c}$ is the EEC function, and $\Sigma^{non-planar}$ is the contribution from non-planar triplets.

5.3 Determination of α_s from the ASY function

In Fig. 5.10 and 5.11 we show the measured distribution for the EEC and ASY compared to Monte Carlo predictions, for, respectively $\sqrt{s} = 35\ GeV$ and $\sqrt{s} = 44\ GeV$. We fit Monte Carlo distributions by minimizing the following χ^2:

$$\chi^2(\alpha_s) = \sum_{k,l} \left\{ A_k^{Data} - A_k^{MC}(\alpha_s) \right\} \mathbf{V}_{\mathbf{kl}}^{-1} \left\{ A_l^{Data} - A_l^{MC}(\alpha_s) \right\}, \tag{5.18}$$

where A_k^{Data} and $A_k^{MC}(\alpha_s)$ are, respectively, the measured ASY and MC predicted ASY –as given by Equation. (5.6)– for the k^{th} bin in $\cos\chi$. $\mathbf{V_{kl}}$ is the covariance matrix, introduced to take into account bin to bin correlations. It is defined as:

$$\mathbf{V_{kl}} = \left[\sigma_{kl}^2(\Sigma^{\rm c}) + \sigma_{\bar{k}\bar{l}}^2(\Sigma^{\rm c}) \right]^{Data} + \left[\sigma_{kl}^2(\Sigma^{\rm c}) + \sigma_{\bar{k}\bar{l}}^2(\Sigma^{\rm c}) \right]^{MC}, \tag{5.19}$$

where

$$\cos\chi_{\bar{k}} = cos(\pi - \chi_k), \qquad and,$$

$$\sigma_{kl}^2(\Sigma^{\rm c}) = \frac{1}{N_{ev}} \left[\frac{1}{N_{ev}} \sum_{n=1}^{N_{ev}} (\Sigma_k^{(n)} \Sigma_l^{(n)}) - \frac{1}{N_{ev}} (\sum_{n=1}^{N_{ev}} \Sigma_k^{(n)}) \frac{1}{N_{ev}} (\sum_{n=1}^{N_{ev}} \Sigma_l^{(n)}) \right],$$

$$with \qquad \Sigma_k^{(n)} = \frac{1}{\Delta\cos\chi} \sum_{i,j} \frac{E_i E_j}{E_{vis}^2}, \qquad for\ |\cos\chi_k - \cos\chi_{ij}| < \Delta\cos\chi/2.$$

The shape of this matrix is shown in Fig. 5.12. One notices that away from the peak at ($\cos\chi_k = -1.0$, $\cos\chi_l = -1.0$), the off-diagonal terms are not negligible compared to the diagonal terms. We have studied the ASY function over the energy range $22\ GeV \leq \sqrt{s} \leq 46.7\ GeV$, see Fig. 5.13. We show below the results of the fits to α_s for both the IJ and Lund fragmentation models.

ϵ	22 GeV	35 GeV	41 GeV	44 GeV	46 GeV
0.07	.093±.045	0.117±.004	.088±.009	0.099±.006	.111±.012
0.10	.077±.035	0.122±.004	.090±.010	0.106±.007	.115±.012
0.13	.081±.038	0.126±.005	.094±.011	0.107±.008	.117±.012
0.15	.076±.040	0.129±.005	.097±.011	0.110±.008	.123±.013

Table 5.2 α_s measurements (IJ model) vs. ϵ cut. $\chi^2/D.o.f < 1.5$.

ϵ	22 GeV	35 GeV	41 GeV	44 GeV	46 GeV
0.07	.138±.051	.129±.004	.101±.011	.103±.007	.112±.013
0.10	.118±.055	.137±.005	.102±.012	.110±.008	.118±.015
0.13	.082±.040	.144±.006	.106±.013	.105±.009	.120±.016
0.15	.101±.040	.148±.006	.109±.013	.108±.009	.122±.016

Table 5.3 α_s measurements (Lund model) vs. ϵ cut. $\chi^2/D.o.f < 1.5$.

In order to study any dependence on the resolution cuts, we also determine α_s using the invariant mass cuts. The results are given below.

All the errors in tables 5.2, 5.3 and 5.4 are statistical only. A first striking feature of tables 5.2 and 5.3 are the large statistical errors for the 22 GeV results. The data sample at this energy is as large as the one for 41 GeV, Fig. 4.6, therefore the effect is not due only to statistics. There is physics behind this: the cross section for $e^+e^- \rightarrow q\bar{q}\gamma$ is expected to

Y_{cut}	0.02	0.03	0.04	0.05
35 GeV	.148±.004	.150±.005	.151±.005	.152±.005
44 GeV	.115±.006	.117±.007	.117±.007	.116±.007

Table 5.4 α_s measurements (Lund model) vs. Y_{cut}. $\chi^2/D.o.f < 1.5$.

dominate over the cross section for $e^+e^- \rightarrow q\bar{q}g$ at relatively low energies. Therefore the background to the three-jet event sample at low energies (say $\sqrt{s} < 25\ GeV$) is important. This is also one of the main reasons why we do not present results for $\sqrt{s} = 14\ GeV$ where the effect is even more noticeable.

We discuss now the main sources of systematic errors involved in the determination of α_s from the ASY function. These are:

1. Detector calibration and simulation: The shape of the ASY function is particularly sensitive to shifts in position measurements. In figure 5.14 we show the effect on the ASY function due to a an intentional shift in the z-position measurement. The shift was a linear function of z: $\Delta z = -a.z/L$, where L is the counter half-length and a a constant adjusted to produce shifts of 20 mm at the end of the counters. Such a shift is very conservative, since in practice one can correct for it by suitable calibration, as described in Chapter 4. The effect of detector simulation has been studied by using a second program, GHEISHA [5-9], as described in Ref. [5-10]. The total combined effects from these contributions to the systematic error is found to be $\sim 5\%$.

2. Acceptance: We studied two aspects of the acceptance. One due to the selection cut (i.e cut 70/50/50) and the other to the neglect of regions with small angle with respect to the beam axis (endcap region). The first effect was investigated by changing the cut to 50/50/50 and 50/60/60. While doing so, the acceptance was found to increase, namely from 75% to 85%, resulting also in an increase of the background contribution from tau-pairs, Bhabha and two-photon events. With the 50/60/60 cut we get: $\alpha_s = 0.118 \pm .004$ at $\sqrt{s} = 35\ GeV$ using the IJ model ($\epsilon = 0.10$). Comparing to table 5.2, we deduce a systematic shift of less than 5%. For the second effect, we analyzed the 1986 data

taking into account the endcap counters H and G, Fig. 3.7. This results in an improved energy resolution, as shown in the total energy plot, Fig. 5.15. The EEC and ASY functions, however, are insensitive to the inclusion of the H and G counters, Fig. 5.16. We conclude that the fact that the MarkJ detector does not cover the entire solid angle does not introduce any systematic errors.

3. Resolution cuts: These effects can be read off directly from tables 5.2, 5.3 and 5.4. We estimate them to be $\approx 7\%$.

4. $\cos\chi_0$ *cut*: This cut was set to -0.72 in the analysis in order to exclude most of the $q\bar{q}$ contribution to the ASY function, while keeping the statistics at a resonable level (the entries towards $\cos\chi = 0.$ have the largest statistical errors). In Fig. 5.17, we show the variation of α_s with respect to $\cos\chi_0$. There is no sign of systematic shift.

5. Fragmentation effects: The differences between the two models (IJ and Lund) reflect the systematic errors due to the lack of a theory of fragmentation. This is the largest source of systematic errors. We estimate it to be as large as 16%. Another possible source of errors is related to the mean transverse momentum of hadrons in the fragmentation process (σ_q parameter). Fig. 5.18 shows the variation of α_s versus σ_q for the Lund model. The effect on α_s is negligible.

Combining the results for the IJ and Lund models, and including the systematic errors (added in quadrature), we get the following results:

$$\alpha_s(35\ GeV) = 0.129 \pm 0.004 \pm 0.012 \tag{5.20}$$

$$\alpha_s(44\ GeV) = 0.108 \pm 0.007 \pm 0.010 \tag{5.21}$$

These values are combined results from the two (IJ and Lund) fragmentation models. One notices that systematic errors are smaller for $\sqrt{s} = 44\ GeV$, this is actually expected: fragmentation effects decrease as the energy increases (roughly a $1/\sqrt{s}$ fall). Using the variation of α_s versus $\sqrt{s}$, we can determine the QCD scale parameter Λ (in the $\overline{MS}$

ϵ	0.07	0.10	0.13	0.15
IJ Model	48±10	69±13	79±17	94±19
Lund 6.3	95±16	128±24	140±30	165±33

Table 5.5 Λ (MeV) in $\overline{MS}$ scheme vs. ϵ cut. ASY method.

scheme) by fitting the data to equation (2.12). The results are shown in table 5.5.

Including systematic errors, we get:

$$\Lambda = 70 \pm 13 \,^{+40}_{-32}\, MeV, \qquad (IJ\ Model) \tag{5.22}$$

$$\Lambda = 130 \pm 25 \,^{+70}_{-50}\, MeV, \qquad (Lund\ Model) \tag{5.23}$$

Combining the two models, we get:

$$\Lambda = 100 \pm 20 \,^{+80}_{-52}\, MeV \tag{5.24}$$

5.4 Determination of α_s from the PTC function

We have measured the PTC function over the energy range $22\ GeV \leq \sqrt{s} < 47\ GeV$. The integrated PTC over this range is shown in Fig. 5.19. We also show the measured distributions (with one angle fixed) for $d^2\Sigma^{\rm PTC}/d\chi_k d\chi_l$ compared to the MC predictions, Fig. 5.20. To fit α_s, we minimize the following χ^2:

$$\chi^2(\alpha_s) = \sum_{j=1}^{f} \frac{(\Sigma^{\rm PTC}_{j,Data} - \Sigma^{\rm PTC}_{j,MC})^2}{\sigma_j^2}, \tag{5.25}$$

where j refers to a cell in the (χ_k, χ_l) plane. Due to the symmetry of the PTC function in the interchange $\chi_k \leftrightarrow \chi_l$, and the β cut (*cf* 5.2.2), we have twelve degrees of freedom (*i.e* f=12) for a bin size $\Delta\chi = 10°$. Again, $\Sigma^{\rm PTC}_{j,MC}$ is determined as in Equation (5.6). We obtain the following results:

ϵ	22 GeV	35 GeV	41 GeV	44 GeV	46 GeV
0.07	.079±.013	.121±.004	.097±.008	.095±.006	.133±.011
0.10	.078±.013	.123±.004	.102±.008	.101±.007	.141±.012
0.13	.082±.013	.129±.005	.108±.009	.103±.007	.146±.013
0.15	.087±.014	.130±.005	.112±.009	.104±.008	.150±.013

Table 5.6 α_s measurements (IJ model) from PTC vs. ϵ cut.

ϵ	22 GeV	35 GeV	41 GeV	44 GeV	46 GeV
0.07	.118±.022	.149±.004	.121±.010	.119±.005	.137±.013
0.10	.105±.021	.151±.004	.124±.010	.128±.006	.145±.014
0.13	.098±.020	.154±.005	.128±.011	.126±.007	.144±.014
0.15	.097±.020	.155±.005	.131±.011	.130±.008	.148±.014

Table 5.7 α_s measurements (Lund model) from PTC vs. ϵ cut.

The systematic errors are estimated as for the ASY method. There are however two sources of errors specific to the PTC method: the dependence of the measurement on the planarity angle θ_p and the β cut. Varying θ_p between 0.08 rad and 0.12 rad we observe that α_s changes by $\approx$ 5%. In the same fashion, if we vary β from 20° to 60° we note that α_s changes by $\Delta\alpha_s = 0.01$, *i.e* an 8% systematic shift.

The resolution cuts introduce a 7% uncertainty as can be seen from tables 5.6 and 5.7. The dependence of α_s on σ_q (the mean transverse momentum in the fragmentation process)

is show in Fig. 5.20 : there is less than 2% variation in the α_s values. The difference between the two fragmentation models is, again, the major source of uncertainty: we estimate it to be 17% at $\sqrt{s} = 35\ GeV$. We can now combine results from the two models:

$$\alpha_s(35\ GeV) = 0.137 \pm 0.004 \pm 0.015 \tag{5.26}$$

$$\alpha_s(44\ GeV) = 0.114 \pm 0.006 \pm 0.012 \tag{5.27}$$

As a cross check, we also give α_s results when invariant-mass cuts are used:

Y_{cut}	0.02	0.03	0.04	0.05
35 GeV	.155±.004	.157±.004	.158±.005	.158±.005
44 GeV	.129±.003	.134±.004	.138±.004	.137±.004

Table 5.8 α_s measurements (Lund model) from PTC vs. Y_{cut}.

We can now fit the QCD scale parameter Λ, using the results of tables 5.6 and 5.7. We obtain the following values:

ϵ	0.07	0.10	0.13	0.15
IJ Model	52±10	64±11	78±15	92±18
Lund 6.3	199±24	240±30	244±34	262±37

Table 5.9 Λ (MeV) in $\overline{MS}$ scheme vs. ϵ cut. PTC method.

which we summarize as:

$$\Lambda = 65 \pm 12^{+45}_{-23}\ MeV, \qquad (IJ\ Model) \tag{5.28}$$

$$\Lambda = 240 \pm 30^{+65}_{-70}\ MeV, \qquad (Lund\ Model) \tag{5.29}$$

Again, combining the two models, we get:

$$\Lambda = 150 \pm 33^{+80}_{-74}\ MeV \tag{5.30}$$

5.5 Comparison between the two methods

In this section, we check the consistency of the results obtained by the two different methods. In the tables below, we show the differences in α_s values:

$\sqrt{s}$	22 GeV	35 GeV	41 GeV	44 GeV	46 GeV
IJ Model	.001±.037	.001±.006	.012 ±.012	.005 ±.010	.026±.017
Lund 6.3	.013 ±.060	.014±.006	.022±.016	.018±.010	.027±.021

Table 5.10 Differences in α_s values from the ASY and PTC methods. ($\epsilon = 0.10$).

The errors given are statistical only. Although, the Lund model appears to give larger differences, it is clear that such apparent discrepancies can be compensated for if we take into account the systematic errors. The combined values at 35 GeV and 44 GeV show good agreement, as seen by comparing results (5.20) to (5.26) and (5.21) to (5.27) respectively. So does the value of the scale parameter Λ. We also observe that both models show a systematic shift between the measured α_s values when using the IJ and Lund fragmentation models.

5.6 Running of α_s

In the energy range we studied, *i.e* $22\ GeV \leq \sqrt{s} < 47\ GeV$, α_s is expected to vary by $\sim 12\%$. Such a variation is contained in the errors on our measured α_s values. Therefore, from this study alone, one can only say that our measured α_s is not inconsistent with the "running" phenomenon. However, measurements of α_s at lower center of mass energies are available. Therefore, one can combine results and test the running of α_s.

At lower energies, α_s has been determined from the decay widths of quarkonia resonances, namely Υ and Υ' [5-11], and from Deep Inelastic Scattering (DIS) experiments [5-12].

The obtained α_s values from the first method using Υ radiative decay ratio $\Gamma(\Upsilon \rightarrow g + hadrons)/\Gamma(\Upsilon \rightarrow hadrons)$ are:

$$\alpha_s(0.157 M_\Upsilon) = 0.226^{+0.067}_{-0.042} \qquad from\ \Upsilon\ decay,$$

$$\alpha_s(0.157 M_{\Upsilon'}) = 0.197^{+0.123}_{-0.055} \qquad from\ \Upsilon'\ decay,$$

whereas using $\Gamma(\Upsilon \rightarrow hadrons)/\Gamma(\Upsilon \rightarrow \mu\mu)$ at a higher energy yields:

$$\alpha_s(0.48 M_\Upsilon) = 0.165^{+0.006}_{-0.005} \qquad from\ \Upsilon\ decay,$$

$$\alpha_s(0.48 M_{\Upsilon'}) = 0.197^{+0.026}_{-0.018} \qquad from\ \Upsilon'\ decay.$$

The second α_s determination from DIS experiments gives the following result at $\sqrt{s} = 10\ GeV$:

$$\alpha_s(10\ GeV) = 0.165 \pm 0.030$$

In Fig. 5.22, we show these results together with our determined α_s values at higher energies. We now use all these values to fit the QCD scale parameter Λ. The result is:

$$\Lambda = 82 \pm 10 \quad (MeV),$$

where the error is statistical only. The χ^2 of the fit was found to be 1.5 (per degree of freedom). A constant value for α_s is ruled out by these data. We deduce from this analysis that α_s is "running". The observed decrease is consistent with the QCD logarithmic prediction, Equation 2.12.

Chapter 6

Conclusions

This study was aimed at improving our understanding of the evolution of hadronic final states in e^+e^-annihilations. We have concentrated on the determination of the strong coupling constant α_s, as well as testing fragmentation models (see Appendix B). We have used two methods relying on two independent variables in order to measure α_s: the Asymmetry of the Energy-Energy correlations function (ASY), and the Planar Triple energy Correlations function (PTC). These two variables have been shown to be suitable for such measurements due, mainly, to their infrared stability, small second order QCD corrections and small variation with $\sqrt{s}$. This is not the case for variables like thrust and oblateness. We obtained the following values for α_s:

$$\text{ASY Method}: \begin{cases} \alpha_s(35\ GeV) = 0.129 \pm 0.004 \pm 0.012 \\ \alpha_s(44\ GeV) = 0.108 \pm 0.007 \pm 0.010 \end{cases}$$

and

$$\text{PTC Method : } \begin{cases} \alpha_s(35\,GeV) = 0.137 \pm 0.004 \pm 0.015 \\ \alpha_s(44\,GeV) = 0.114 \pm 0.006 \pm 0.012 \end{cases}$$

The major source of systematic errors comes from fragmentation effects for which only phenomenological models exist. We determine the QCD scale parameter Λ_{MS} from our α_s measurements in the energy range $22\,GeV \leq \sqrt{s} < 47\,GeV$:

$$\Lambda = 100 \pm 20\,^{+80}_{-52} \qquad \text{ASY Method,}$$

$$\Lambda = 150 \pm 33\,^{+80}_{-74} \qquad \text{PTC Method.}$$

Using our results together with α_s values from lower energy experiments, we deduce that a running α_s is strongly favored over a constant α_s.

A comparison to results from similar experiments (Appendix A) shows that the apparent discrepancies between the α_s values published in 1982-1983 are now well understood. They are traced back to non-exact 2^{nd} order QCD calculations used by some collaborations. All experiments using the ERT calculation obtain consistent results.

We also observe that cluster fragmentation models using LLA calculations (parton showers) do not provide a good description of our data. We obtain much better fits when using them with fixed order matrix elements.

We conclude that QCD predictions are consistent with our data. However, we still lack a complete theoretical description of hadronic final states due to the ambiguity introduced by the fragmentation process. Future improvements should concentrate on the following:

- Parton level: use 3^{rd} or higher order QCD calculations. Unfortunately, this seems unlikely in the near future due its complexity. Alternate methods to fixed order matrix elements are LLA calculations. However, as they stand at the present time, they do not provide a good description of data (see Appendix B). A refinement of QCD calculation seems strongly indicated.

- Fragmentation effects: Ideally, these should be associated with parton generation in a single theory. To date, however, their factorization seems more realistic. The semi-phenomenological models commonly used, do provide a reasonably good description of data. Models relying on the color string picture appear more appealing, although our data does not rule out independent jet models. Since the fragmentation models are phenomenological, their parameters can alwyas be tuned to reproduce data. This approach is more likely to prevail unless a major breakthrough occurs.

- study higher energy regions: This can be reached with the advent of high energy colliders (TRISTAN, SLC, and in the near future LEP). In addition to the usual excitement (and surprises!) of probing higher energy regions, one can already see three advantages. The first one is the reduction of fragmentation effects which are expected to decrease with increasing center of mass energy. Pure QCD effects will then be dominant. The second advantage is the possibility of studying multi-jet events which constitute signatures of high order QCD effects. The third one is to measure α_s at higher energies and test more rigourously one the major predictions of QCD: asymptotic freedom. Furthermore, a study of the Z^0 peak region will be possible at SLC and LEP. The biggest advantage in such a study is the substantial suppression of QED radiative effects, hence permitting a "cleaner" study of QCD.

Appendix A

Comparison with other experiments

In this appendix, we present a summary of α_s measurements from PETRA and PEP experiments. All experiments initially used shape variables, like thrust, to determine α_s and did not include complete 2^{nd} order calculations. However, as seen in Chapter 5, on cne hand, 2^{nd} corrections were shown to be improtant, and on the other hand, the shape variables were found to be not "safe" quantities. As a next step, practically all collaborations included 2^{nd} order calculations, and used the safer method relying on the Asymmetry of Energy-Energy correlations. Again, some serious discrepancies were noticed among the measured α_s values [A-1]. These conflicting results were traced back to the bias introduced by the approximations used in some $O(\alpha_s^2)$ calculations, like the ones of Ref. [2-18b]. Indeed, all discrepancies disappeared when the different groups used the same QCD calculation. This short historical note is summarized in Fig. A-1. In this comparison, we consider only the α_s measurements using the ASY method. In the table below we give a summary of these measurements.

Experiment	QCD $O(\alpha_s^2)$	Fragm. Model	α_s	Ref.
MARK-J	ERT	IJ	0.122 ± 0.004	This
	ERT	Lund 6.3	0.137 ± 0.005	thesis
JADE	GKS	Lund	0.165 ± 0.01	[A-2]
	GKS	Indep.	$0.11 - 0.14$	"
	ERT	*	0.12 ± 0.02	[A-3]
CELLO	GKS	Lund	0.19 ± 0.02	[A-4]
	GKS	Indep.	$0.12 - 0.15$	"
PLUTO	ERT	Lund	0.145 ± 0.006	[A-5]
	ERT	IJ	0.135 ± 0.006	"
TASSO	FSSK	Lund	0.190 ± 0.009	[A-6]
	FSSK	Indep.	$0.11 - 0.16$	"
	ERT	Lund	0.159 ± 0.012	"
	ERT	Indep.	$0.12 - 0.13$	"
MAC (29 GeV)	GKS	Lund	0.185 ± 0.013	[A-7]
	GKS	Indep.	$0.105 - 0.140$	"
PLUTO	ERT	Lund	0.147 ± 0.010	[A-8]
+TASSO	ERT	IJ	0.142 ± 0.010	"

Table A.1

Comparison of measured $\alpha_s(35 \ \ GeV)$ from PETRA + PEP experiments using the ASY method.

The quoted errors are statistical only. The "Indep." fragmentation model refered to in table A.1 indicates that the collaboration used various options of the IJ model. These

options mainly concern the gluon fragmentation and conservation of energy-momentum. In the IJ model used by the Mark-J collaboration, a gluon is assumed to fragment as a $q\bar{q}$ pair, and energy-momentum conservation is imposed via a Lorentz boost. The ERT calculation refers to the calculation used by the MarkJ group (based on Ref. [2-18a]), whereas GKS and FSSK refer to those of Ref. [2-18b]. The result using the "*" fragmentation model for the Jade Collaboration has been determined using a $\propto 1/\sqrt{s}$ fragmentation law.

One notices that the GKS/FSSK calculation gives systematically larger α_s values. This problem is now well understood and is due to missing terms in the matrix elements. Measurements using the same analysis methods do agree however. Taking into account the different fragmentation models, we deduce :

$$0.10 < \alpha_s(35 \quad GeV) < 0.17$$

when the ERT calculation is used.

Appendix B

Tests of Cluster Models

We mentioned in Chapter 2 a third class of fragmentation models, the so-called cluster models, which we did not use in the determination of α_s. In this appendix, we will test one of these models: the Caltech cluster model (CIT), version II [B-1]. In its original version, this model uses partons generated using the Leading Log Approximation (LLA). In this study, we will use the cluster fragmentation using both LLA partons and the MarkJ partons, which we refer to as ERT partons (Sec. 5.1.1). The CIT model evolves in three stages:

- Parton Generation.
- Formation and evolution of string systems.
- Low mass cluster hadronization.

We now briefly introduce these three stages and then present tests of the two versions of the model: ERT+CIT and LLA+CIT.

B.1 LLA Parton showers

There are two approaches to parton generation in e^+e^-annihilations: fixed order matrix elements (like ERT, GKS and FSSK) and LLA parton showers. Fixed order matrix elements have been traditionally used by experimentalists to test QCD (*e.g* to determine α_s). One may ask why not to keep fixed order matrix elements which have been so far quite successful in describing the data. This is motivated mainly by the following considerations:

1) At higher energies than presently available, *e.g* SLC and LEP, we expect higher order jet events (*i.e* 4-jet, 5-jet events, etc..). This implies that higher order QCD effects would become important. This is akin to the necessity of $O(\alpha_s^2)$ calculation to describe properly 3-jet events. Unfortunately, an $O(\alpha_s^3)$ QCD calculation does not seem imminent.

2) It has been reported by the Jade collaboration [B-2] that existing QCD calculations do not properly describe the observed 4-jet event rate. They determine that such rate is underestimated by a factor of 2.

LLA calculations are an alternative to fixed order matrix elements methods. They rely on a summation of all leading terms in the perturbative QCD expansion. Non-leading terms are neglected (in contrast to fixed order matrix elements). Practically, the idea is to let the primary quarks (q and $\bar{q}$ from the e^+e^-collision) split into quarks and gluons. These produced partons split again. The process yields the so-called "parton shower" which stops when the parton invariant mass reaches the value of the QCD scale parameter Λ_{QCD}. The perturbative splittings are generated according to the following probability:

$$d\mathbf{P} = \frac{dt}{t}\frac{\alpha_s(t)}{2\pi}dz P_{A/B}(z), \qquad (B.1)$$

where t is the squared mass of the parent parton and $P_{A/B}(z)$ is the appropriate Atarelli-Parisi function of the splitting variable z [B-3]. For instance, the Altarelli-Parisi

function for the bremsstrahlung process $q \rightarrow qg$ is given by:

$$P_{q\rightarrow qg}(z) = \frac{4}{3}\frac{1+z^2}{1-z}.$$

The formalism involves only two parameters: the LLA QCD scale Λ_{QCD} (not to be confused with $\Lambda_{\overline{MS}}$), and a cutoff t_0 on shower evolution.

B.2 String evolution and Hadronization

The large distance color separations in QCD are usually viewed through the creation of $q\bar{q}$ pairs. A simple phenomenological picture for a confined, *colorless* $q\bar{q}$ system of center of mass energy W is the "yo-yo" model [B-4]. In this picture, the $q\bar{q}$ pair is confined to a *string* by a constant magnitude force:

$$\frac{d\vec{p}}{dt} = \pm\kappa\hat{p}. \qquad (B.2)$$

Subsequent pair creations are due to the breaking of the string. In the CIT model, the probability for breaking is uniform:

$$d\mathbf{P}_{break} = \mathbf{P}_0 dA\,, \qquad \mathbf{P}_0 \textit{ constant}\,, \qquad (B.3)$$

where $dA = dldt\sqrt{(1-v_\perp^2)}$ is the invariant area swept out by the string; t is the time coordinate, and l and $v_\perp$ are, respectively, the position along the string and transverse velocity of string element $d\vec{l}$. This string model evolution of a cluster of mass W is terminated by the following cut-off procedure:

$$\mathbf{P}_{break} = \begin{cases} 0 & \text{if } W < W_0, \\ 1\text{-e}^{-\rho(W-W_0)^2/2} & \text{if } W > W_0 \end{cases} \qquad (B.4)$$

where

$$\rho \equiv \mathbf{P}_0/\kappa^2 \, , and \qquad W_0 \equiv W_{th} + W_{max}, \tag{B.5}$$

W_{th} is the two particle threshold for the particular flavor of the parent cluster, and W_{max} is a cutoff parameter. Breaks are allowed at all positions along the string. If a break occurs near one end of the string, creating a "smaller" string of mass W_1, and such that:

$$W_1 < W_{th} + W_{min},$$

then this "small" cluster is identified with a single hadron. W_{min} is a second cutoff parameter. The model parametrizes experimental data to describe the hadronization of low mass systems.

The default values used for the five mentioned parameters are:

$$\Lambda_{QCD} = 0.3 - 0.7 \, GeV \qquad t_0 = 1 - 2 \, GeV^2,$$

$$W_{max} = 2.2 \pm 0.3 \, GeV \qquad W_{min} = 0.25 \pm 0.1 \, GeV,$$

$$\rho = 1.6 \pm 0.3 \, GeV.$$

B.3 Tests of the Model

In this section, we test the CIT model by comparing its predictions for various distributions to the MarkJ data, corrected for detector acceptance, radiative corrections and selection criteria. Any distribution X is corrected, bin by bin, as follows:

$$X(corrected) = X(measured) \frac{X(MC \; with \; ideal \; detector)}{X(Full \; MC \; simulation)}.$$

We examine separately the two options for the model: LLA+CIT and ERT+CIT.

B.3.1 LLA+CIT Model

The first variable we study is Thrust (Equ. 5.7). Fig. B.1 shows the expected distribution for various values of ρ, whereas Fig. B.2 is a similar plot for Major (Equ. 5.9). It is observed that the model is too high for low-thrust events and too low for high-thrust events. Similar remarks apply to the Major plot. Varying W_{max} and W_{min} does not cure the problem, Fig. B.3 and B.4. One would ultimately get some improvement for either the low-thrust region *or* the high-thrust region by going to much lower values of ρ or decreasing Λ_{QCD}. However, we were not able to find a set of parameters that correctly describes the Thrust and Major distributions. The ASY (Equ. 5.12) function is also not well described by the model, Fig. B.5. Variations of ρ, W_{max} and W_{min} did not improve the situation. All parameters which are not varied in the various plots were set to the above default values.

B.3.2 ERT+CIT Model

In this approach, we generate partons using the ERT matrix elements and then use the CIT fragmentation scheme. Our study of different shape variables has led us to require much smaller ρ values than those used with LLA partons. In Fig. B.6 and B.7, we show the distributions for Thrust and Major. For $0.2 \leq \rho \leq 0.3$, we get good agreement between ERT+CIT and data. The ASY function is plotted in Fig. B.8. We observe the strong dependence of the predicted distribution on the parameter ρ. The agreement with data is best with $\rho \sim 0.3$, in agreement with the preferred value from the Thrust and Major distributions. As a final test, we show the particle flow of three-jet events (Flower plot), Fig. B.9. The three-jet events were selected by requiring a large value of the Oblateness (Equs. 5.10): $O_b > 0.3$. The agreement is reasonable except at the lower regions of the plot. It appears that the CIT model overestimates the string effect [B-5], in which fewer hadrons are produced between the fastest two jets in a three-jet event than in the regions between the other two jets.

B.4 Conclusions

An immediate conclusion is that the LLA calculation does not seem to describe properly

the measured shape variables. Second order QCD calculations give better agreement with data. The fragmentation process itself was shown to give reasonable results. The more conventional models (IJ and Lund) have more freedom in parameter tuning (like fragmentation functions and mean transverse momentum), and, consequently, yield better fits to data. This tuning option is much more limited in cluster models due to the smaller number of parameters. The CIT-II model has been shown, however, to give good descriptions of other distributions, such as charge multiplitcities and rapidity, see Ref. [B-1].

References

[2-1] M. Gell–Mann, Phys. Lett. 8 (1964) 214;
G. Zweig, CERN Preprints TH 401 (1964); TH 412 (1964).

[2-2] Y. Ne'eman, Nucl. Phys. 26 (1961) 222;
M. Gell–Mann, Phys. Rev. 125 (1962) 1067.

[2-3] E. D. Bloom *et al.*, Phys. Rev. Lett. 23 (1969) 930.

[2-4] J. D. Bjorken Phys. Rev. 179 (1969) 1547.

[2-5] O. W. Greenberg, Phys. Rev. Lett. 13 (1964)598.

[2-6] D. P. Barber *et al.*, Phys. Rev. Lett. 43 (1979) 830.

[2-7] R. Brandelik *et al.*, Phys. Lett. 86B (1979) 243;
Ch. Berger *et al.*, Phys. Lett. 86B (1979) 418;
W. Bartel *et al.*, Phys. Lett. 91B (1980) 142.

[2-8] H. Fritzsch and M. Gell–Mann, Proc. 16*th* Int. Conf. on High Energy Physics, Chicago–Batavia (NAL, Batavia, 1972) Vol. 2, p. 135.

[2-9] C. N. Yang and R. L. Mills Phys. Rev. 96 (1954) 191.

[2-10] C. Itzykson and J. B. Zuber, "Quantum Field Theory", Mc Graw Hill, New York, N.Y. (1980).

[2-11] S. L. Glashow, Nucl. Phys. 22 (1961) 579;
S. Weinburg, Phys. Rev. Lett. 19 (1967) 1264; Phys. Rev. D5 (1972) 1412;
A. Salam, in: Elementary Particle Theory,
ed. N. Svartholm (Stockholm, 1968)p 361;
S. L. Glashow, J. Ilipoulos and L. Maiani; Phys. Rev. D2 (1970) 1285;
J. Ellis and M. K. Gaillard, CERN 76-1 (1976).

[2-12] G. Kramer, Theory of Jets In Electron–Positron Annihilation (Springer, Hamburg, 1984).

[2-13] J. Ellis, M. K. Galliard and G. G. Ross, Nucl. Phys. B111 (1976) 253;
(Erratum B130 (1977) 516).

[2-14] G. Sterman and S. Weinberg, Phys. Rev. Lett. 39 (1977) 1436.

[2-15] M. Dine and J. Sapirstein, Phys. Rev. Lett. 43 (1979) 668;
K. G. Chetyrkin, A. L. Kataev and F. V. Tkachov,
Phys. Lett. 85B (1979) 277;
W. Celmaster and R. J. Gonsalves, Phys. Rev. Lett. 44 (1979) 560;
Phys. Rev. D21 (1979) 3112.

[2-16] W. A. Bardeen, A. J. Buras, D. W. Duke and T. Muta,
Phys. Rev. D18 (1978) 3998;
A. J. Buras, Rev. Mod. Phys. 52(1980) 199;
M. J. Marciano, Phys. Rev. D29 (1984) 580.

[2-17] T. D. Gottschalk, Phys. Lett. 109B (1982) 331.

[2-18a] R. K. Ellis, D. A. Ross and A. G. Terrano,
Phys. Rev. Lett. 45 (1980) 1226; Nucl. Phys. B178 (1981) 421;
R. K. Ellis and D. A. Ross, Phys. Lett. 106B (1981) 88;
J. A. M. Vermaseren, K. J. F. Gaemers and S. J. Oldham,
Nucl. Phys. B187 (1981) 301.

[2-18b] K. Fabricius, I. Schmidt, G. Schierholz and G. Kramer,
Phys. Lett. 97B (1980) 431;
Phys. Rev. Lett. 97B (1980) 431;
Z. Physik C11 (1982) 315;
B. Lampe and G. Kramer, DESY Report 82–025 (1982);
F. Gutbrod, G. Kramer and G. Schierholz, Z. Physik C21 (1984) 235.

[2-18c] B. Lampe and G. Kramer, DESY Report 86–119 (1986).

[2-18d] T. D. Gottschalk and M. P. Schatz,
Cal. Tech. Reports CALT–68–1173 (1985); CALT–68–1173 (1985);
Phys. Lett. 150B (1985) 451.

[2-19] R. Y. Zhu, Ph.D Thesis, MIT (1983).

[2-20a] R. D. Field and R. P. Feynman, Nucl. Phys. B136 (1978) 1.

[2-20b] P. Hoyer *et al.*, Nucl. Phys. B161 (1979) 349.

[2-20c] A. Ali *et al.*, Z. Phyisk C1 (1979) 203; C1 (1979) 269;
Phys. Lett. 83B (1979) 375; Nucl. Phys. B168 (1980) 490.

[2-21a] B. Andersson and G. Gustafson, Z. Physik C3 (1980) 223;

B. Andersson, G. Gustafson, and T. Sjöstrand,
Z. Physik C6 (1980) 235; Nucl. Phys. B197 (1982) 45;
G. Gustafson, Z. Physik C15 (1982) 155;
T. Sjöstrand, Comput. Phys. Commun. 27 (1982) 243; 28 (1983) 229.

[2-21b] T. Sjöstrand, Comput. Phys. Commun. 39 (1986) 347;
T. Sjöstrand and M. Bengtsson, Lund Report LU-TP 86-22 (October 1986).

[2-22] G. C. Fox and S. Wolfram, Nucl. Phys. B168(1980) 285;
R. D. Field and S. Wolfram, Nucl. Phys. B213(1983) 65;
B. R. Weber, Nucl. Phys. B238 (1984) 492;
T. D. Gottschalk, Nucl. Phys. B214(1983) 201;
Nucl. Phys. B239(1984) 325; Nucl. Phys. B239(1984) 349.

[3-1] PETRA Proposal (Updated Version), DESY (1976).

[3-2] D. P. Barber *et al.*, the MARK J Collab., Phys. Rep. 63 (1980) 337;
B. Adeva *et al.*, the MARK J Collab., Phys. Rep. 109 (1984) 131.

[3-3] A. H. Walenta, Proc. Intern. Conf. on Instr. for Colliding Beam Physics,
SLAC-250 (1982)

[3-4] G. Viertel, Wire Chamber Conference, Vienna (Austria), Feb. 1986;
M. Dhina, M.Sc. Thesis, MIT, (1985).

[4-1] M.–C. Ho, Ph.D. Thesis, NIKHEF, Amsterdam (1983).

[5-1] F. A. Berends, R. Kleiss, Nucl. Phys. B177 (1981) 237;
B178 (1981) 141.

[5-2] Z. Kunszt Phys. Lett. 99B (1981) 429; 107B (1981) 123.

[5-3] A. DeRújula *et al.*, Nucl. Phys. B138 (1978) 387;
E. Farhi, Phys. Rev. Lett. 39 (1977) 1587.

[5-4] R. B. Clare, Ph.D Thesis, MIT (1982).

[5-5] C. L. Basham *et al.*Phys. Rev. Lett 41 (1978) 1585;
Phys. Rev. D21 (1979) 2018.

[5-6] L. S. Brown and S. D. Ellis Phys. Rev. D24 (1981) 2383.

[5-7] S. D. Ellis *et al.*Nucl. Phys. B229 (1983) 317;
A. Ali and F. Barreiro Phys. Lett. B118 (1982) 155.

[5-8] F. Csikor *et al.*Phys. Rev. D31 (1985) 1025.

[5-9] H. Fesefeldt, RWTH Aachen, Report PITHA 85/02 (1985).

[5-10] M. H. Capell, Ph.D Thesis, MIT (1986).

[5-11] S. J. Brodsky *et al.*, Phys. Rev. D28 (1983) 228;
P. Avery *et al.*, Phys. Rev. Lett. 50(1983) 807.

[5-12] G. Altarelli, Proc. Intern. Europhysics Conf. on
High Energy Physics (Bari) 1985.

[A-1] P. Söding, Proc. Intern. Europhysics Conf.
on High Energy Physics (Brighton) 1983;
J. Dorfan, Proc. Intern. Symp. on Lepton and Photon Interactions
at High Energies, (Cornell) 1983

[A-2] W. Bartel *et al.*, Zeit f. Phys. C25(1984) 231.

[A-3] S. Bethke , Proc. Intern. Europhysics Conf. on High Energy Physics (Berkeley) 1986;
Desy Report 86-115.

[A-4] H. J. Behrend *et al.*, Phys. Lett. 138B(1984) 311.

[A-5] Ch. Berger *et al.*, Zeit f. Phys. C28(1985) 365.

[A-6] M. Althoff *et al.*, Zeit f. Phys. C26(1984) 157.

[A-7] E. Fernandez *et al.*, Phys. Rev. D31 (1985) 2724.

[A-8] F. Barreiro, Desy Report 85-086.

[B-1] T. D. Gottschalk and D. A. Morris, Caltech Report
CALT-68-1365 (1986).

[B-2] W. Bartel *et al.*, Desy Report DESY 86-086.

[B-3] G. Altarelli and G. Parisi, Nucl. Phys. B126 (1977) 298.

[B-4] X. Artru and G. Mennessier, Nucl. Phys. B270 (1974) 93;
B. Andersson, G. Gustafson, and C. Peterson, Z. Physik C1 (1979) 105.

[B-5] W. Bartel *et al.* Z. f. Phys. C21 (1983) 37;
Phys. Lett. 157B (1985) 340;
H. Aihara *et al.*, Phys. Rev. Lett. 54(1985) 270.

Figure Captions

1.1: Space-time diagram for hadron production in e^+e^- annihilation.
The curly line represent gluons.

2.1: QCD Feynman rules.

2.2: QCD diagrams for $e^+e^- \rightarrow$ *hadrons*:

a) 0^{th} order diagram for $e^+e^- \rightarrow q\bar{q}$;

b) 1^{st} order diagrams for $e^+e^- \rightarrow q\bar{q}g$;

c) 1^{st} order virtual diagrams for $e^+e^- \rightarrow q\bar{q}g$;

d) 2^{nd} order diagrams for $e^+e^- \rightarrow 4 - partons$.

2.3: QCD diagrams for $e^+e^- \rightarrow$ *hadrons*:

a) 2^{nd} order virtual diagrams for $e^+e^- \rightarrow q\bar{q}g$;

b) 2^{nd} order virtual diagrams for $e^+e^- \rightarrow q\bar{q}$.

2.4: Schematic description of fragmentation models:

a) Independent model of Ali *et al.*.

b) Space time evolution of strings in the Lund model.

2.5: Schematic description of fragmentation models:

a) Kink in the string due to gluon emission (lund model);

b) QCD parton shower with string fragmentation;

c) Same as b) but with cluster fragmentation.

3.1: a) Setup of the PETRA storage ring and experiments;

b) Injection apparatus for PETRA.

3.2: The MarkJ Detector:

(a) Side view;

(b) End view.

3.3: Side view of one half of the inner part of MarkJ.

3.4: Schematic description of the detector layers.

3.5: MarkJ Time Expansion Chamber (TEC):

a)End view;

b)Half segment of TEC showing drift and detection regions.

3.6: a) Side view of one half of the drift tube arrays;

b) Reconstructed vertex position from Bhabha events.

3.7: Small polar angle detector region.

3.8: Electromagnetic calorimeter:

Counter-wise energy distributions for 1986 Data versus Monte Carlo:

a) A counters;

b) B counters;

c) C counters.

3.9: Hadronic calorimeter:

Counter-wise energy distributions for 1986 Data versus Monte Carlo:

a) K_{12} counters;

b) K_3 counters;

c) $K-4$ counters.

4.1: Visible energy distribution for hadronic data after all cuts.

4.2: Transverse and longitudinal energy distributions.

4.3: Visual scan display of a hadronic event: side view of detector.

4.4: Same as 4.3: end view of detector.

4.5: Same as 4.3: Fitted tracks in drift tubes.

4.6: Total number of selected hadronic events versus center of mass energy.

4.7: a) Schematic description of a counter element with two photomultipliers;

b) Illustration of the various timings used to determine the z position from TDC's (see Sec. 4.4).

4.8: Counter calibration for 1986 data:

a) $Z_{tube} - Z_{TDC}$ distribution for A counters;

b) $Z_{tube} - Z_{ADC}$ distribution for A counters.

4.9: Counter calibration for 1986 data:

a) $Z_{tube} versus Z_{tube} - Z_{TDC}$ plot for A counters;

b) $Z_{tube} versus Z_{tube} - Z_{ADC}$ plot for A counters.

5.1: a) Thrust distribution dependence on ϵ cuts;

b) Oblateness distribution dependence on ϵ cuts.

5.2: a) Integrated thrust dependence on invariant mass cut. The left scale (circles with error bars) is for full Monte carlo simulation, including detector effects and radiative corrections, whereas the right scale (solid line) is for parton level;

b) Same plot for oblateness.

5.3: a) Dependence of the energy-energy correlation function on ϵ cuts;

b) Dependence of the asymmetry function on ϵ cuts.

5.4: a) Dependence of the energy-energy correlation function on invariant mass cuts;

b) Dependence of the asymmetry function on invariant mass cuts.

5.5: Integrated asymmetry dependence on ϵ cuts. The circles with error bars (left scale) are for full monte carlo simulation whereas the full line (right scale) is for parton level.

5.6: 1986 data: three dimensional plot showing the planar triple energy correlation function. The peaks at $\chi_{1(2)}$ are due to $q\bar{q}$ final states and $q\bar{q}g$ final states where the emitted gluon is either soft or collinear to one of the quarks. The contribution of three-jet events is most dominant in the inner valley.

5.7: Dependence of the planar triple energy correlation function on ϵ cuts. In the two histograms one of the angles is fixed.

5.8: Dependence of the planar triple energy correlation function on invariant mass cuts. In the two histograms one of the angles is fixed.

5.9: Integrated triple energy correlation function dependence on ϵ cuts. The left and right scales are as for 5.5.

5.10: 35 GeV data versus monte carlo: energy energy correlations and asymmetry functions.

5.11: Same as 5.10 at 44 GeV.

5.12: Bin to bin correlations for the asymmetry function. Note that some entries are negative.

5.13: Total integrated asymmetry for data versus center of mass energy.

5.14: Study of the effect of a shift in z positions on the asymmetry function.

5.15: Total visible energy distribution with/without the H and G endcap counters.

5.16: Energy energy correlation and asymmetry functions with/without H and G counters.

5.17: Variation of α_s (from ASY) with the $\cos\chi_0$ cut.

5.18: Variation of α_s (from ASY) with the mean transverse momentum σ_q.

5.19: Total integrated PTC for data versus center of mass energy.

5.20: 1986 data (35 GeV) versus Monte carlo: PTC distributions with one angle fixed.

5.21: Variation of α_s (from PTC) with the mean transverse momentum σ_q.

5.22: α_s versus center of mass energy: solid lines are QCD predictions for various Λ values. The low energy data are from Deep Inelastic Scatering experiments and Υ decays.

A.1: α_s results: comparison with other experiments. Note the big discrepancies in the period 1983-1984. The recent results are in much better agreement.

B.1: Thrust distribution: corrected data versus LLA + CIT for different ρ values.

B.2: Major distribution: corrected data versus LLA + CIT for different ρ values.

B.3: Thrust distribution: corrected data versus LLA + CIT for different W_{max} values.

B.4: Thrust distribution: corrected data versus LLA + CIT for different W_{min} values.

B.5: Asymmetry function: corrected data versus LLA + CIT. All parameters set at default values (see Appendix B).

B.6: Thrust distribution: corrected data versus ERT + CIT for different ρ values.

B.7: Major distribution: corrected data versus ERT + CIT for different ρ values.

B.8: Asymmetry function: corrected data versus ERT + CIT for different ρ values.

B.9: Flower plot (particle flow of three jet events in thrust-major plane): data versus ERT + CIT. Note that ERT + CIT overestimates the string effect.

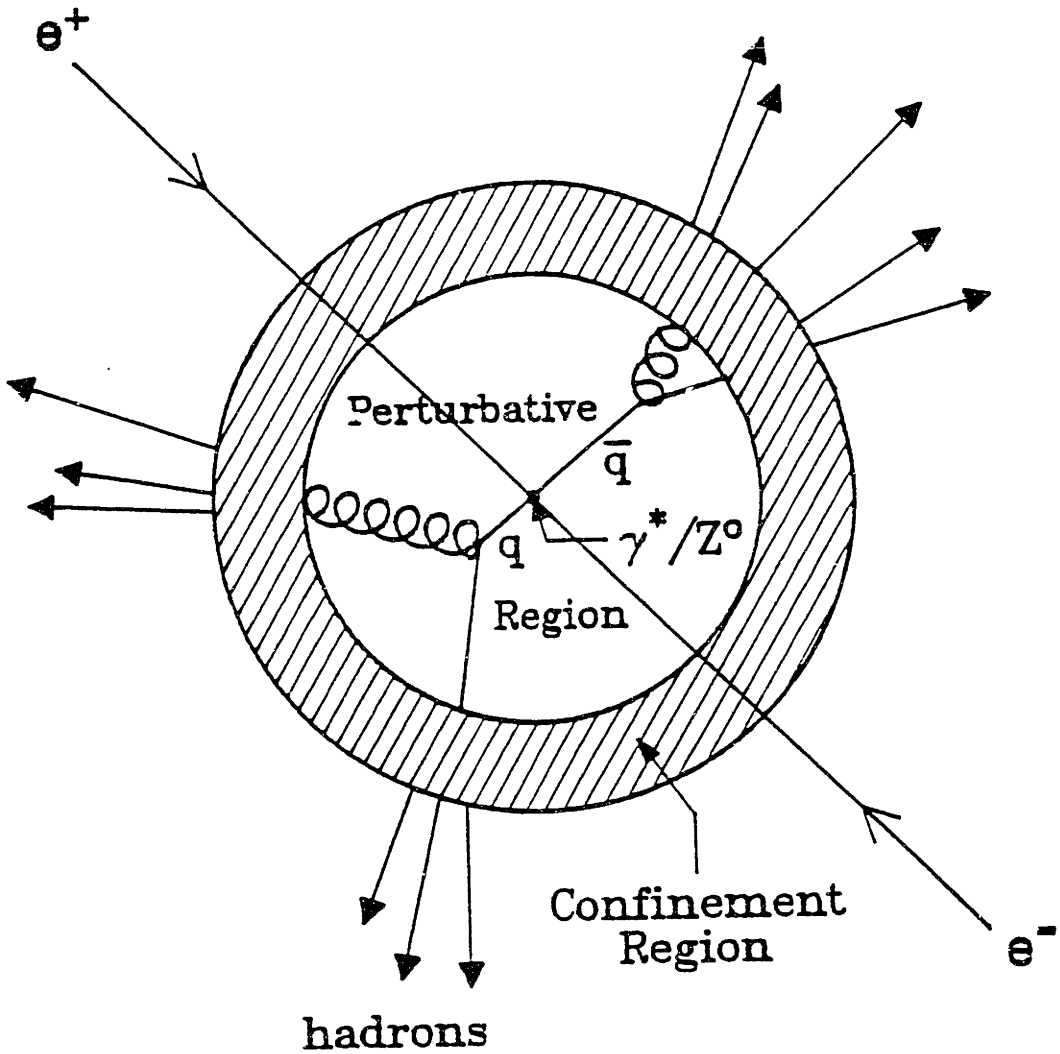

Figure 1.1

Fermion Propagator: $b \quad p \quad a \;\; \beta \quad\quad \alpha \;=\; \left(\frac{i}{\gamma \cdot p - m}\right)_{\alpha\beta} \delta_{ab}$

Gluon Propagator: $j \quad k \quad i \;\; \nu \quad\quad \mu \;=\; \frac{-i}{k^2}\left[g_{\mu\nu} - (1-\lambda)\frac{k_\mu k_\nu}{k^2}\right]\delta_{ij}$

Ghost Propagator: $j \quad k \quad i \;=\; \frac{i}{k^2}\,\delta_{ij}$

Gluon-Quark Vertex:

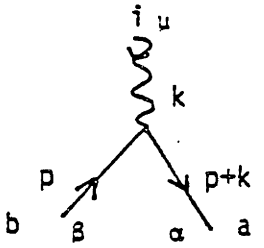

$= i g (\gamma_\mu)_{\alpha\beta} \left(\frac{\lambda}{2}\right)_{ab}$

Gluon-Ghost Vertex:

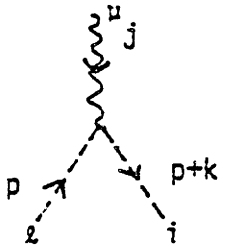

$= - g\, f_{ij\ell}(p+k)_\mu$

3-Gluon Vertex:

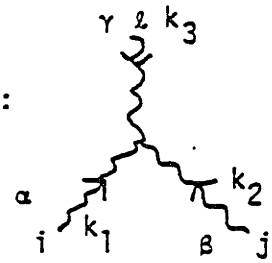

$= g f_{ij\ell}[g_{\alpha\gamma}(k_3-k_1)_\beta + g_{\beta\alpha}(k_1-k_2)_\gamma + g_{\gamma\beta}(k_2-k_3)_\alpha]$

4-Gluon Vertex:

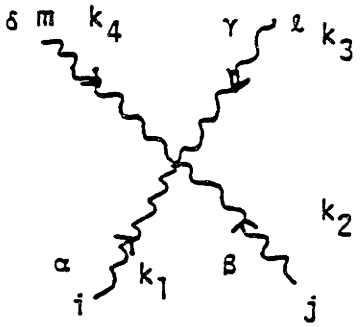

$$= - i g^2 \{ f_{ij} f_{m\ell} (g_{\alpha\delta} g_{\beta\gamma} - g_{\alpha\gamma} g_{\beta\delta}) + f_{im} f_{rj\ell} (g_{\alpha\beta} g_{\gamma\delta} - g_{\alpha\gamma} g_{\beta\delta}) + f_{ri\ell} f_{rjm} (g_{\alpha\beta} g_{\gamma\delta} - g_{\alpha\delta} g_{\beta\gamma}) \}$$

Figure 2.1

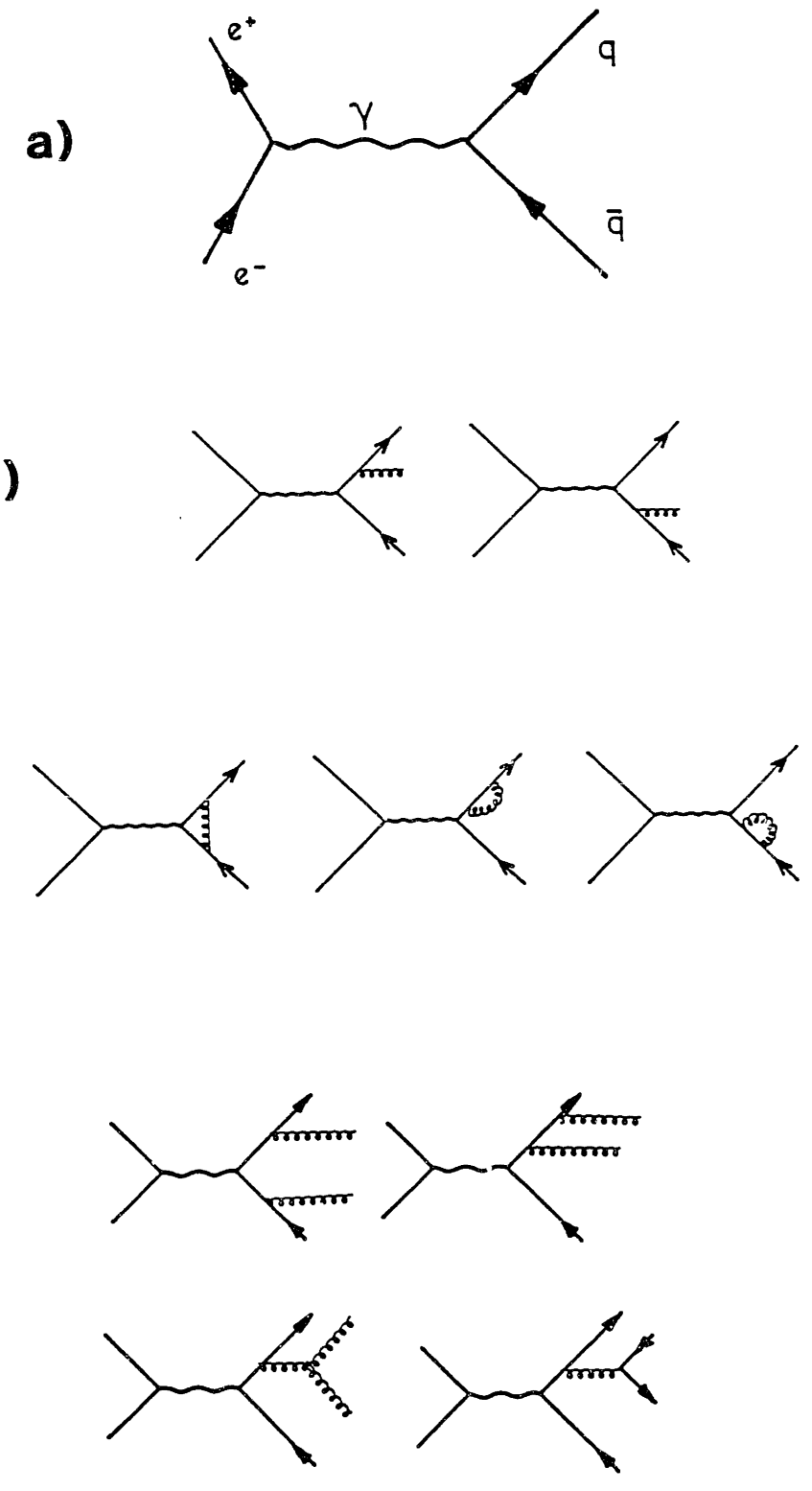

Figure 2.2

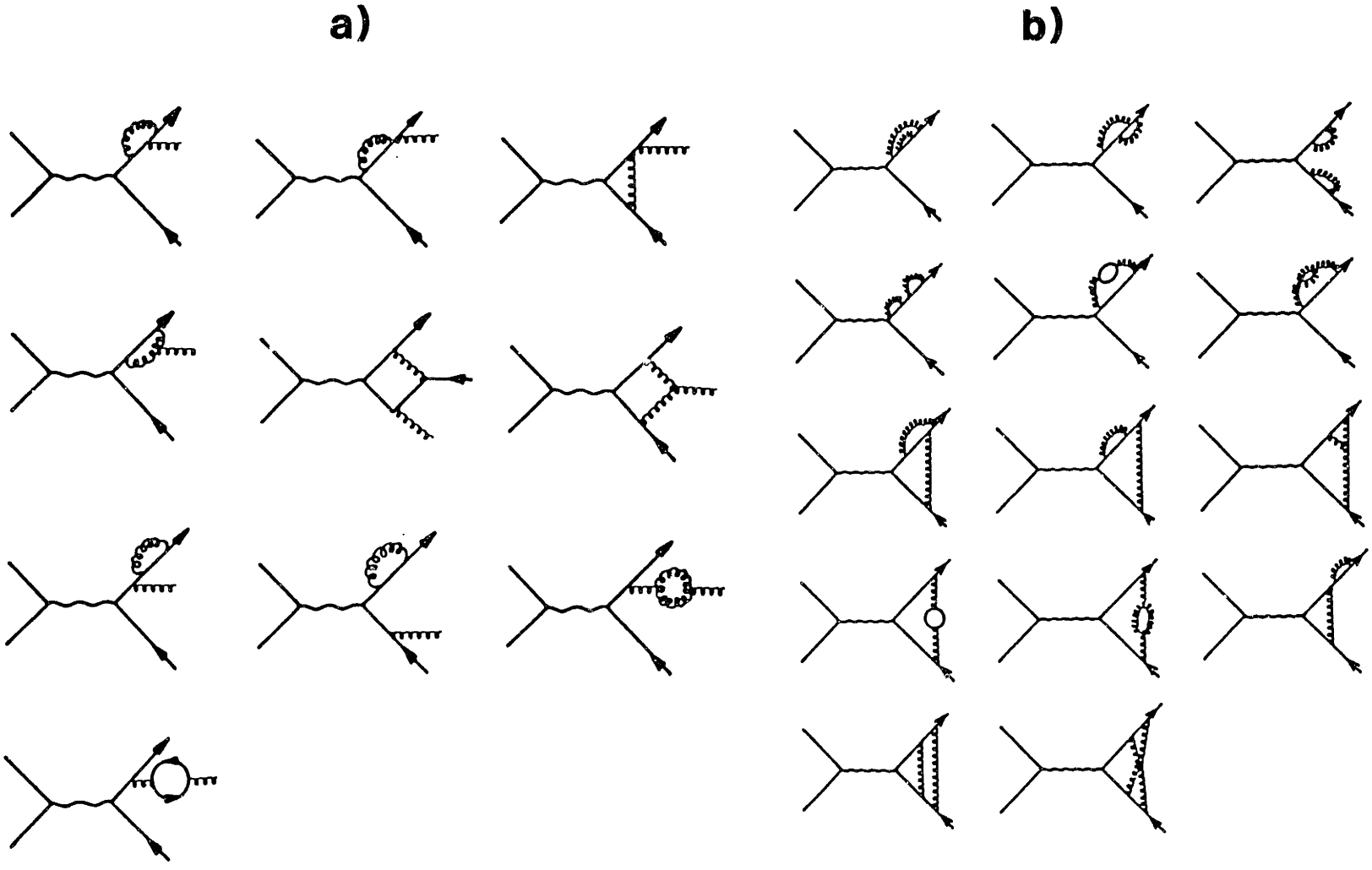

Figure 2.3

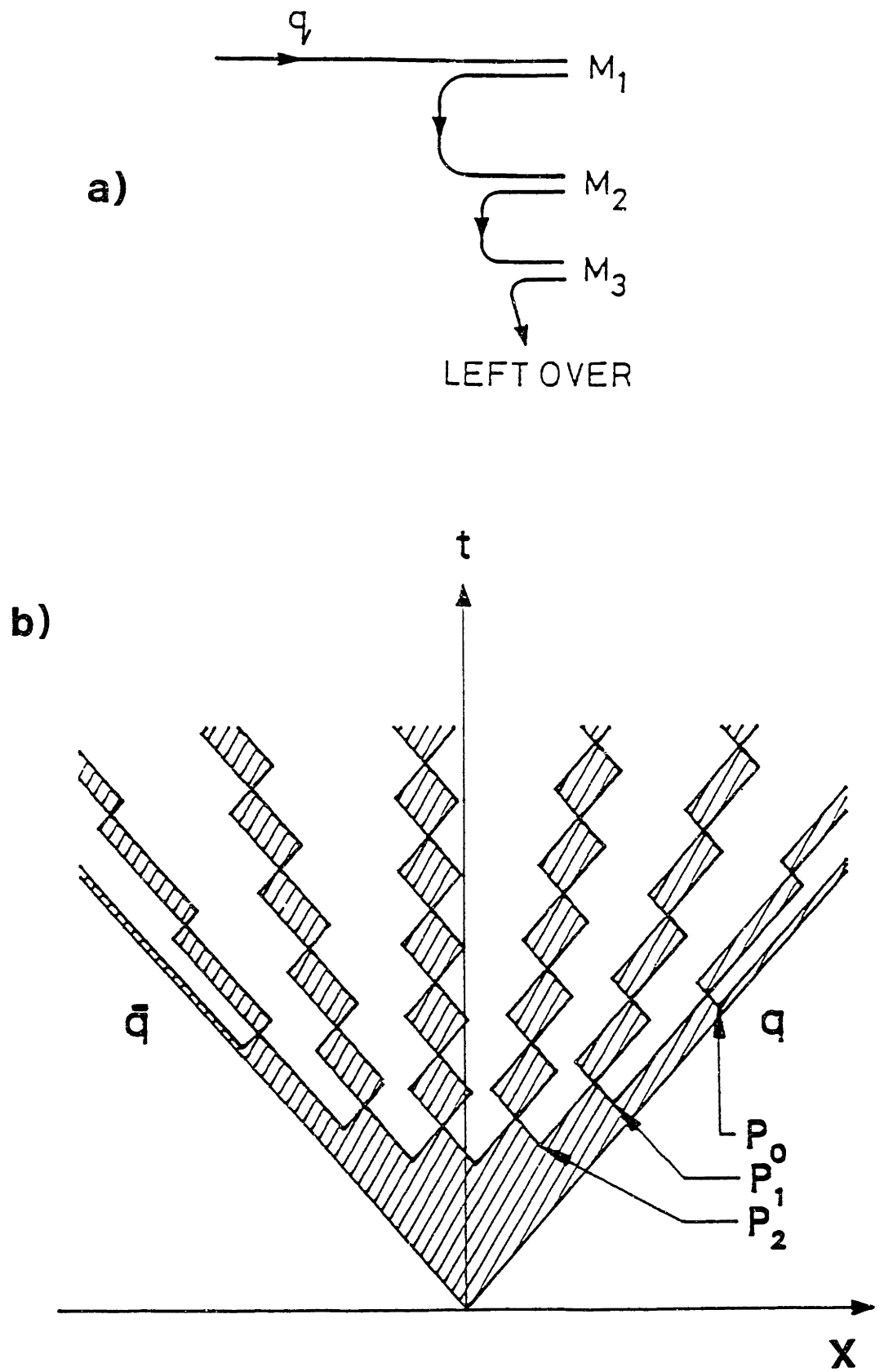

Figure 2.4

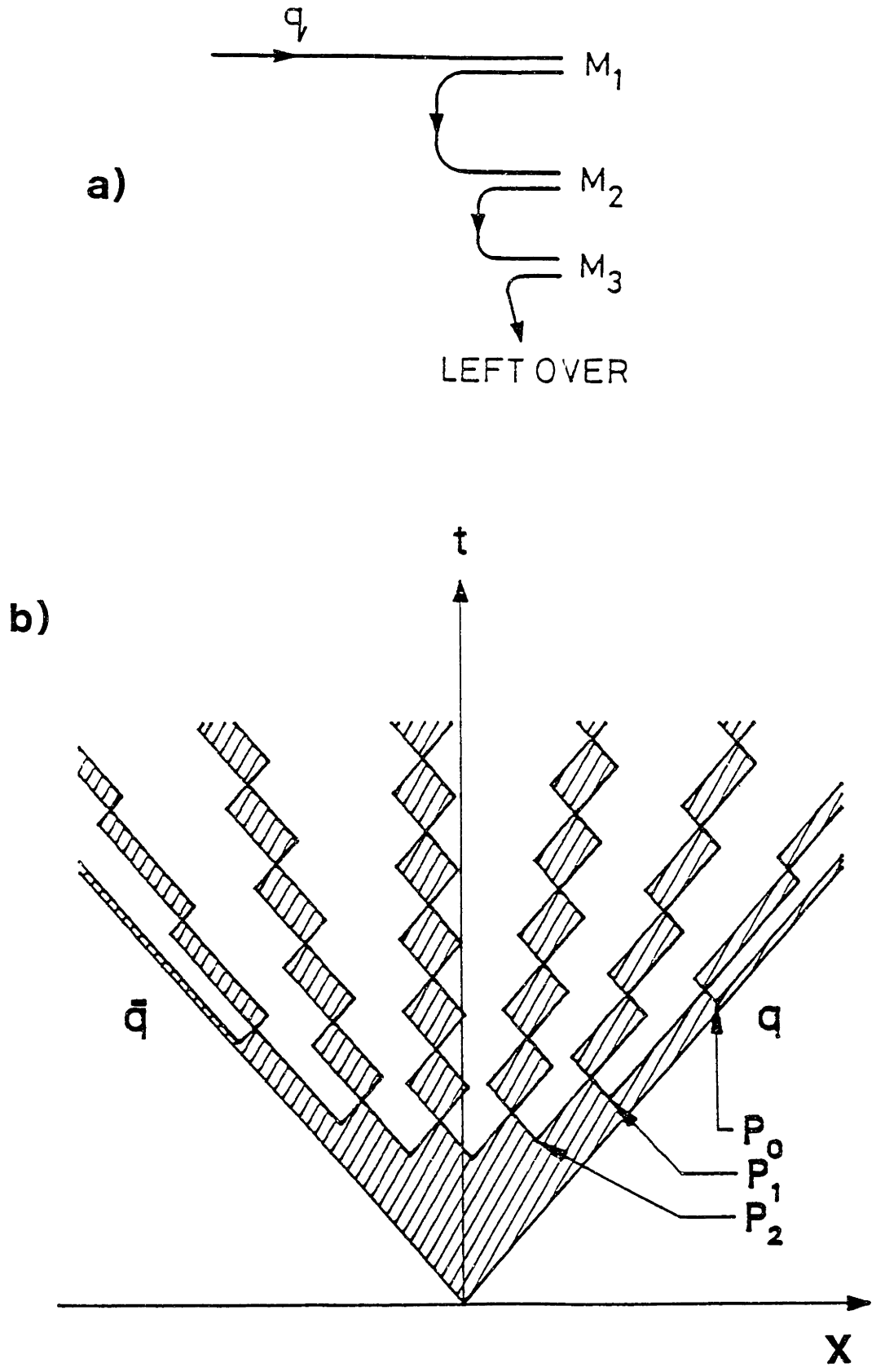

Figure 2.4

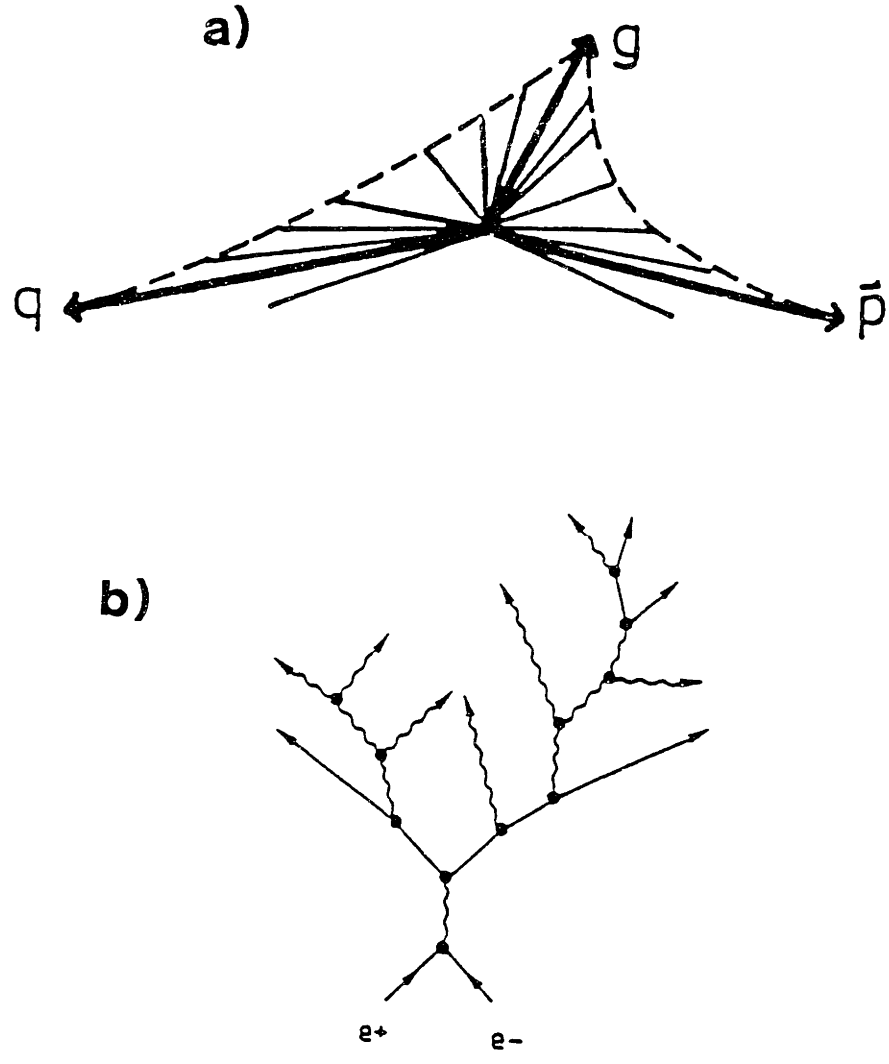

Figure 2.5

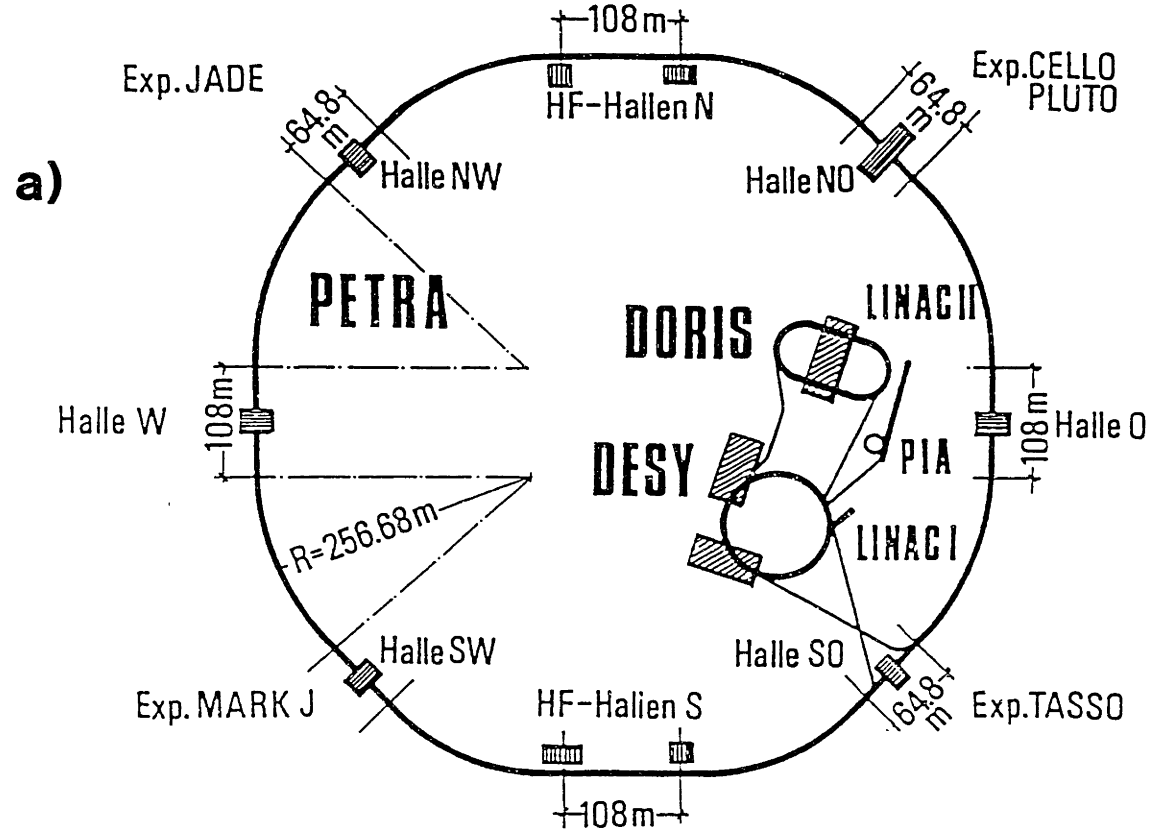
a)
108m
Exp.JADE
HF-Hallen N
Exp.CELLO
PLUTO
64.8m
Halle NW
Halle NO
PETRA
DORIS
LINAC II
Halle W
108m
Halle O
DESY
PIA
R=256.68m
LINAC I
Halle SW
Halle SO
Exp. MARK J
HF-Halien S
Exp.TASSO
108m

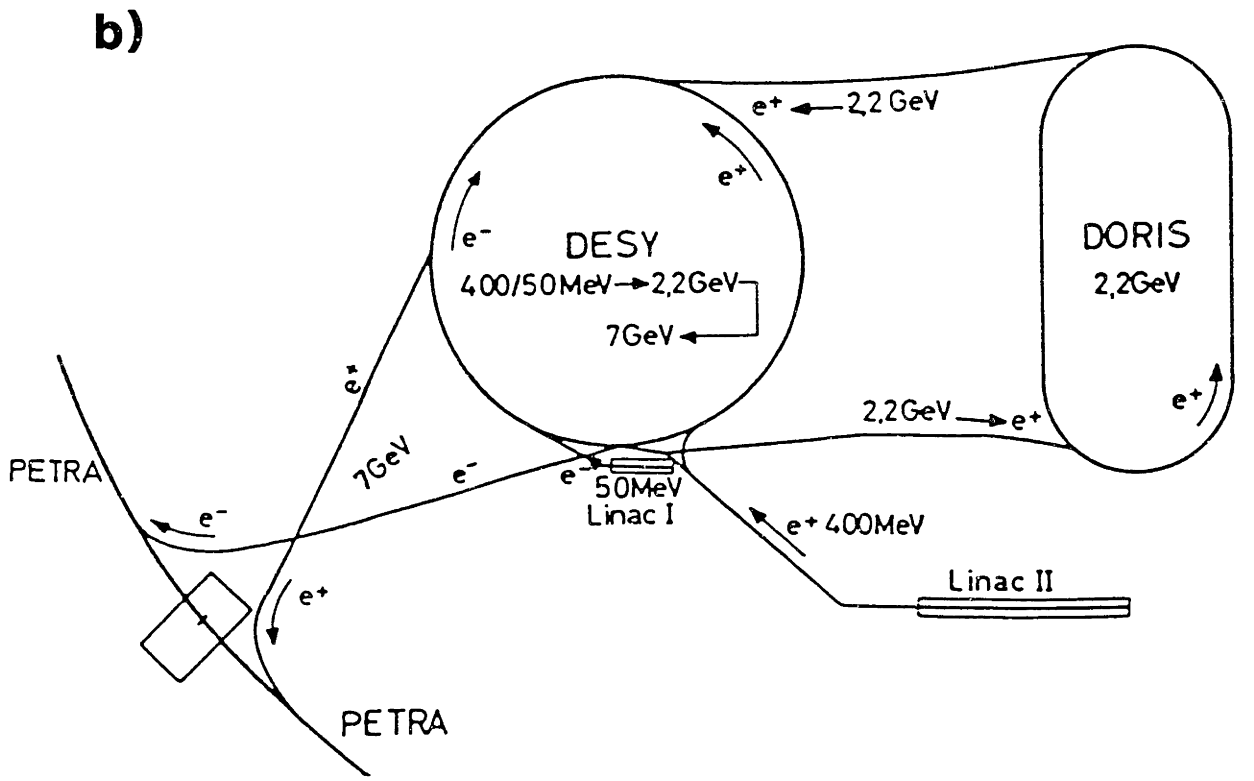
b)
e+ 2,2 GeV
e+
e-
DESY
400/50MeV→2,2GeV
7GeV
DORIS
2,2GeV
e+
2,2GeV → e+
e+
PETRA
7GeV
e-
e-
e-
50MeV
Linac I
e+ 400MeV
e-
Linac II
e+
PETRA

Figure 3.1

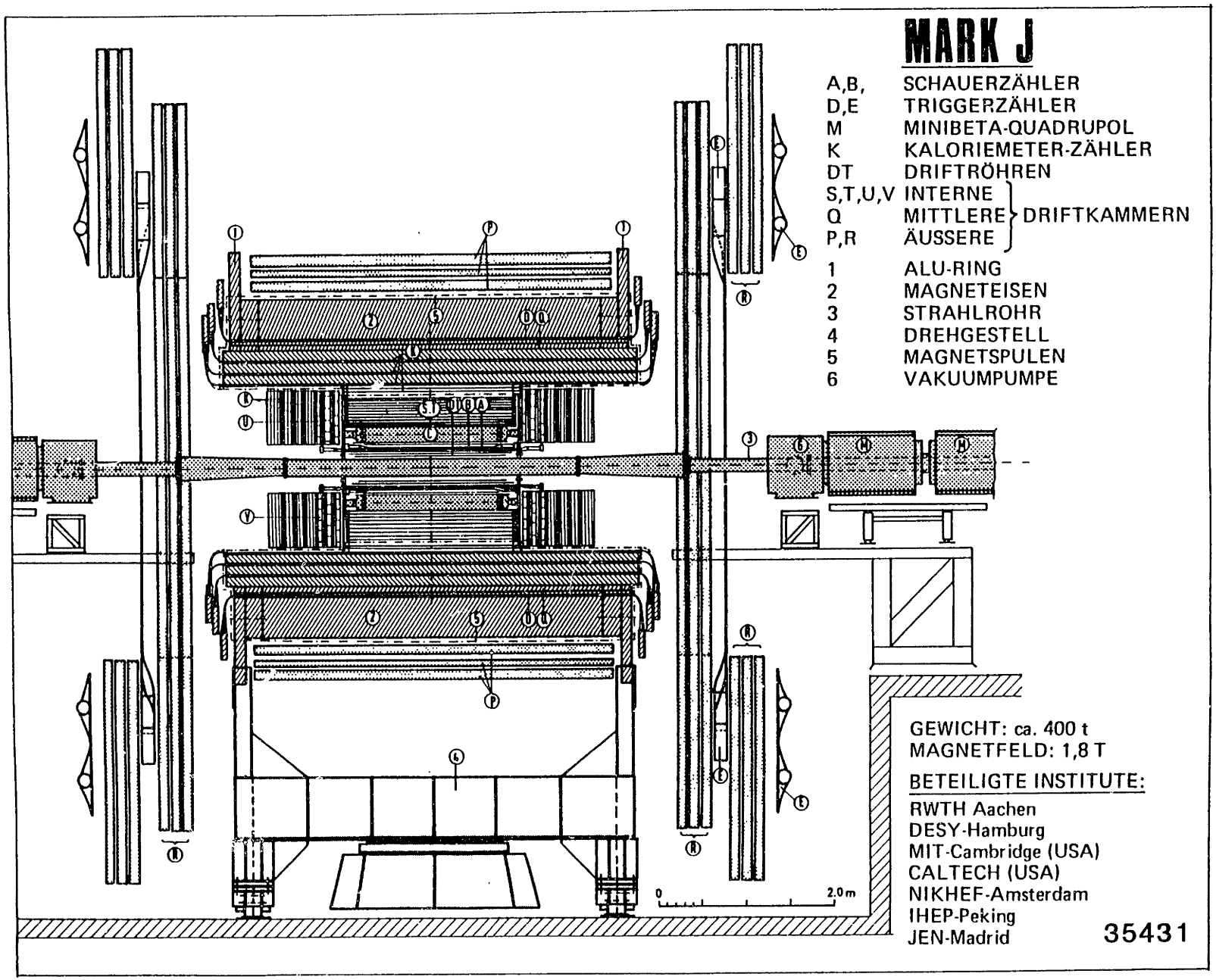
MARK J
A,B, SCHAUERZÄHLER
D,E TRIGGERZÄHLER
M MINIBETA-QUADRUPOL
K KALORIEMETER-ZÄHLER
DT DRIFTRÖHREN
S,T,U,V INTERNE
Q MITTLERE
P,R ÄUSSERE
DRIFTKAMMERN
1 ALU-RING
2 MAGNETEISEN
3 STRAHLROHR
4 DREHGESTELL
5 MAGNETSPULEN
6 VAKUUMPUMPE
GEWICHT: ca. 400 t
MAGNETFELD: 1,8 T
BETEILIGTE INSTITUTE:
RWTH Aachen
DESY-Hamburg
MIT-Cambridge (USA)
CALTECH (USA)
NIKHEF-Amsterdam
IHEP-Peking
JEN-Madrid
0
2.0m
35431

Figure 3.2a

MARK J - DETEKTOR
(Querschnitt)

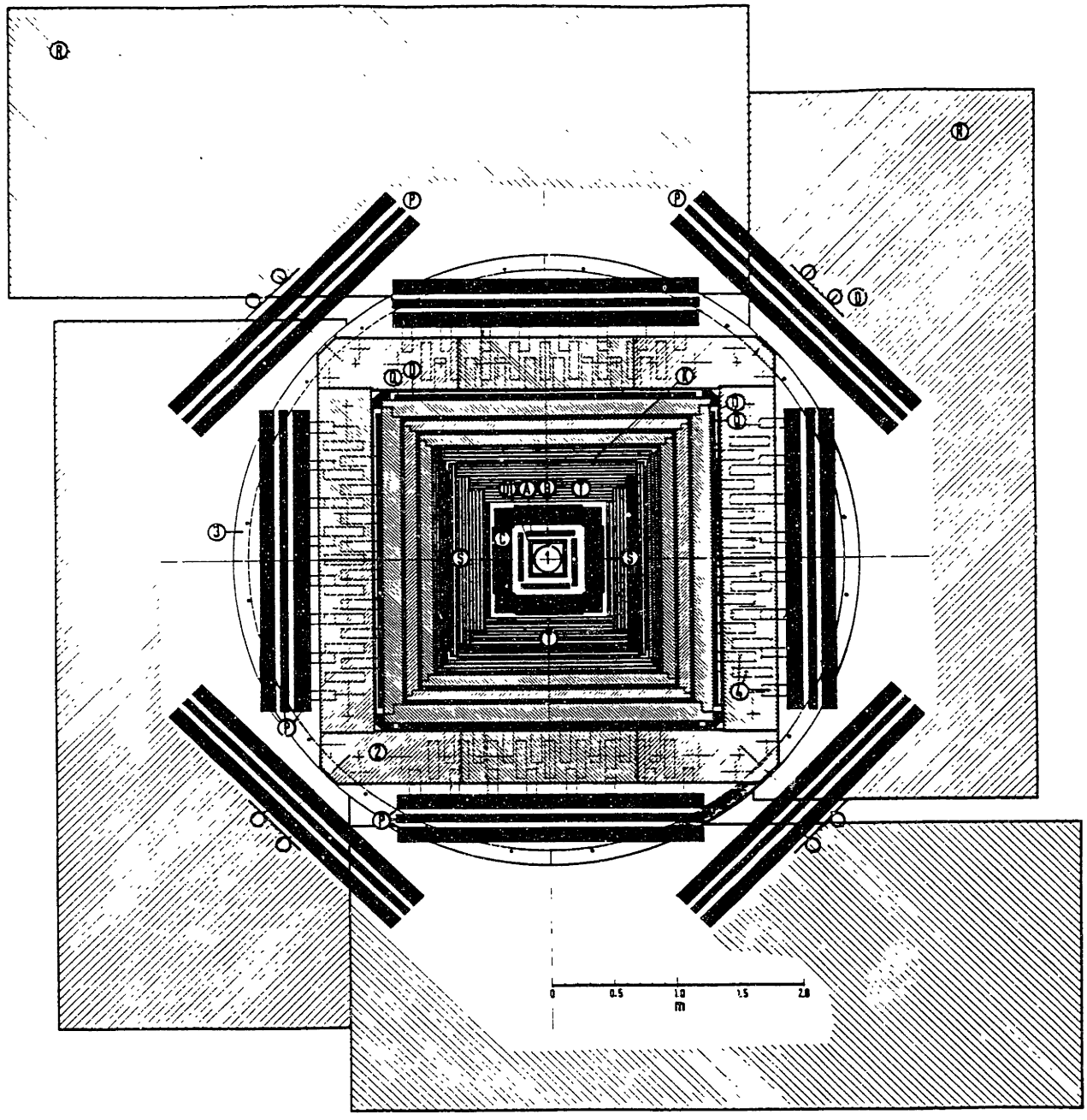

A B C Schauer—Zähler
D Trigger—Zähler
DT Drifttröhren
Q Mittlere Driftkammern
P R Äußere Driftkammern
S T Innere Driftkammern

1 Strahlrohr
2 Eisenjoch
3 Aluminium—Ring
4 Multiplier

Beteiligte Institute

RWTH—Aachen
DESY—Hamburg
MIT—Cambrige
NIKHEF—Amsterdam
HEPI—Peking
JEN—Madrid
CALTECH—Pasadena

Gesamtgewicht: 400 t
Magnetfeld : 1.8 T

36889

Figure 3.2b

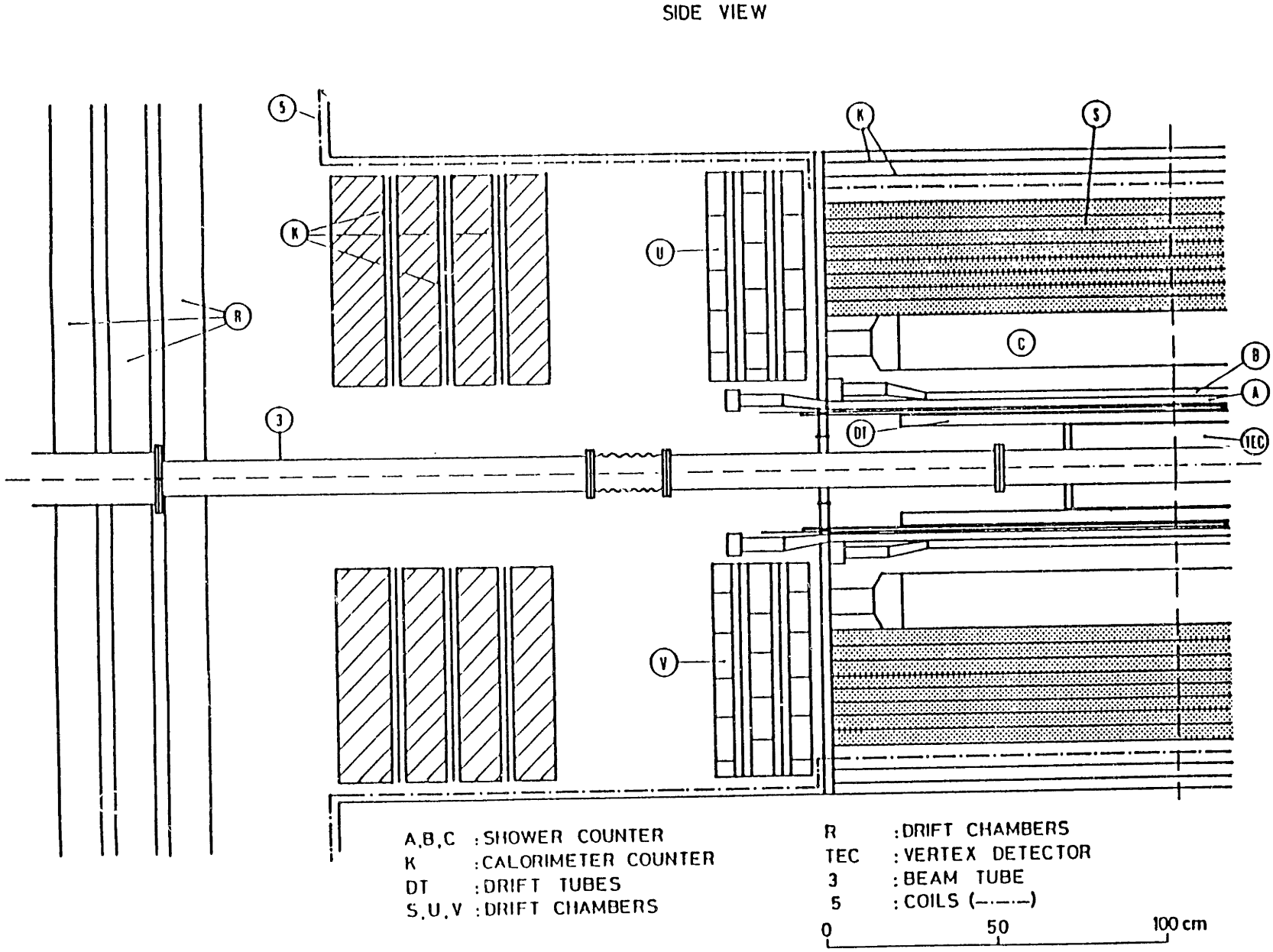
SIDE VIEW
S
K
S
K
U
R
C
B
A
3
DT
TEC
V
A,B,C : SHOWER COUNTER
K : CALORIMETER COUNTER
DT : DRIFT TUBES
S,U,V : DRIFT CHAMBERS
R : DRIFT CHAMBERS
TEC : VERTEX DETECTOR
3 : BEAM TUBE
5 : COILS (—·—·—)
0
50
100 cm

Figure 3.3

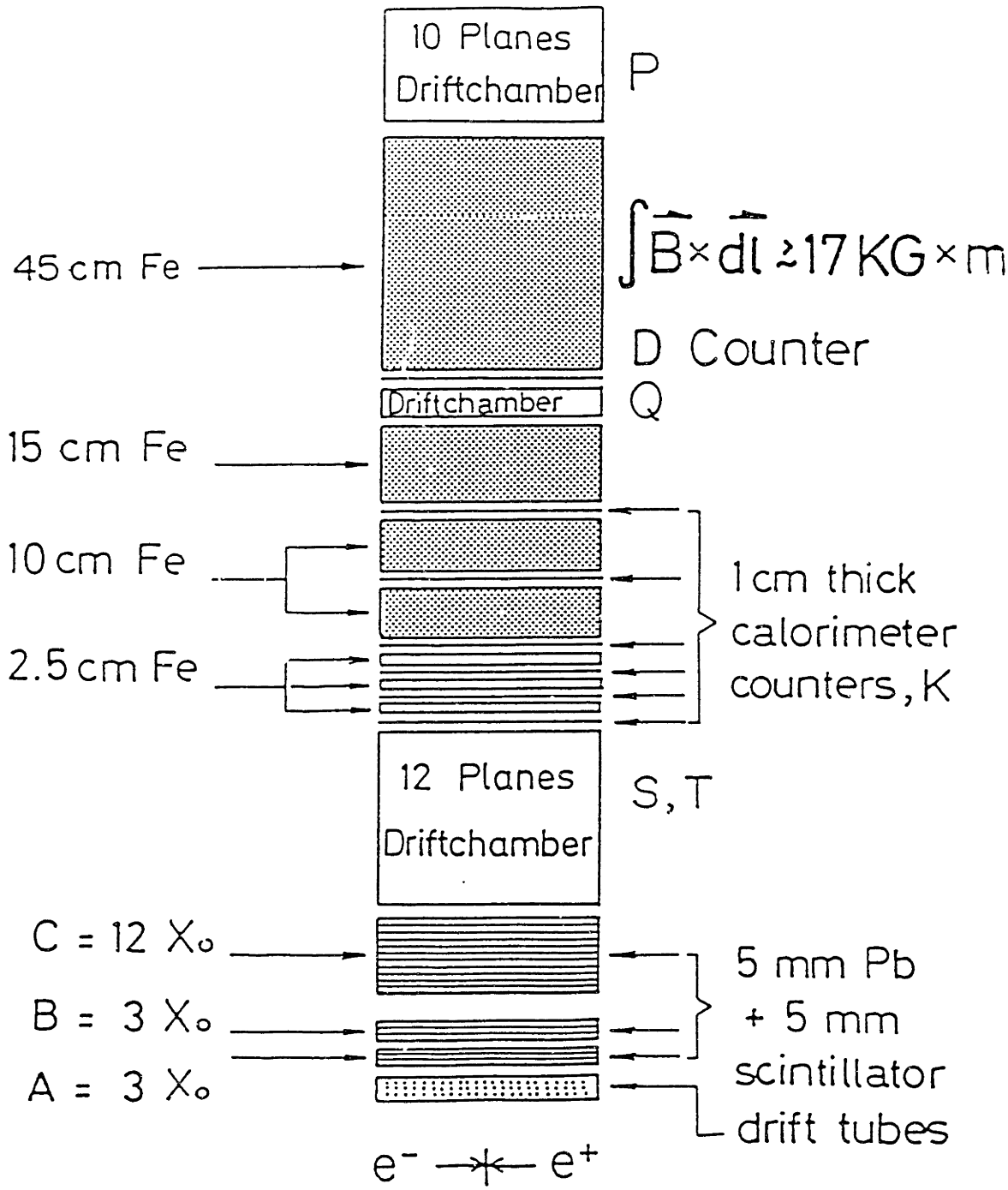
10 Planes
Driftchamber
P
45 cm Fe
$\int \vec{B} \times d\vec{l} \gtrsim 17\,KG \times m$
D Counter
Driftchamber
Q
15 cm Fe
10 cm Fe
2.5 cm Fe
1 cm thick
calorimeter
counters, K
12 Planes
Driftchamber
S, T
C = 12 X_o
B = 3 X_o
A = 3 X_o
5 mm Pb
+ 5 mm
scintillator
drift tubes
$e^- \rightarrow \leftarrow e^+$

Figure 3.4

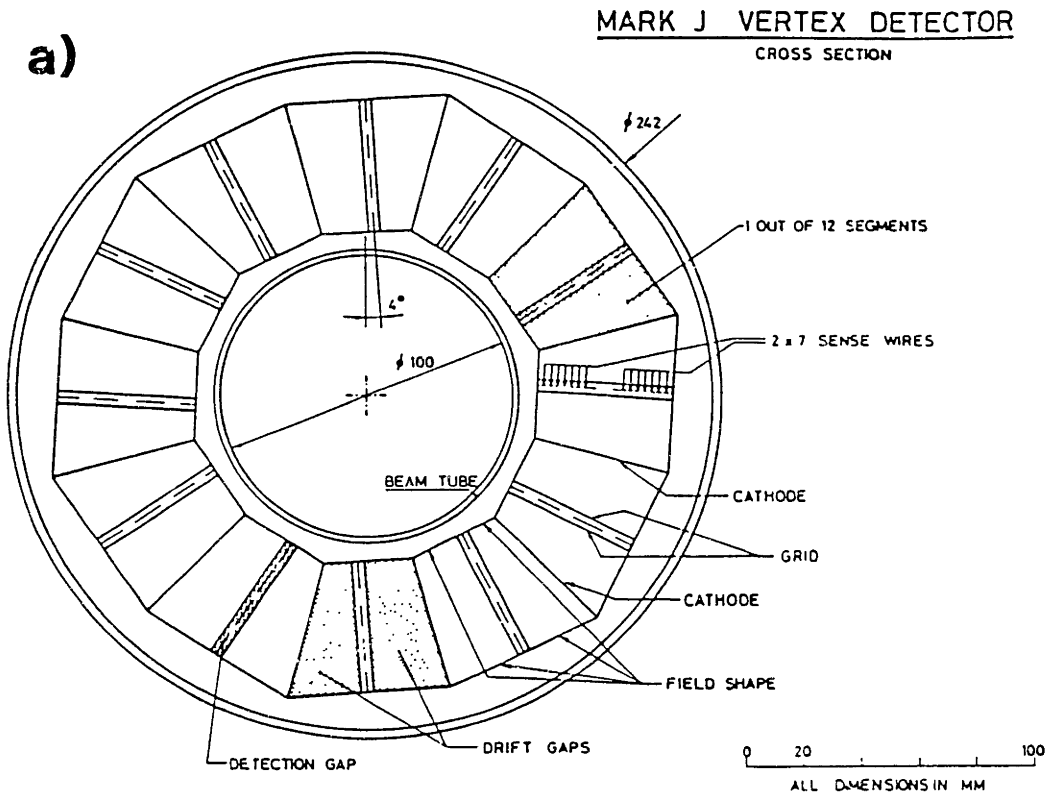
a)
MARK J VERTEX DETECTOR
CROSS SECTION
ϕ242
1 OUT OF 12 SEGMENTS
2 x 7 SENSE WIRES
4°
ϕ100
BEAM TUBE
CATHODE
GRID
CATHODE
FIELD SHAPE
DRIFT GAPS
DETECTION GAP
0 20 100
ALL DIMENSIONS IN MM

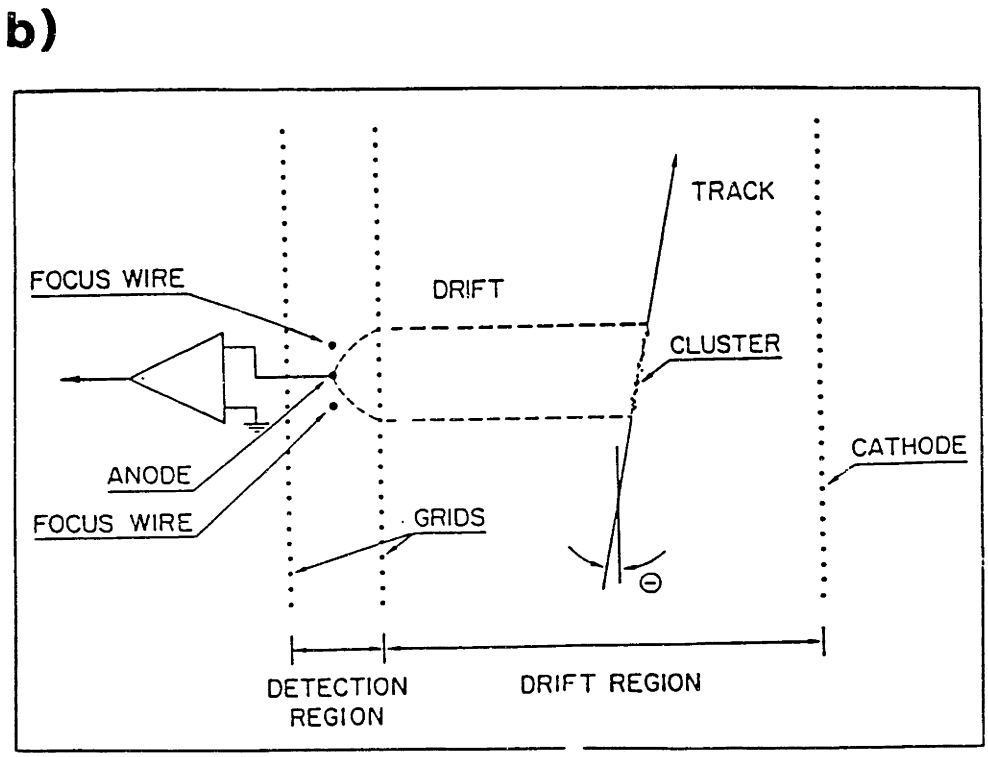
b)
TRACK
FOCUS WIRE
DRIFT
CLUSTER
CATHODE
ANODE
FOCUS WIRE
GRIDS
DETECTION REGION
DRIFT REGION

Figure 3.5

a)

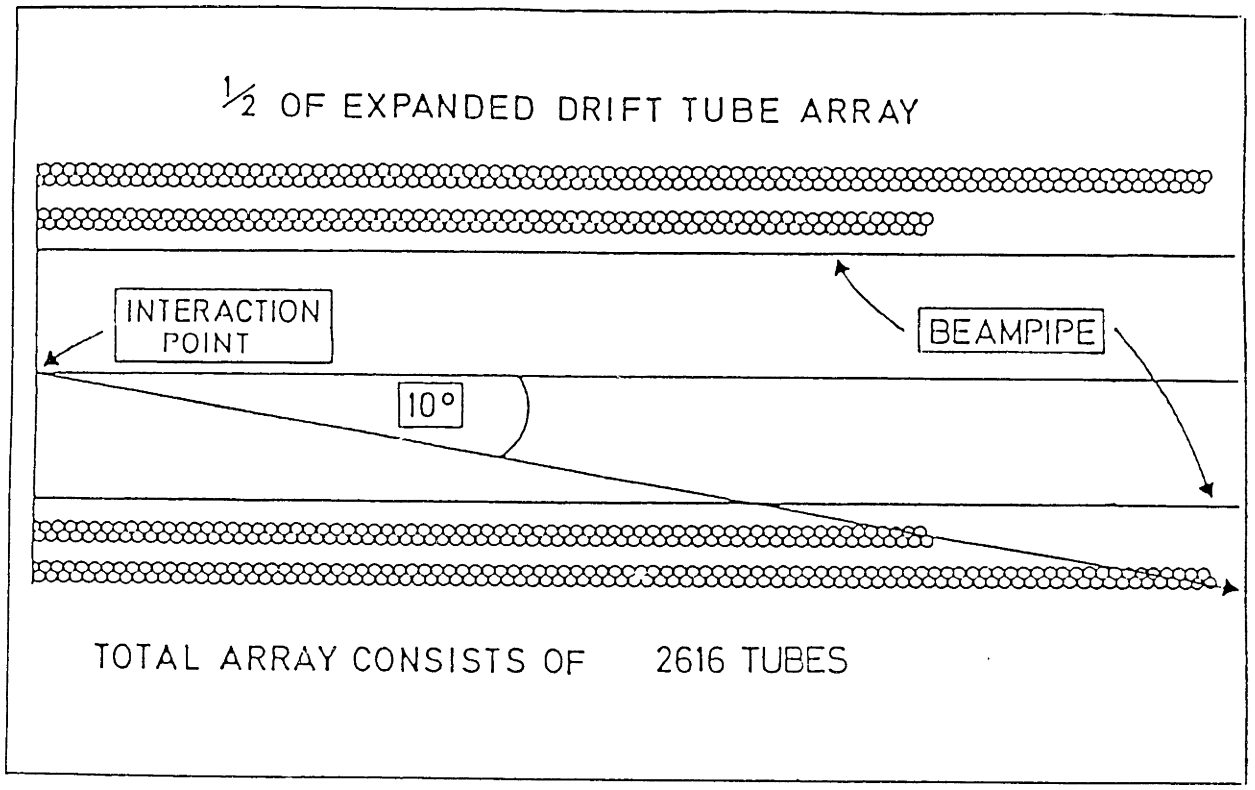
½ OF EXPANDED DRIFT TUBE ARRAY
INTERACTION POINT
BEAMPIPE
10°
TOTAL ARRAY CONSISTS OF 2616 TUBES

b)

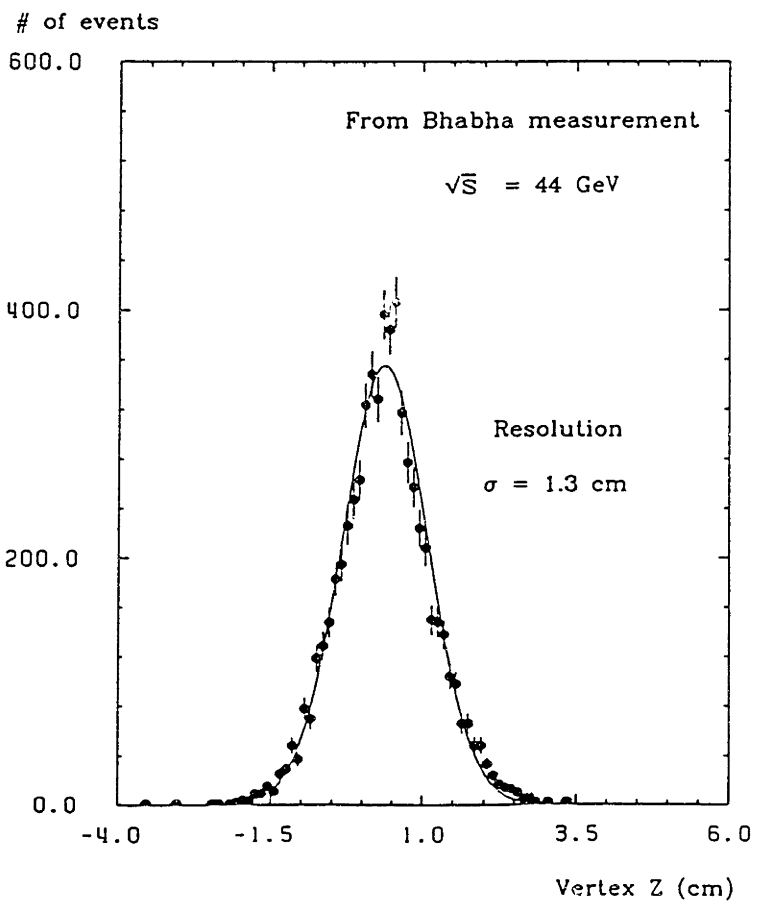
# of events
600.0
400.0
200.0
0.0
From Bhabha measurement
√s = 44 GeV
Resolution
σ = 1.3 cm
-4.0
-1.5
1.0
3.5
6.0
Vertex Z (cm)

Figure 3.6

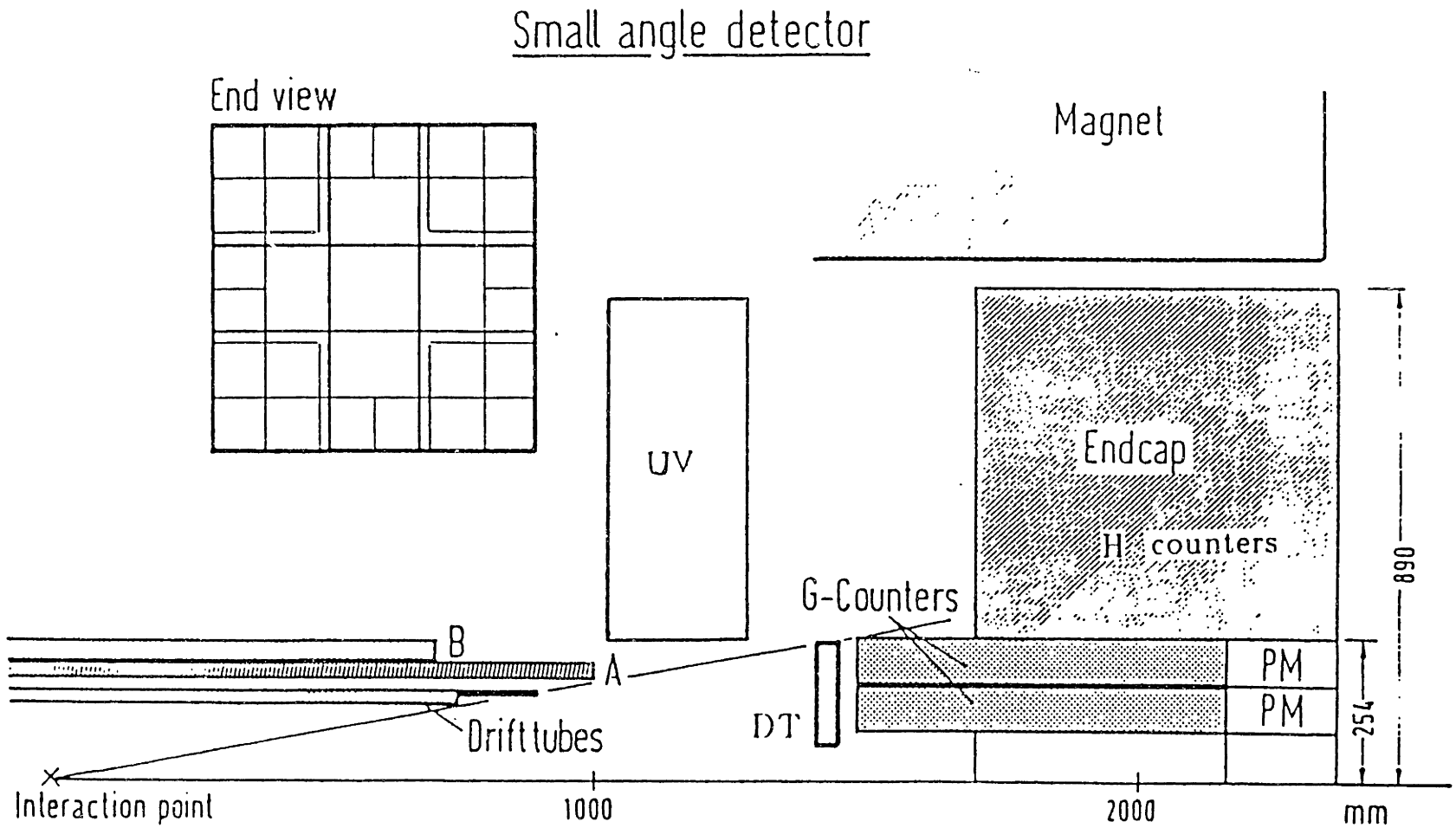
Small angle detector
End view
Magnet
UV
Endcap
H counters
G-Counters
B
A
PM
PM
DT
Drift tubes
254
890
Interaction point
1000
2000
mm

Figure 3.7

a)

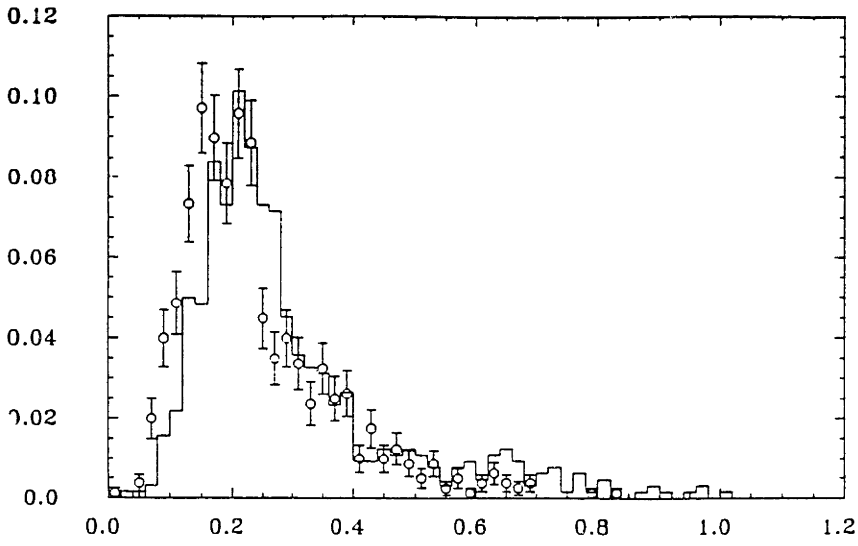

E(A)/ETOT DEC. 86

b)

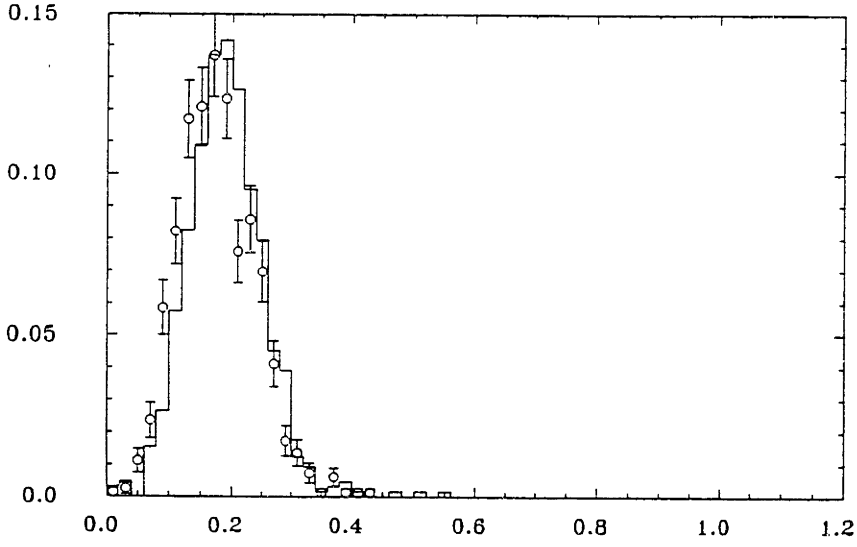

E(B)/ETOT DEC. 86

c)

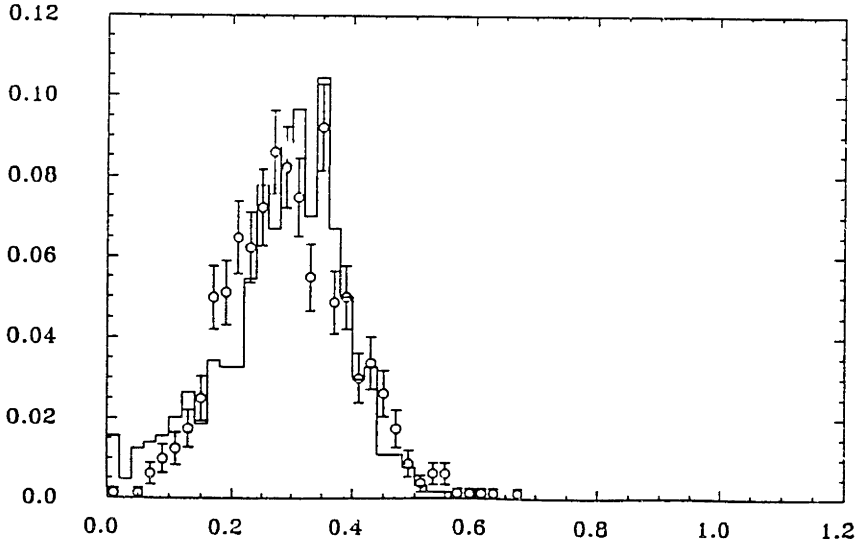

E(C)/ETOT DEC. 86

Figure 3.8

a)

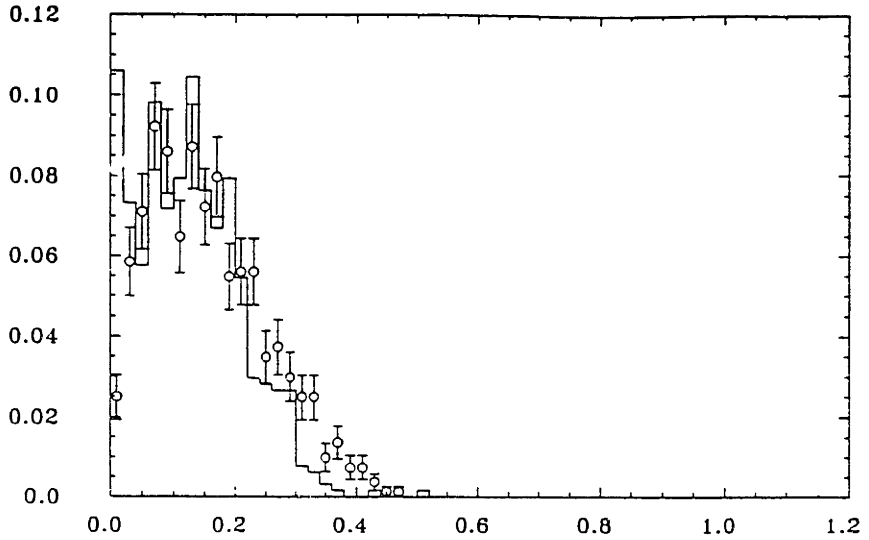

E(K12)/ETOT DEC. 86

b)

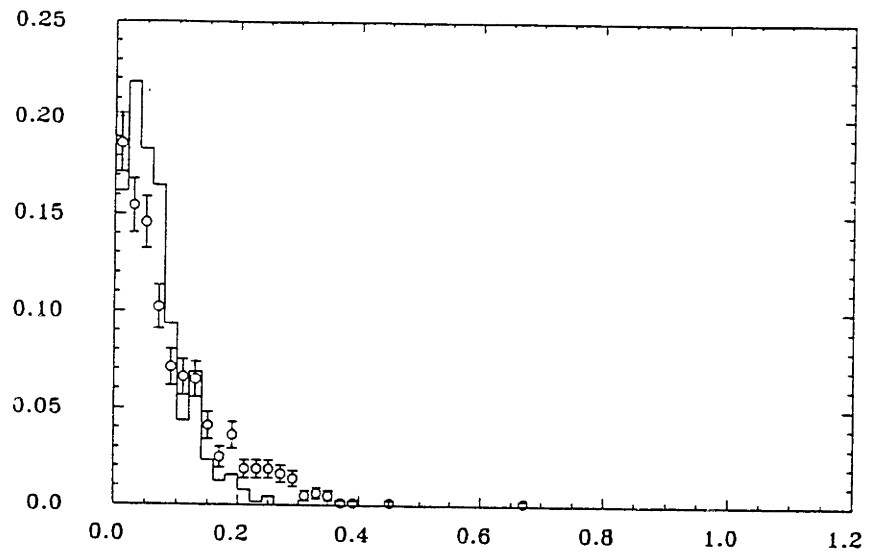

E(K3)/ETOT DEC. 86

c)

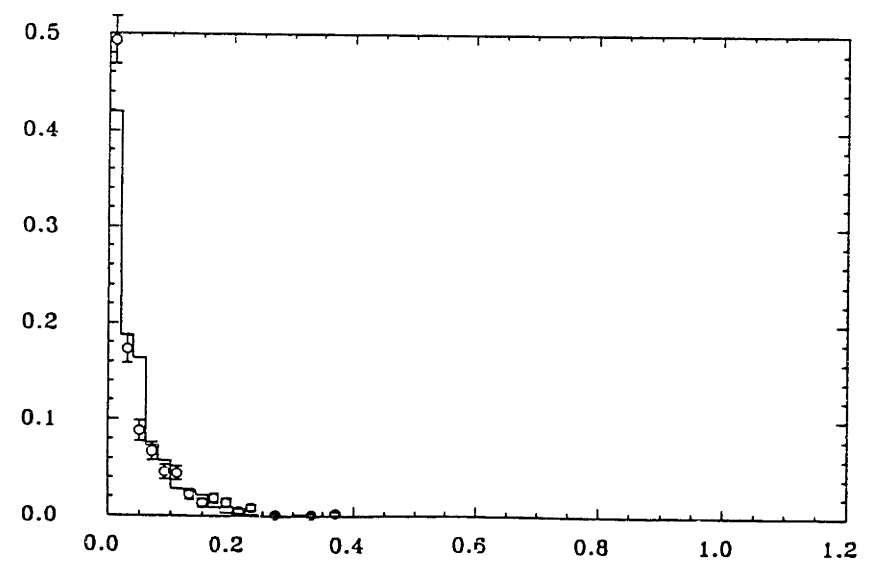

E(K4)/ETOT DEC. 86

Figure 3.9

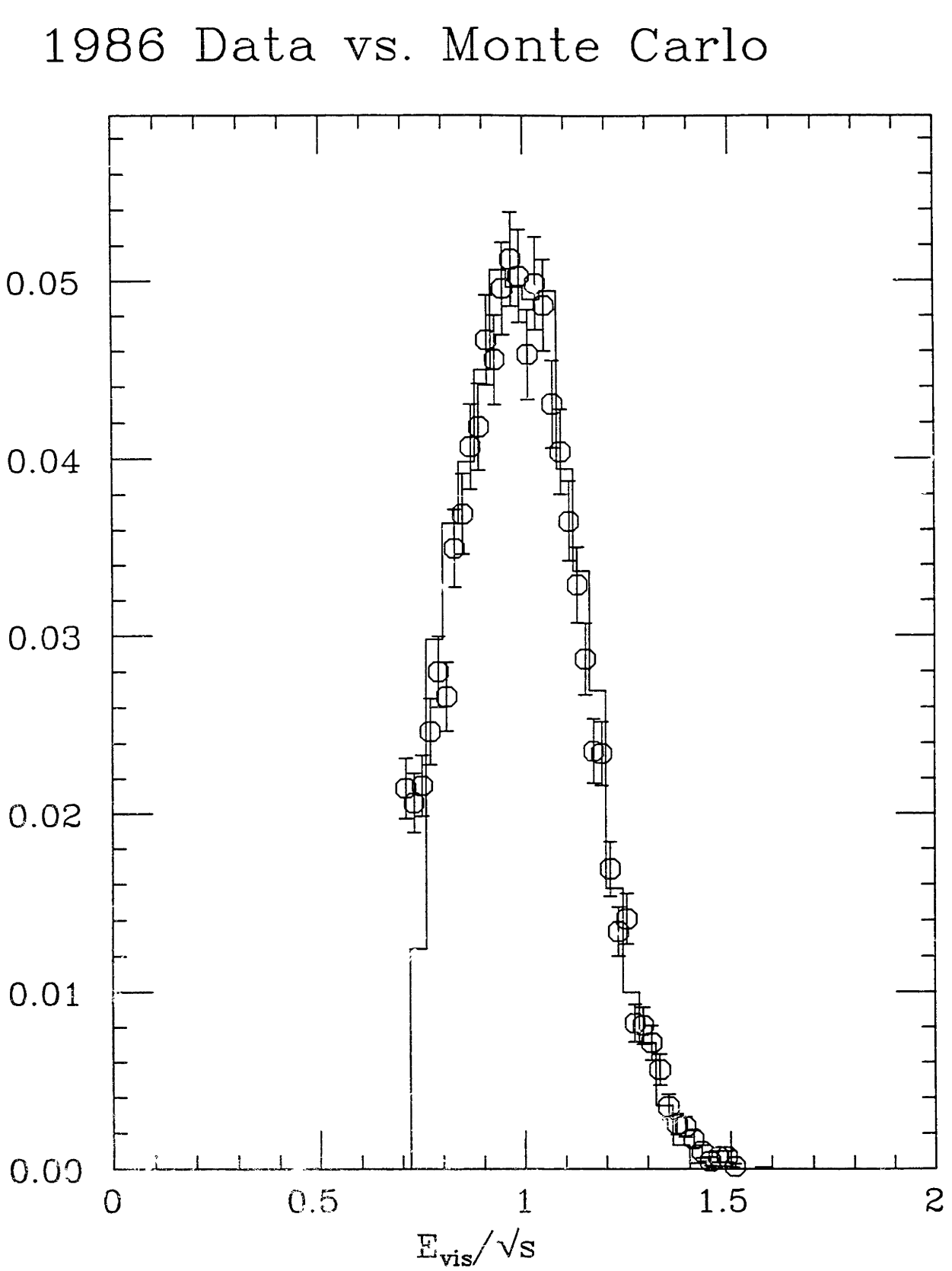
1986 Data vs. Monte Carlo
0.05
0.04
0.03
0.02
0.01
0.00
0
0.5
1
1.5
2
$E_{vis}/\sqrt{s}$

Figure 4.1

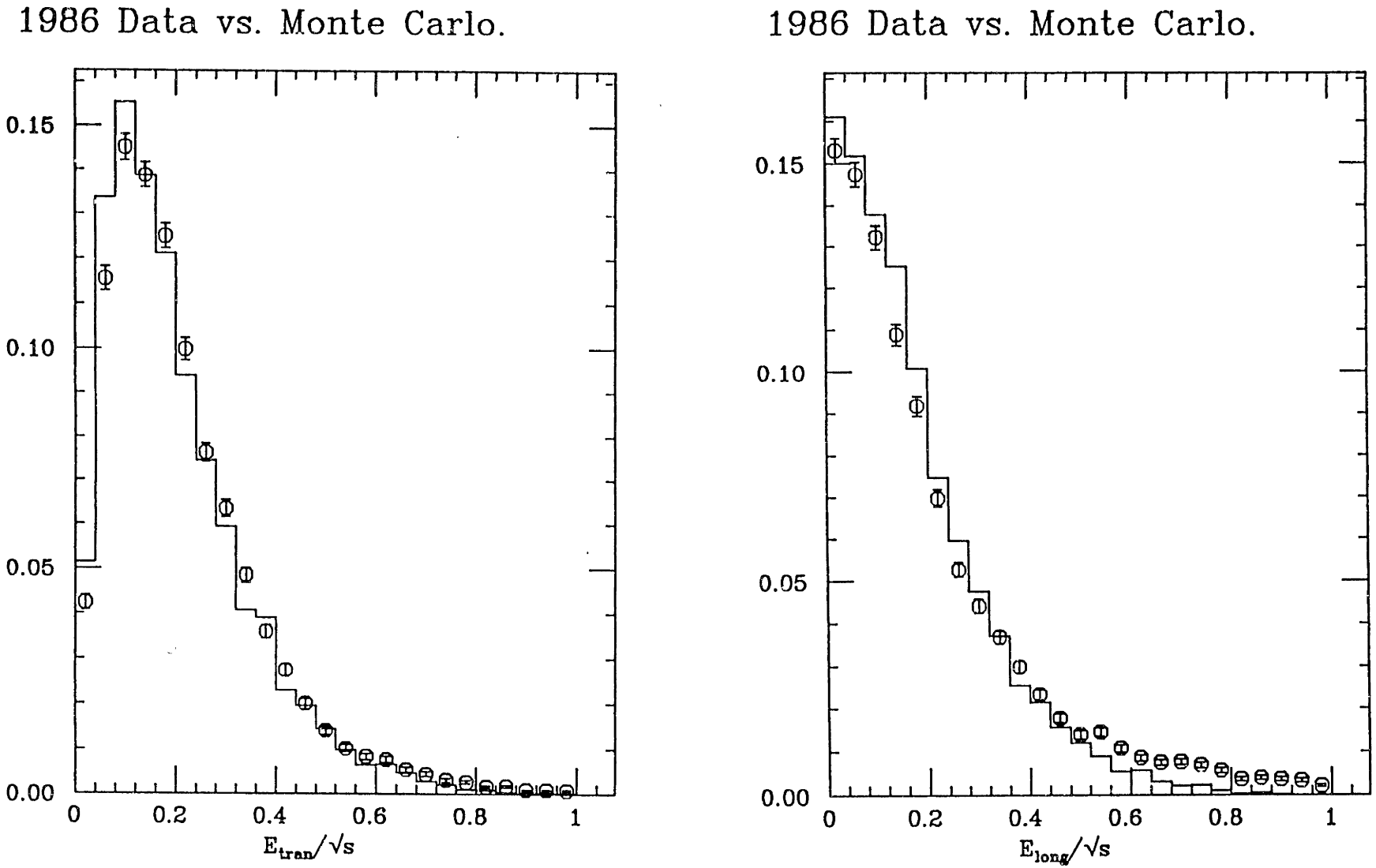
1986 Data vs. Monte Carlo.
0.15
0.10
0.05
0.00
0
0.2
0.4
0.6
0.8
1
$E_{tran}/\sqrt{s}$
1986 Data vs. Monte Carlo.
0.15
0.10
0.05
0.00
0
0.2
0.4
0.6
0.8
1
$E_{long}/\sqrt{s}$

Figure 4.2

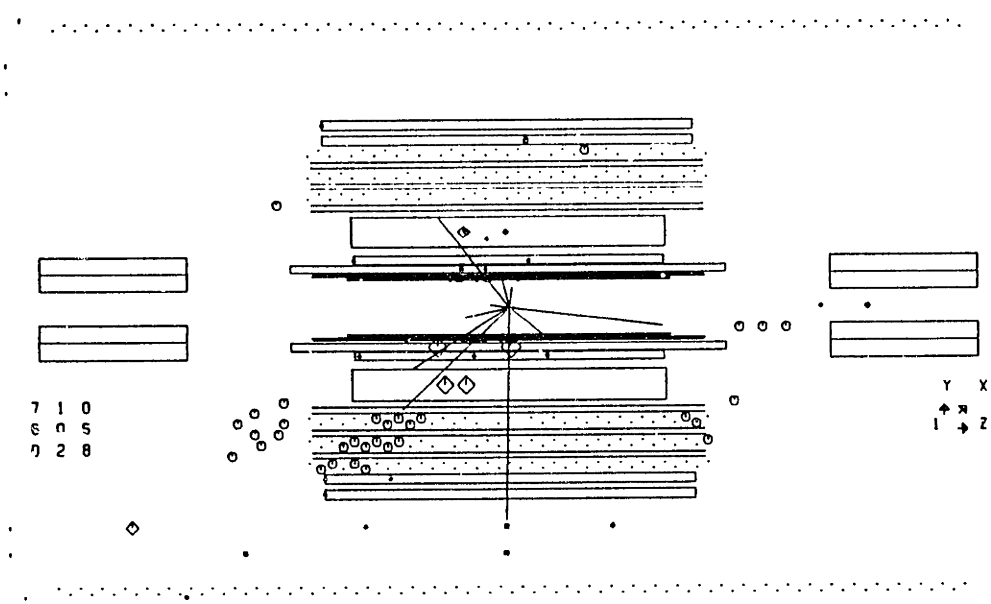

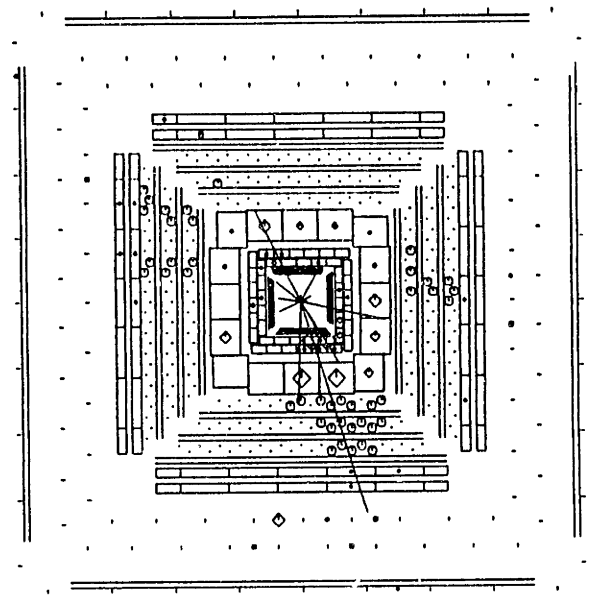

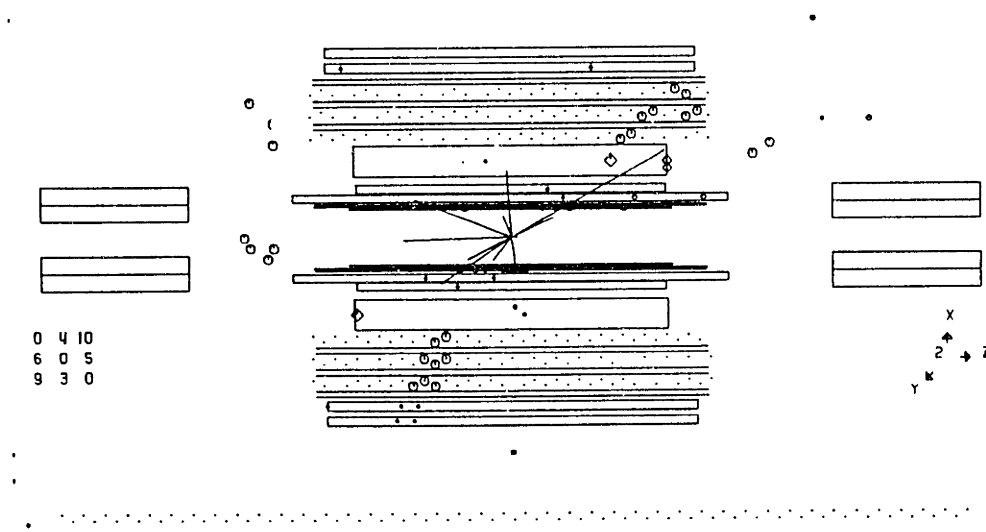

RUN11937 EVENT 2017 ECMS 35.00 86/ 6/22 20.42.40
CTRS TDC 158 ADC 205 ABC25130 K 5876

REG	L	A	B	C	K12	K3	K4	D	SUM	ER	5	6	SUM
1	0	867	150	3466	78	0	0	0	4561	E	0	0	0
2	0	6313	940	4294	973	2765	235	18	415520	G	0	0	0
3	0	385	55	2349	1206	74	0	195	4069	DP	0	0	0
4	0	1792	166	4353	238	307	0	0	6856	H	1171	0	1171
0	0	9357	131	114462	2495	3146	235	37	932177	SUM	1171	0	1171

WIRES 196 165 (NB/B) TUBES 171 170

REG	ST		Q		P		CP		UV		R		FR	BA
1	1	1	0	0	0	0	0	0	2	4	0	0	0	41
2	20	18	0	0	0	0	0	0	7	9	17	48	0	35
3	13	8	0	0	1	0	0	0	0	0	0	0	0	46
4	8	8	0	0	0	0	0	0	0	0	0	0	0	48

NJ 12 ETOT 31.01 EKD 5.88 PXYZ 3.87 -8.69 -4.64
EMIN= 0.10 ESCALE= 10.0

J	EJ	EKD	THE	PHI	NC
1	6.89	0.82	91.1	287.6	5
2	5.30	0.48	31.6	347.6	9
3	4.47	2.18	135.1	268.2	5
4	3.79	0.45	122.9	116.6	7
5	3.62	1.03	141.6	302.2	6
6	1.73	0.0	44.5	300.1	2
7	1.49	0.0	150.0	205.0	1
8	1.32	0.0	100.5	60.0	3
9	1.01	0.12	84.8	140.9	5

THR 0.629
OBL 0.353
MIN 0.240

Figure 4.3

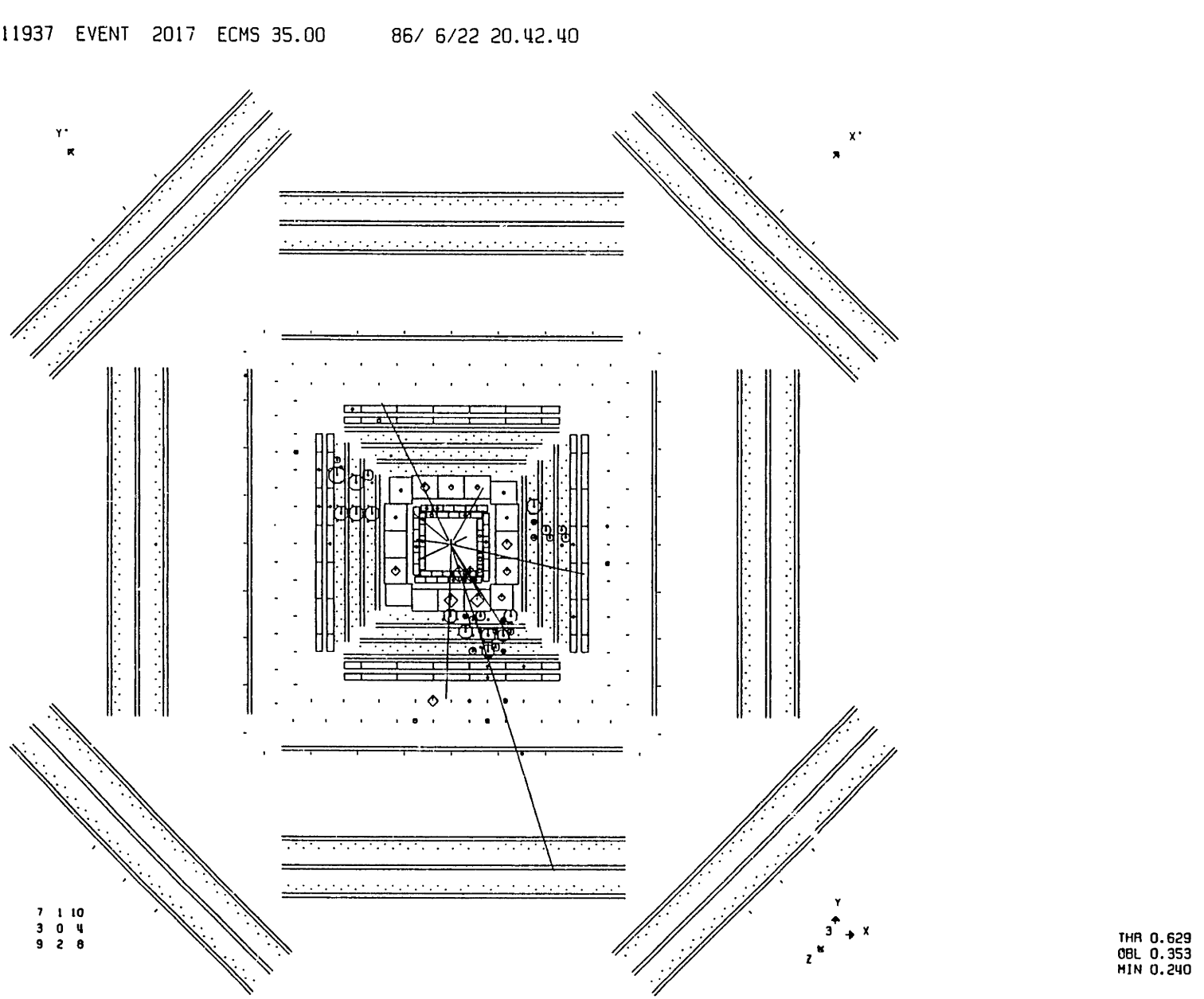
RUN 1937 EVENT 2017 ECMS 35.00 86/ 6/22 20.42.40
Y
X
7 1 10
3 0 4
9 2 8
Y
3
X
Z
THR 0.629
OBL 0.353
MIN 0.240

Figure 4.4

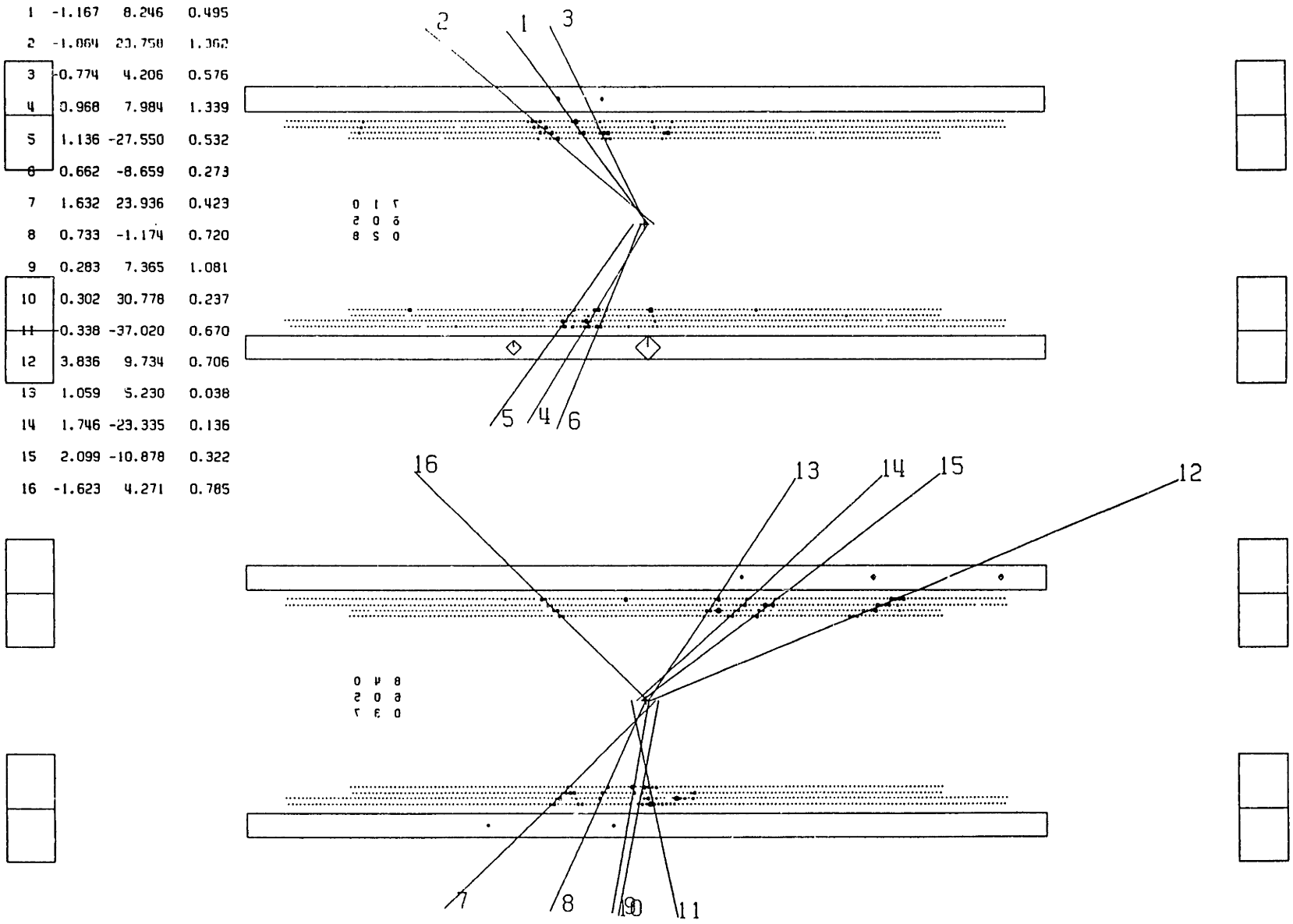
RUN11937 EVENT 2017 ECMS 35.00 86/ 6/22 20.42.40
1 -1.167 8.246 0.495
2 -1.064 23.750 1.362
3 -0.774 4.206 0.576
4 0.968 7.984 1.339
5 1.136 -27.550 0.532
6 0.662 -8.659 0.273
7 1.632 23.936 0.423
8 0.733 -1.174 0.720
9 0.283 7.365 1.081
10 0.302 30.778 0.237
11 -0.338 -37.020 0.670
12 3.836 9.734 0.706
13 1.059 5.230 0.038
14 1.746 -23.335 0.136
15 2.099 -10.878 0.322
16 -1.623 4.271 0.785
1
2
3
4
5
6
7
8
9
10
11
12
13
14
15
16

Figure 4.5

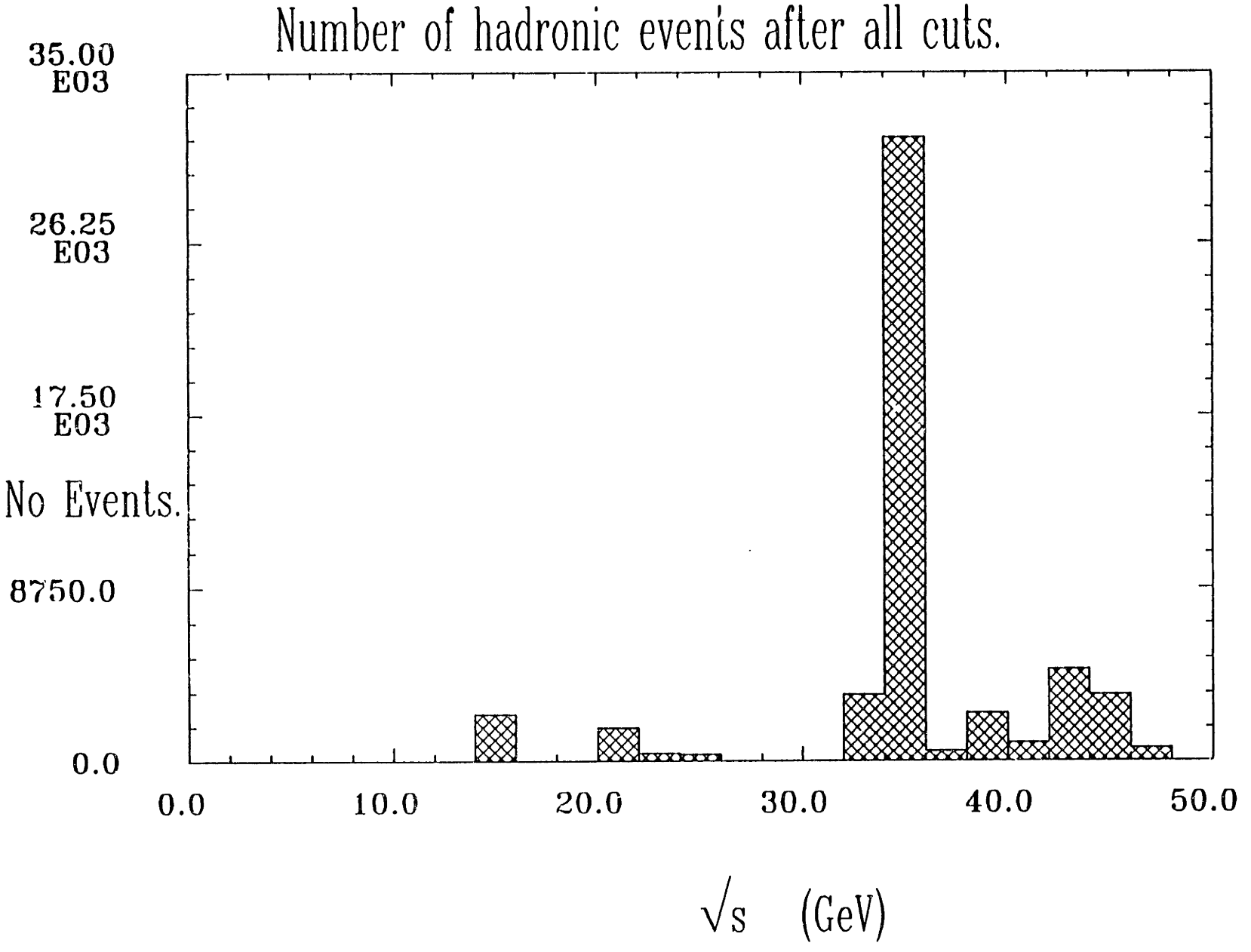
Number of hadronic events after all cuts.
35.00
E03
26.25
E03
17.50
E03
No Events.
8750.0
0.0
0.0
10.0
20.0
30.0
40.0
50.0
√s (GeV)

Figure 4.6

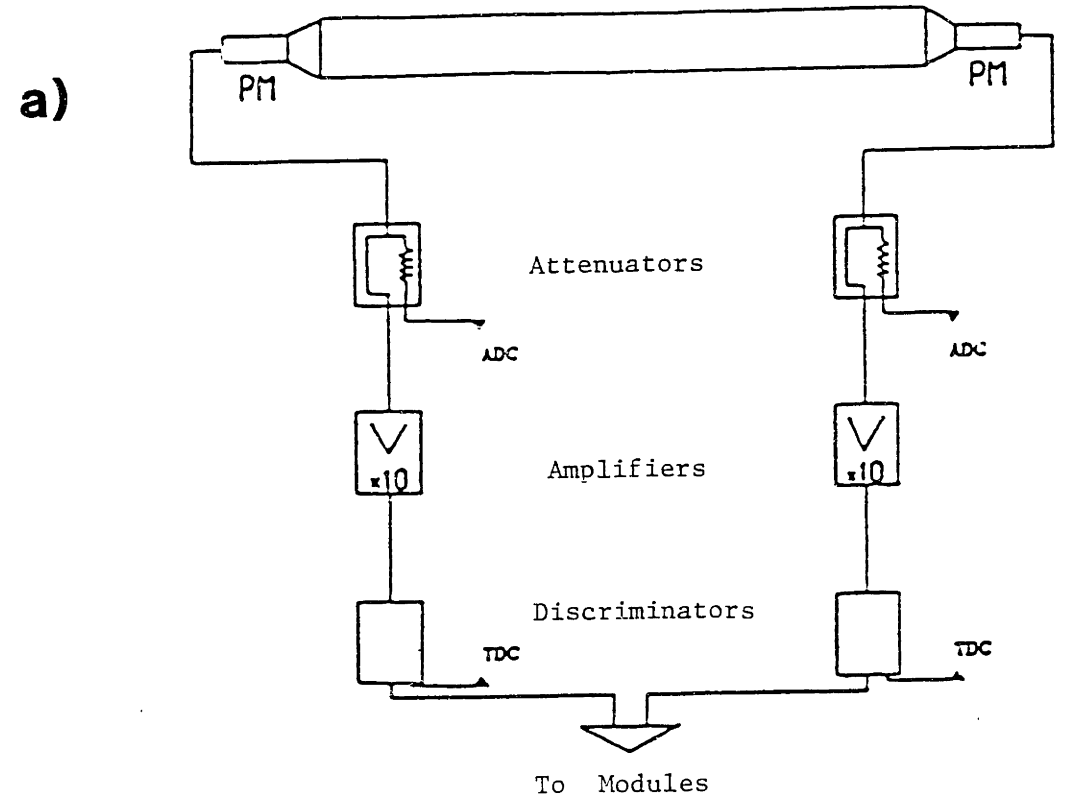
a)
PM
PM
Attenuators
ADC
ADC
x10
x10
Amplifiers
Discriminators
TDC
TDC
To Modules

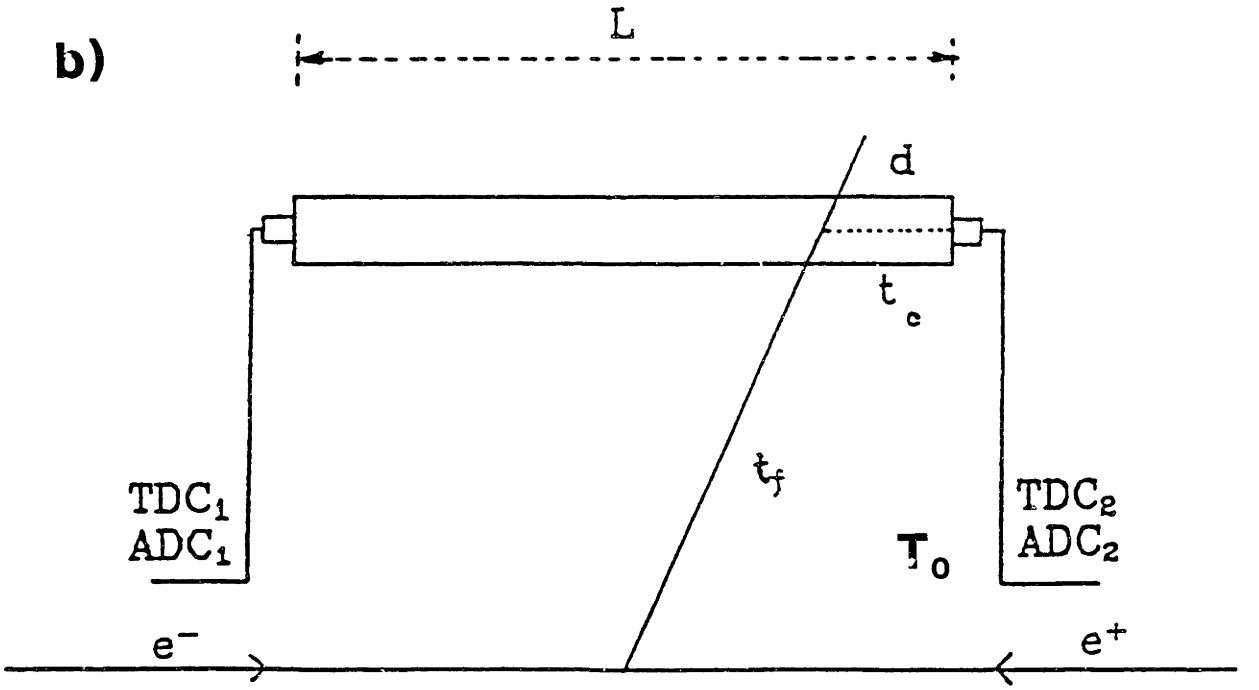
b)
L
d
t_c
t_f
T_0
TDC_1
ADC_1
TDC_2
ADC_2
e^-
e^+

Figure 4.7

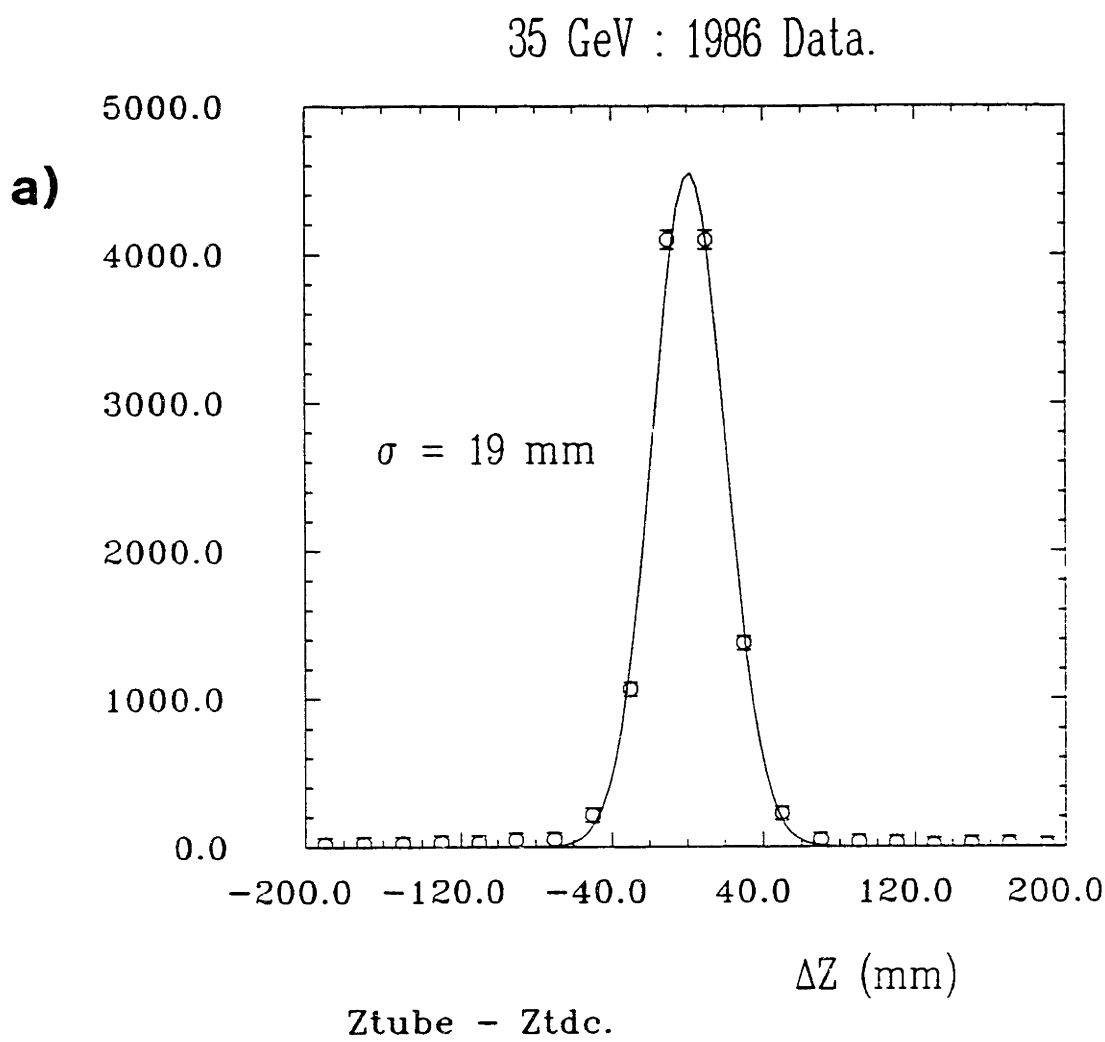
35 GeV : 1986 Data.
a)
5000.0
4000.0
3000.0
2000.0
1000.0
0.0
σ = 19 mm
−200.0 −120.0 −40.0 40.0 120.0 200.0
ΔZ (mm)
Ztube − Ztdc.
b)
2000.0
1500.0
1000.0
500.0
0.0
σ=46 mm
−250.0−150.0 −50.0 50.0 150.0 250.0
ΔZ (mm)
Ztube − Zadc

Figure 4.8

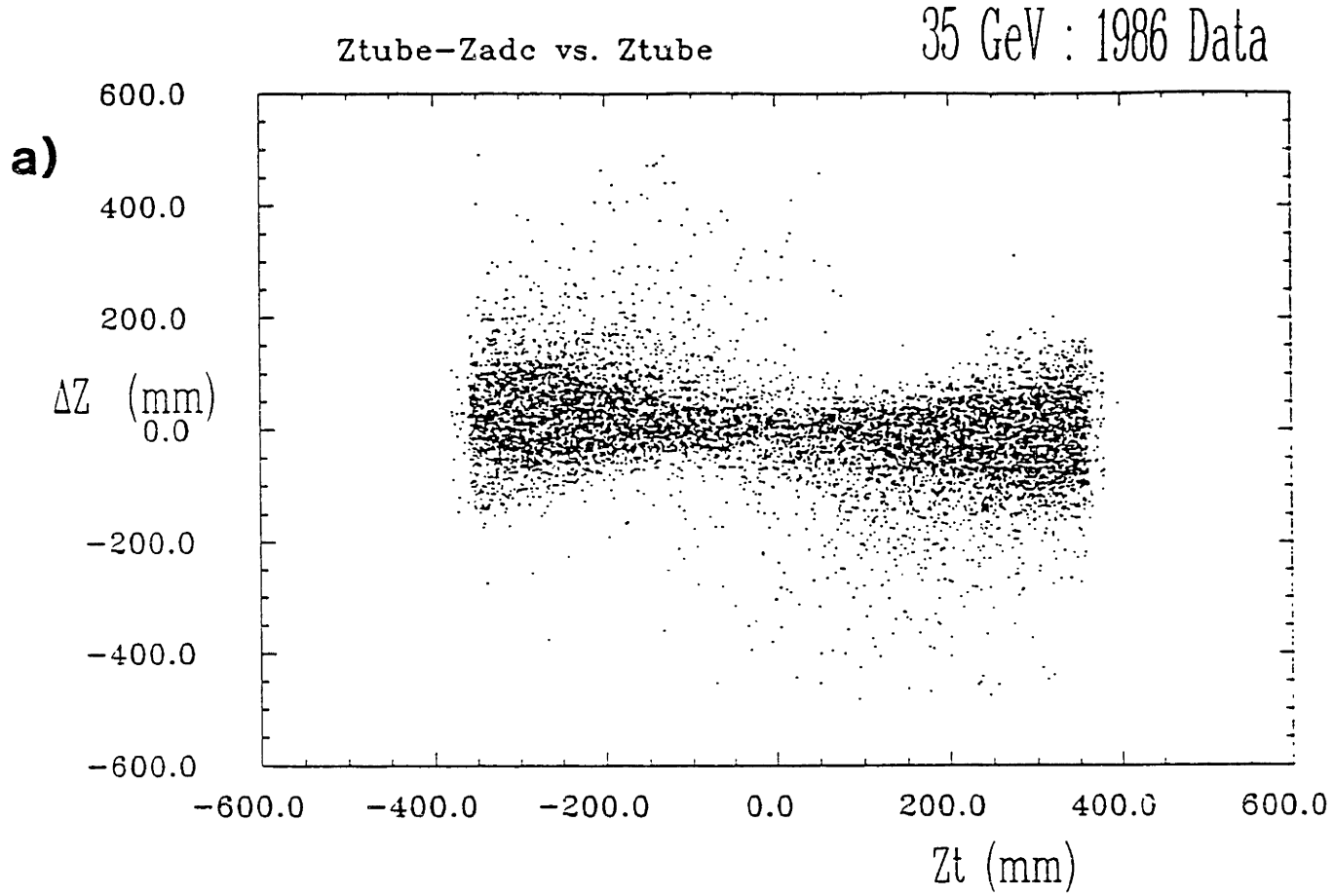
Ztube−Zadc vs. Ztube
35 GeV : 1986 Data
a)
600.0
400.0
200.0
ΔZ (mm)
0.0
−200.0
−400.0
−600.0
−600.0
−400.0
−200.0
0.0
200.0
400.0
600.0
Zt (mm)

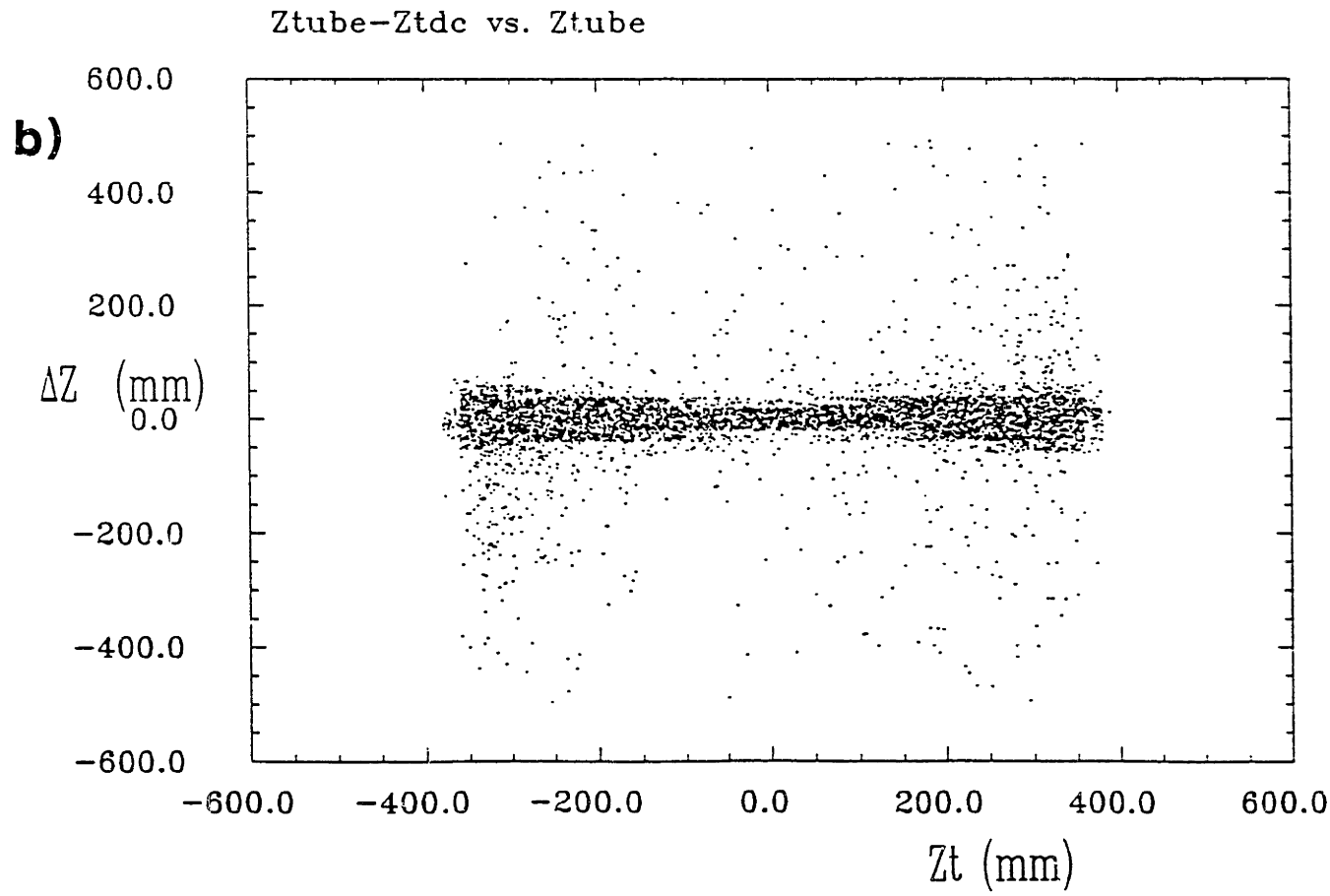
Ztube−Ztdc vs. Ztube
b)
600.0
400.0
200.0
ΔZ (mm)
0.0
−200.0
−400.0
−600.0
−600.0
−400.0
−200.0
0.0
200.0
400.0
600.0
Zt (mm)

Figure 4.9

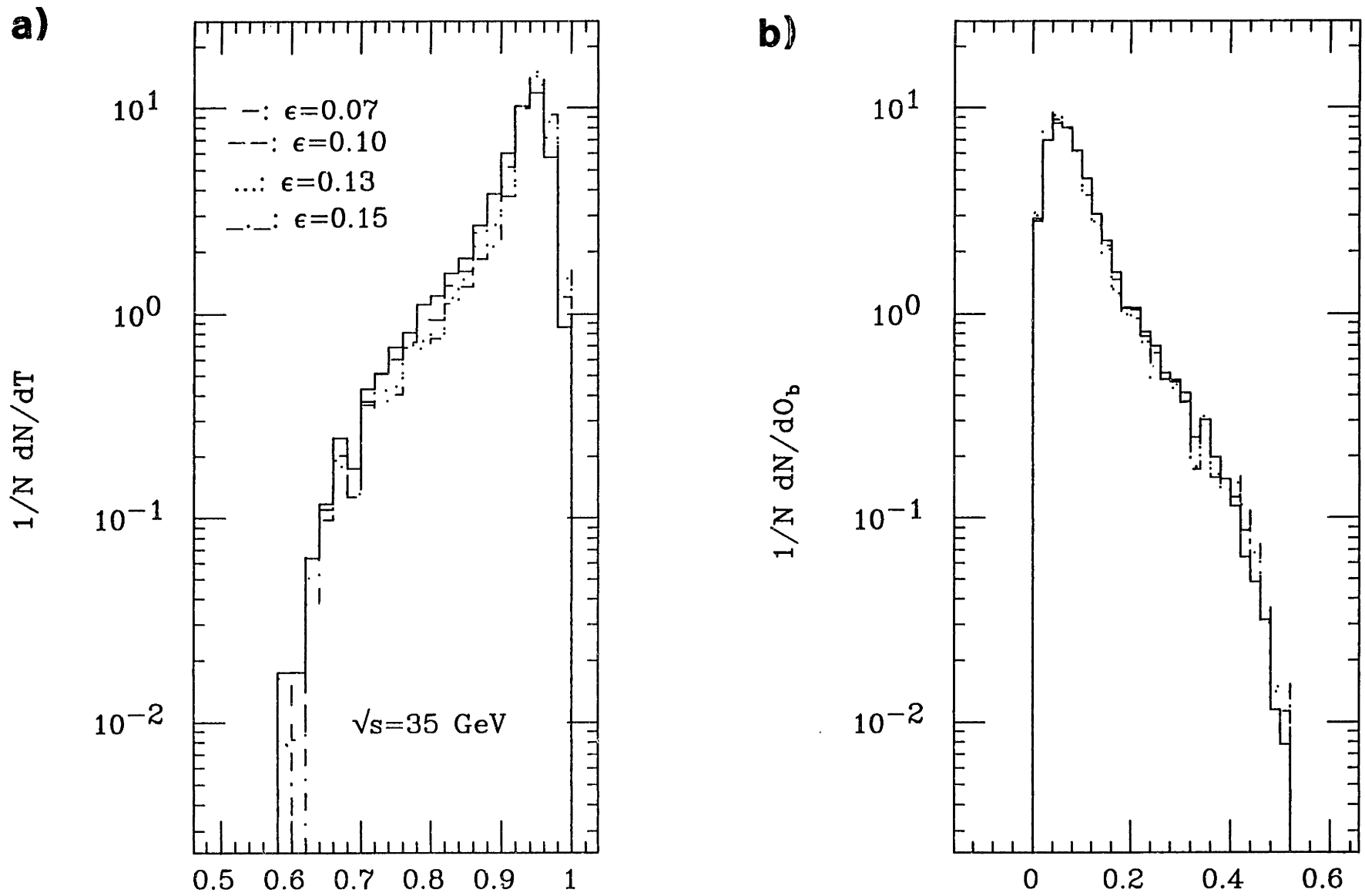
Thrust vs. (ϵ,δ) cuts.
a)
1/N dN/dT
10^1
10^0
10^-1
10^-2
–: ϵ=0.07
– –: ϵ=0.10
...: ϵ=0.13
_._: ϵ=0.15
√s=35 GeV
0.5
0.6
0.7
0.8
0.9
1
Oblateness vs. (ϵ,δ) cuts.
b)
1/N dN/dO_b
10^1
10^0
10^-1
10^-2
0
0.2
0.4
0.6

Figure 5.1

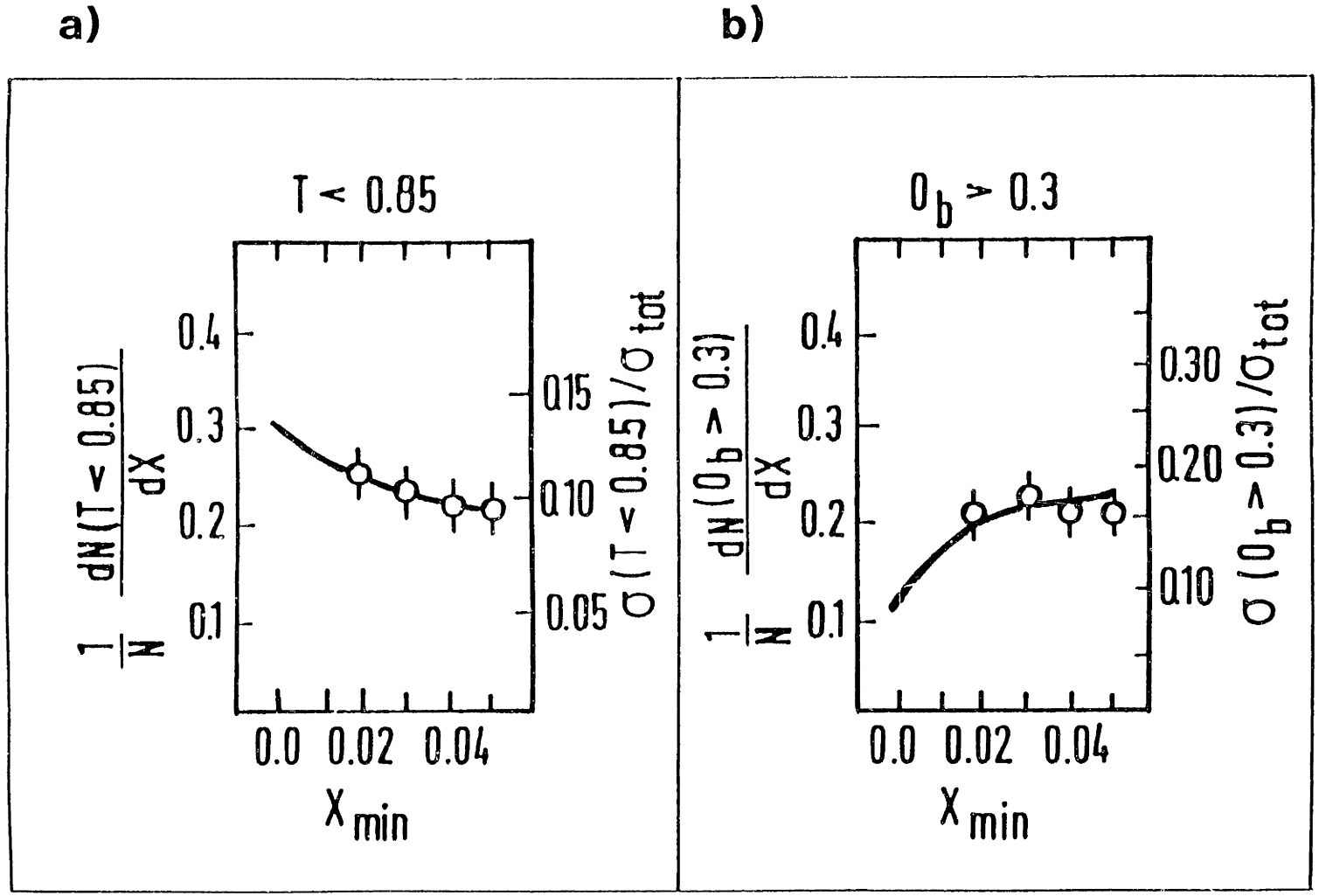
a)
b)
T < 0.85
O_b > 0.3
$\frac{1}{N}\frac{dN(T<0.85)}{dX}$
$\frac{1}{N}\frac{dN(O_b>0.3)}{dX}$
$\sigma(T<0.85)/\sigma_{tot}$
$\sigma(O_b>0.3)/\sigma_{tot}$
0.4
0.3
0.2
0.1
0.15
0.10
0.05
0.30
0.20
0.10
0.0
0.02
0.04
X_{min}

Figure 5.2

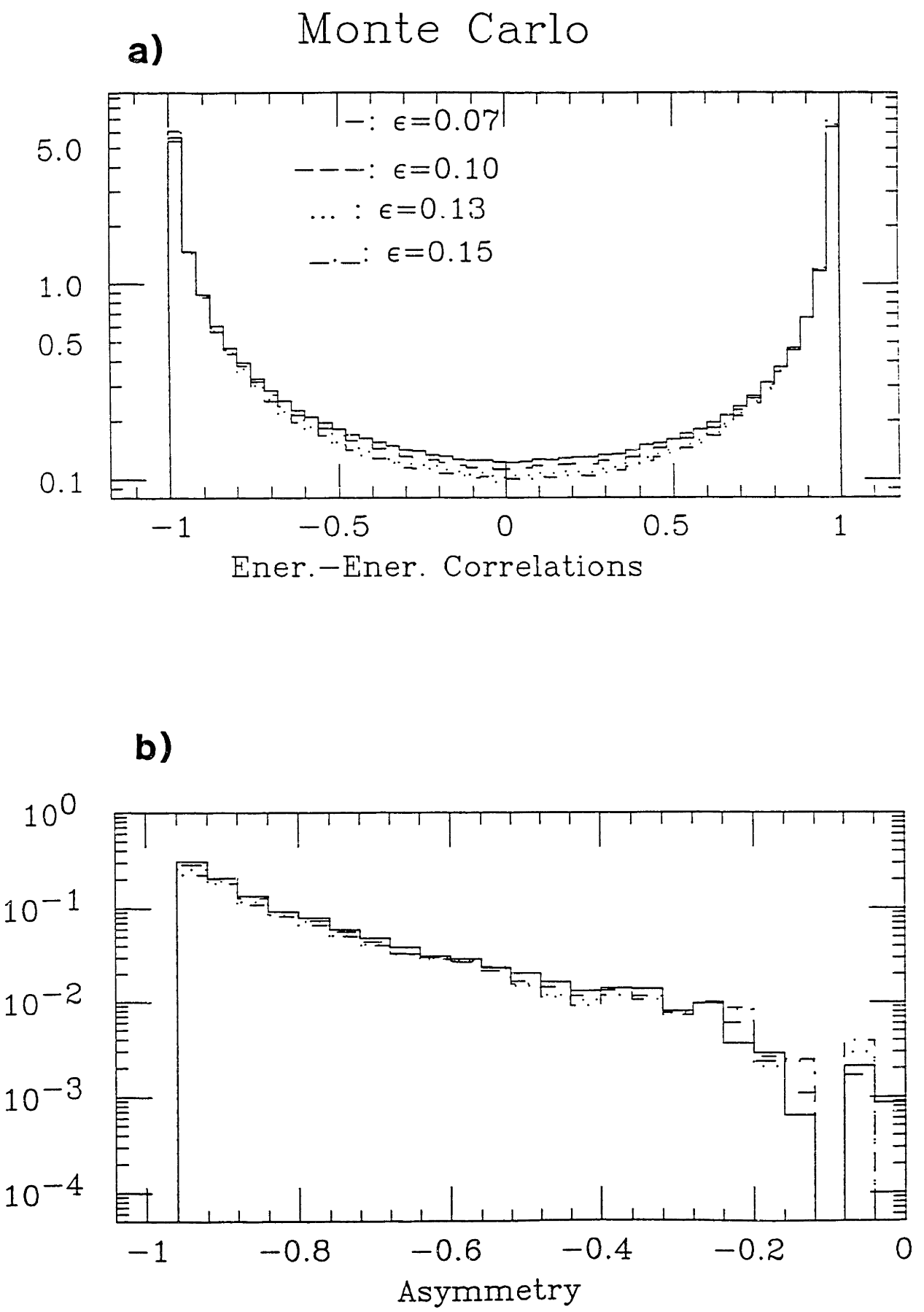
Monte Carlo
a)
—: ϵ=0.07
– – –: ϵ=0.10
... : ϵ=0.13
_._: ϵ=0.15
5.0
1.0
0.5
0.1
−1
−0.5
0
0.5
1
Ener.−Ener. Correlations
b)
10^0
10^−1
10^−2
10^−3
10^−4
−1
−0.8
−0.6
−0.4
−0.2
0
Asymmetry

Figure 5.3

a) EEC: Y cut Dependence.

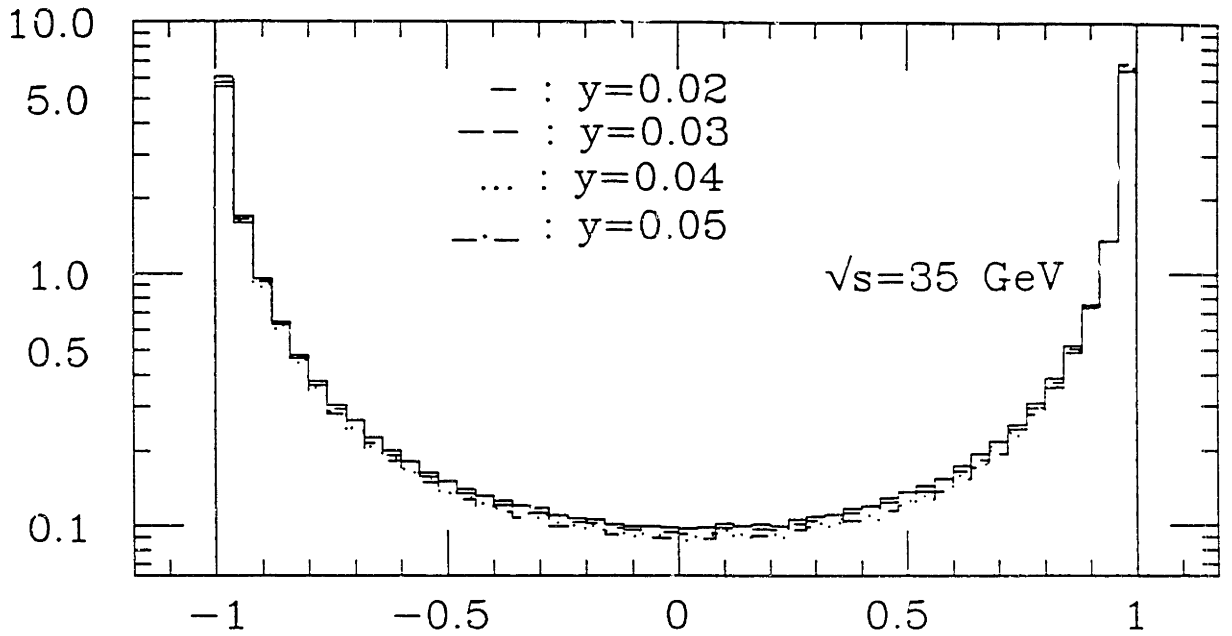

b) ASY: Y cut Dependence.

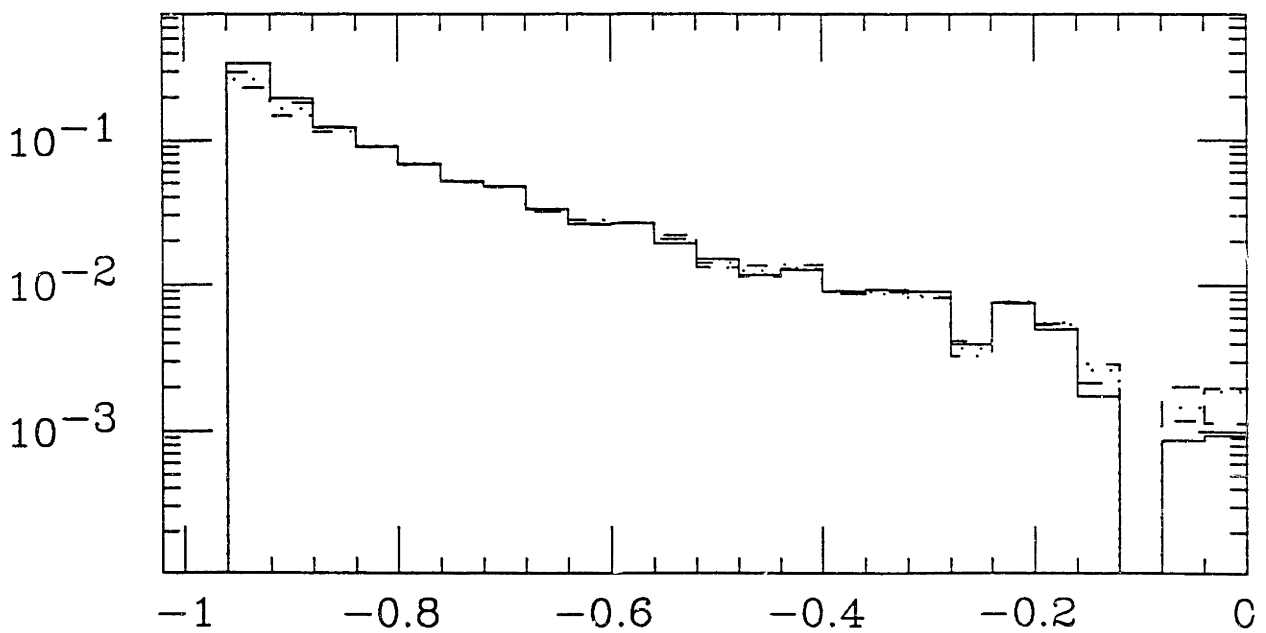

Figure 5.4

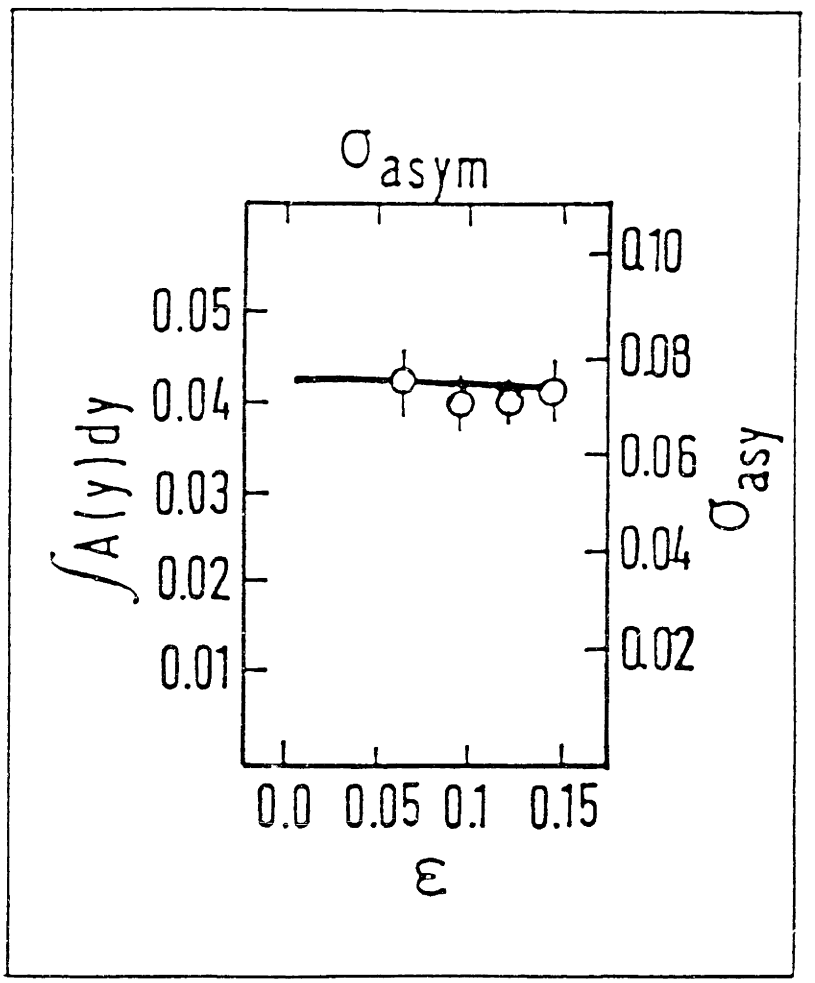
σasym
0.05
0.04
0.03
0.02
0.01
∫A(y)dy
0.10
0.08
0.06
0.04
0.02
σasy
0.0
0.05
0.1
0.15
ε

Figure 5.5

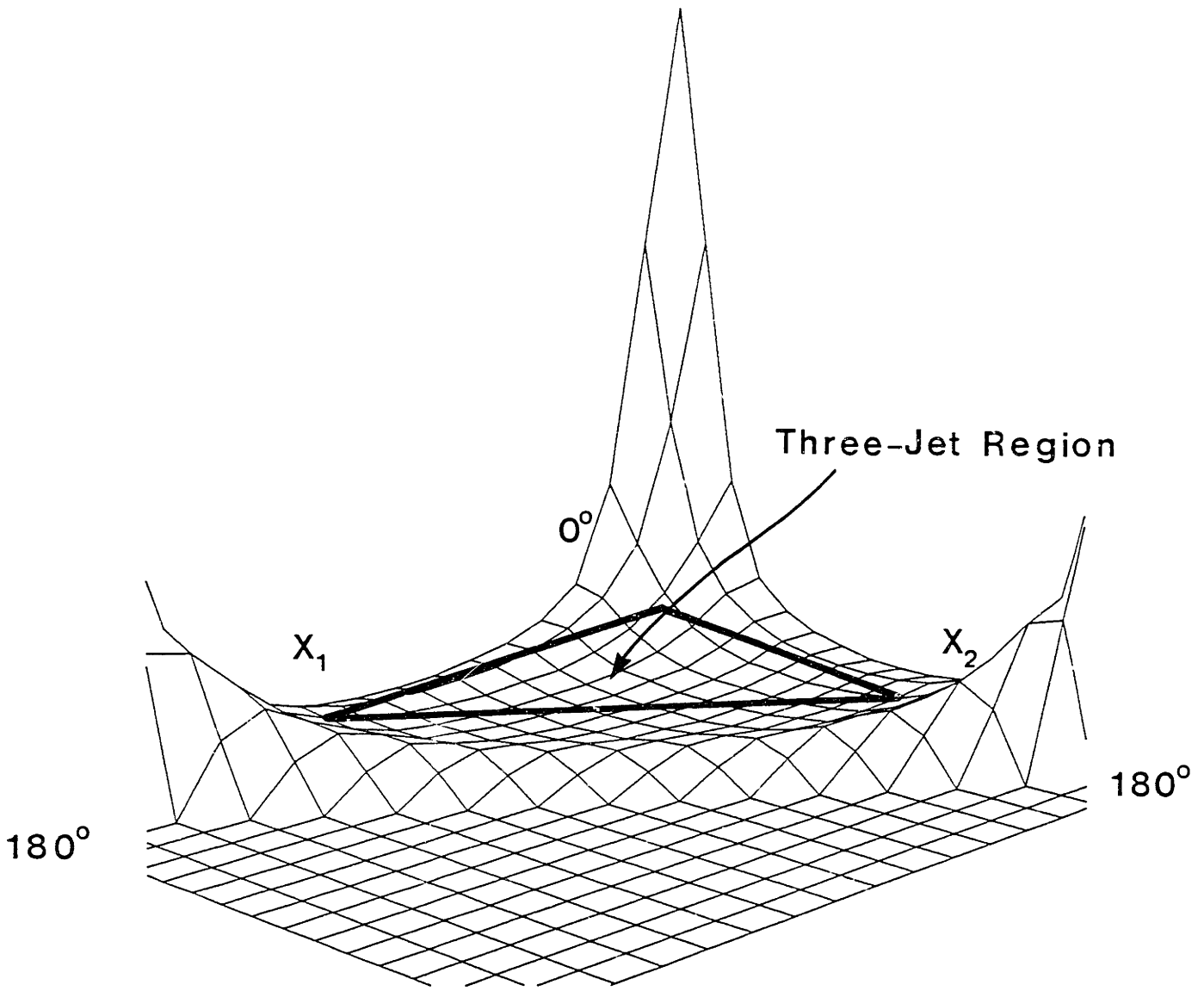

PTC

Figure 5.6

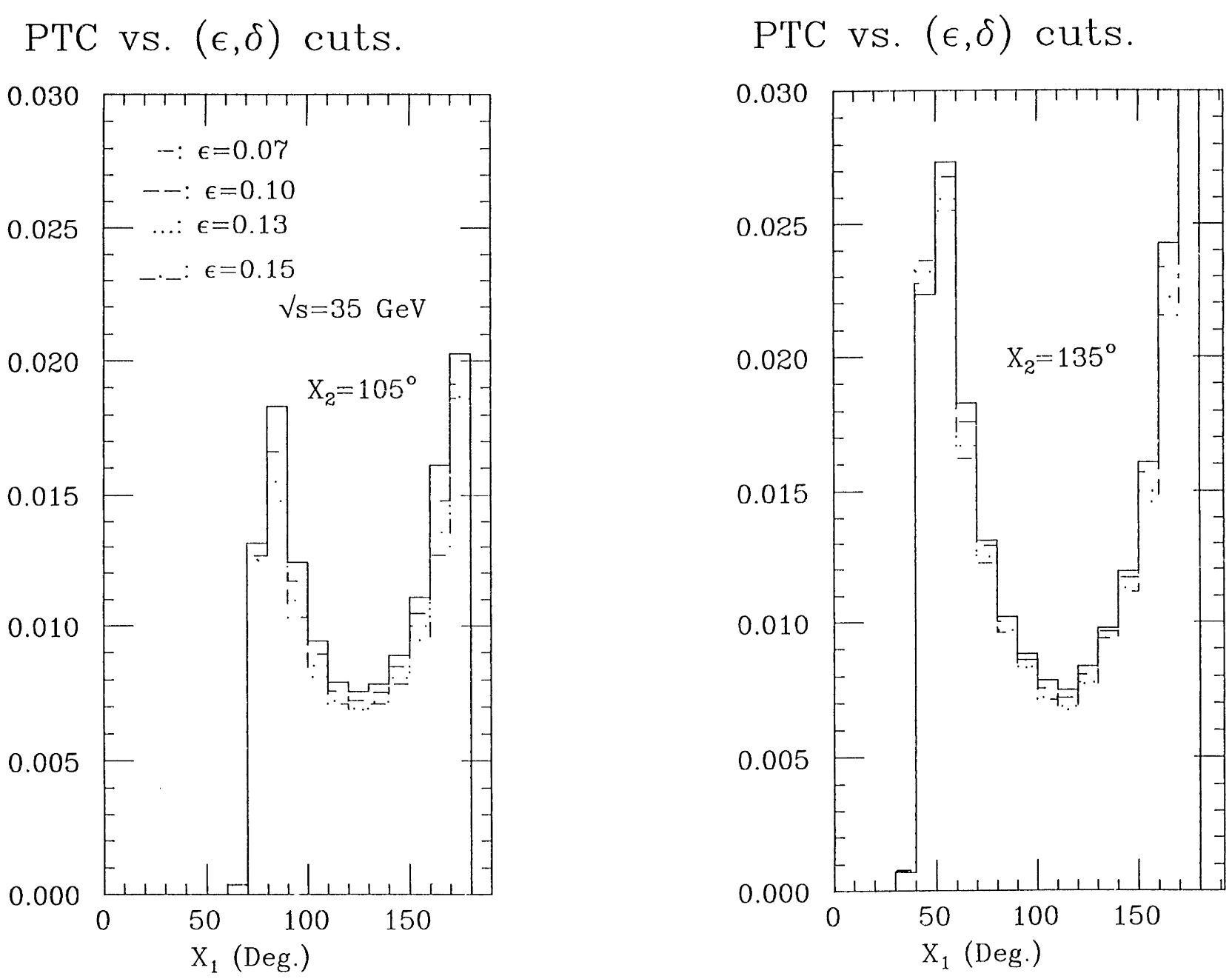
PTC vs. (ϵ,δ) cuts.
0.030
0.025
0.020
0.015
0.010
0.005
0.000
—: ϵ=0.07
– –: ϵ=0.10
...: ϵ=0.13
_._: ϵ=0.15
√s=35 GeV
X2=105°
0
50
100
150
X1 (Deg.)
PTC vs. (ϵ,δ) cuts.
X2=135°
X1 (Deg.)

Figure 5.7

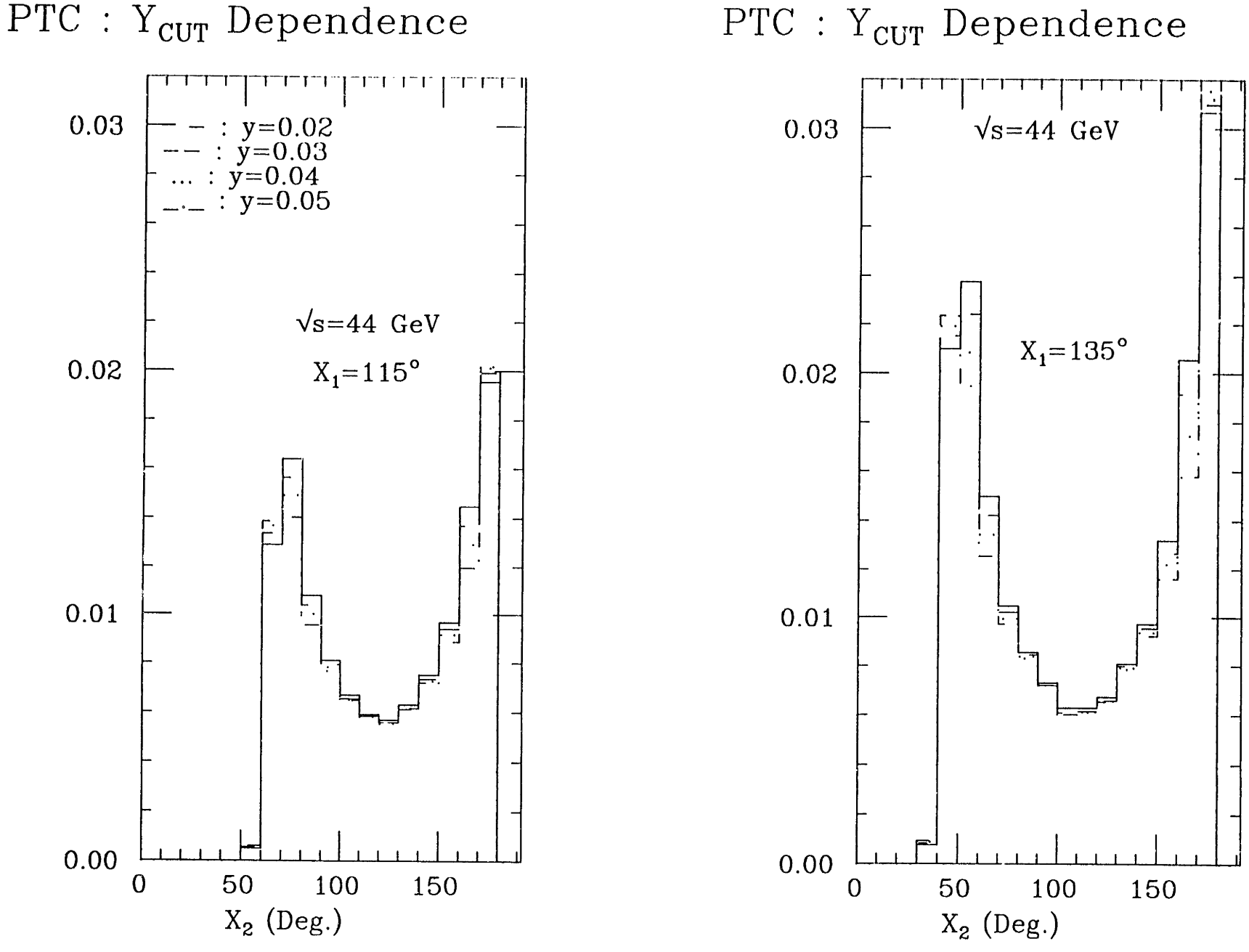
PTC : Y_{CUT} Dependence
0.03
0.02
0.01
0.00
— : y=0.02
-- : y=0.03
... : y=0.04
-·- : y=0.05
√s=44 GeV
X_1=115°
0
50
100
150
X_2 (Deg.)
PTC : Y_{CUT} Dependence
0.03
0.02
0.01
0.00
√s=44 GeV
X_1=135°
0
50
100
150
X_2 (Deg.)

Figure 5.8

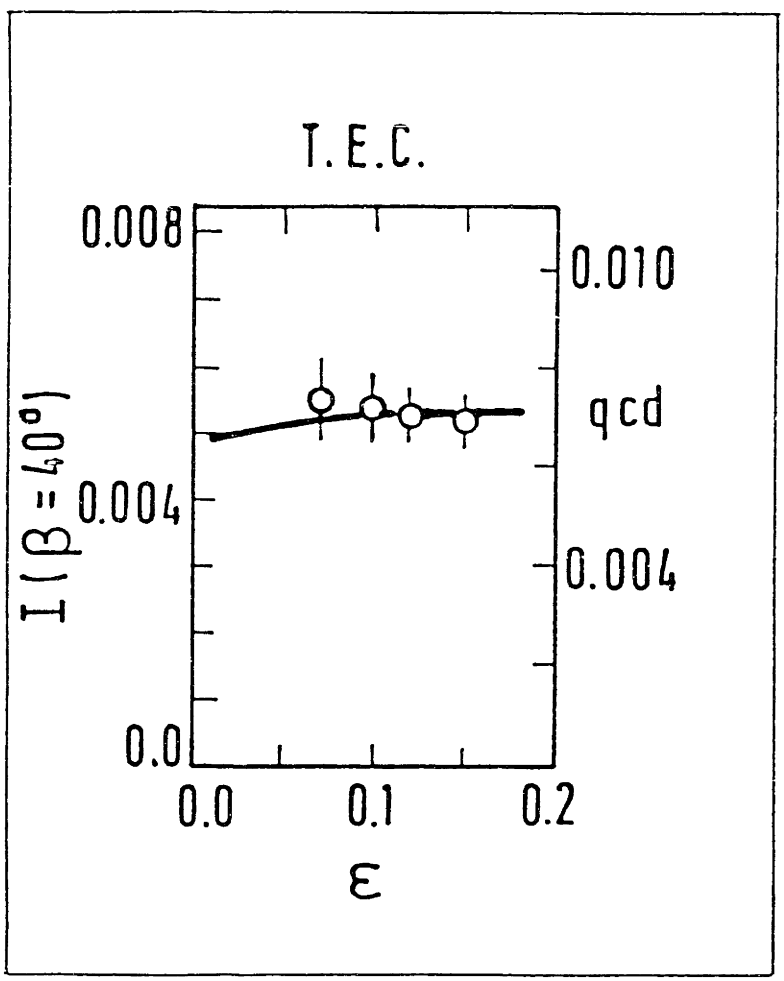

Figure 5.9

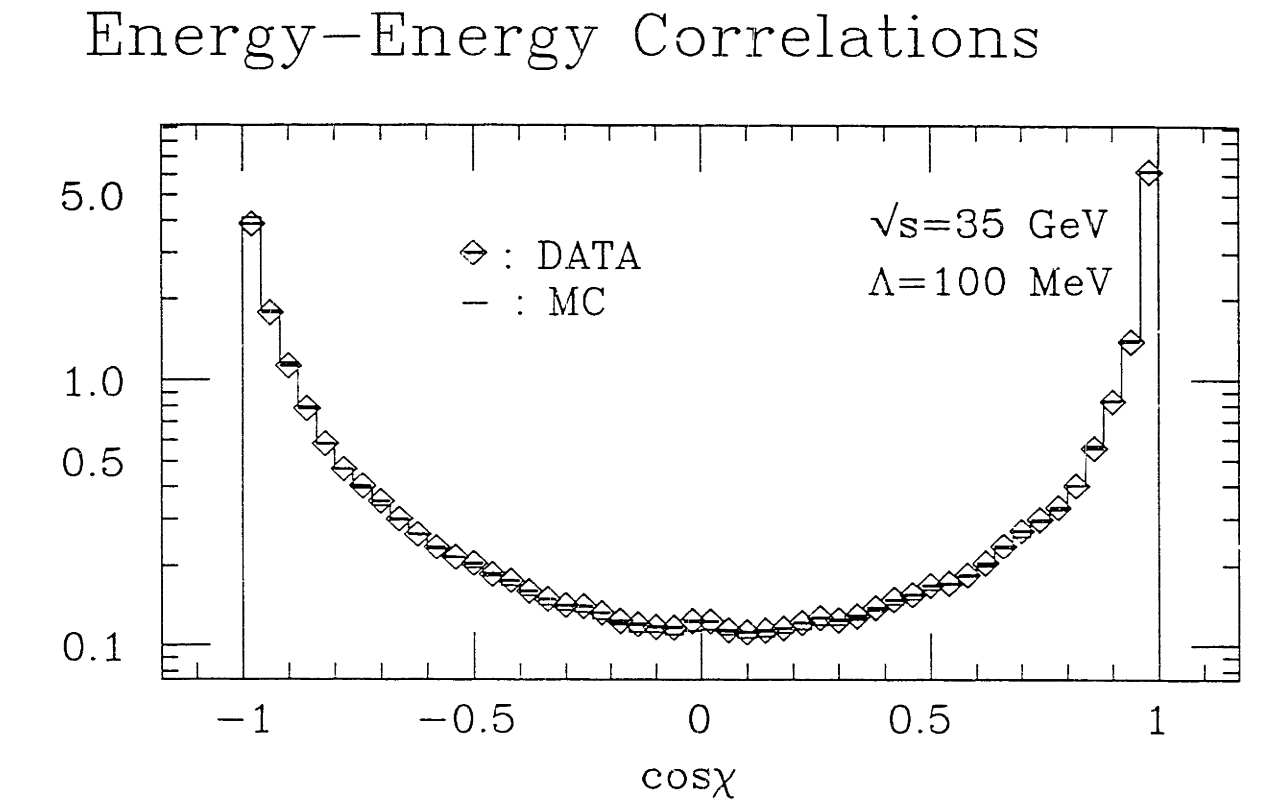
Energy–Energy Correlations
5.0
1.0
0.5
0.1
◇ : DATA
– : MC
√s=35 GeV
Λ=100 MeV
−1
−0.5
0
0.5
1
cosχ

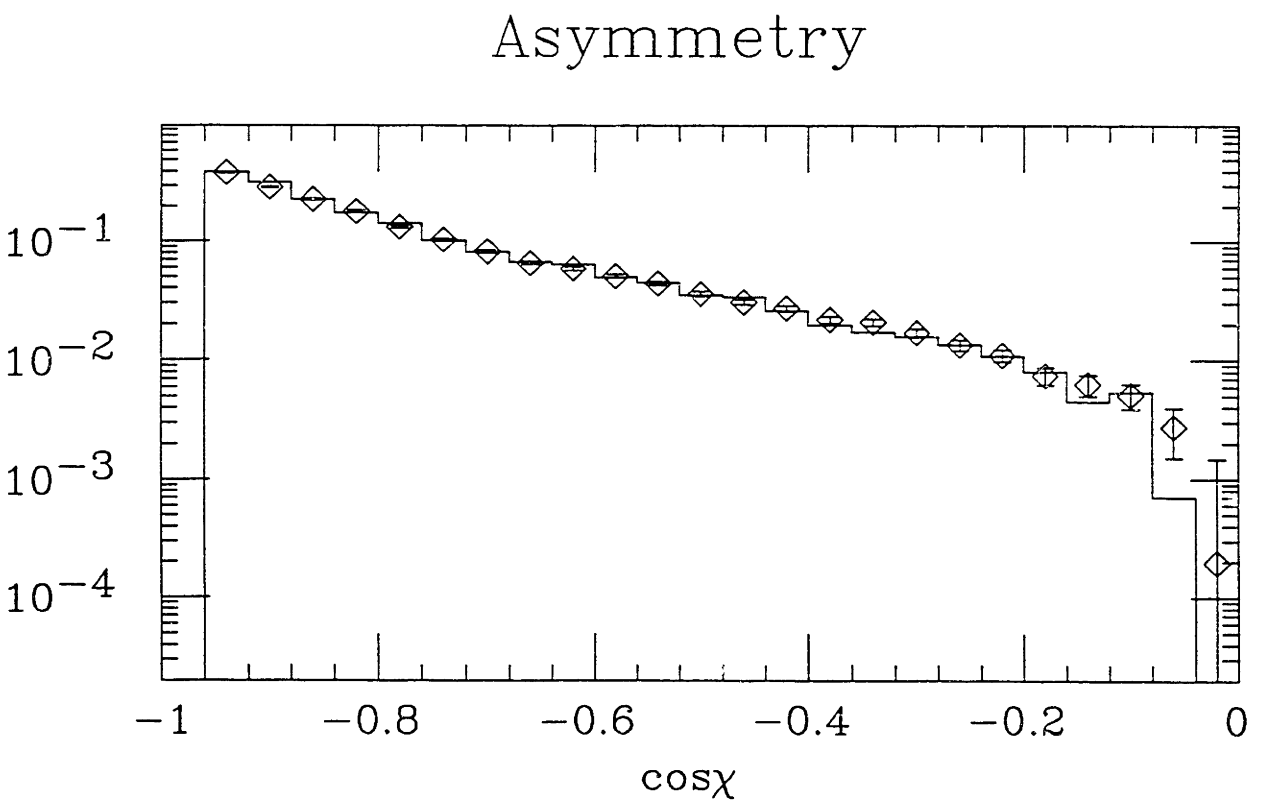
Asymmetry
10^{-1}
10^{-2}
10^{-3}
10^{-4}
−1
−0.8
−0.6
−0.4
−0.2
0
cosχ

Figure 5.10

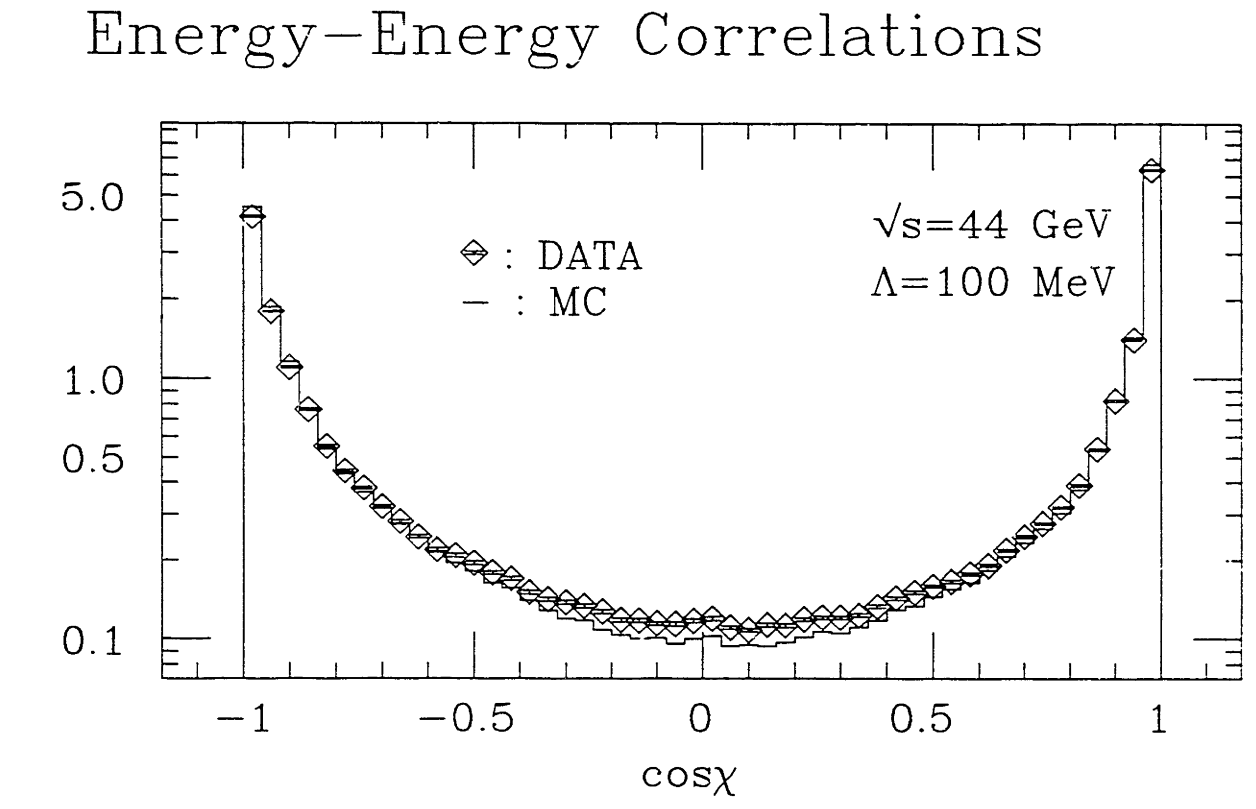
Energy–Energy Correlations
5.0
1.0
0.5
0.1
◈ : DATA
– : MC
√s=44 GeV
Λ=100 MeV
−1
−0.5
0
0.5
1
cosχ

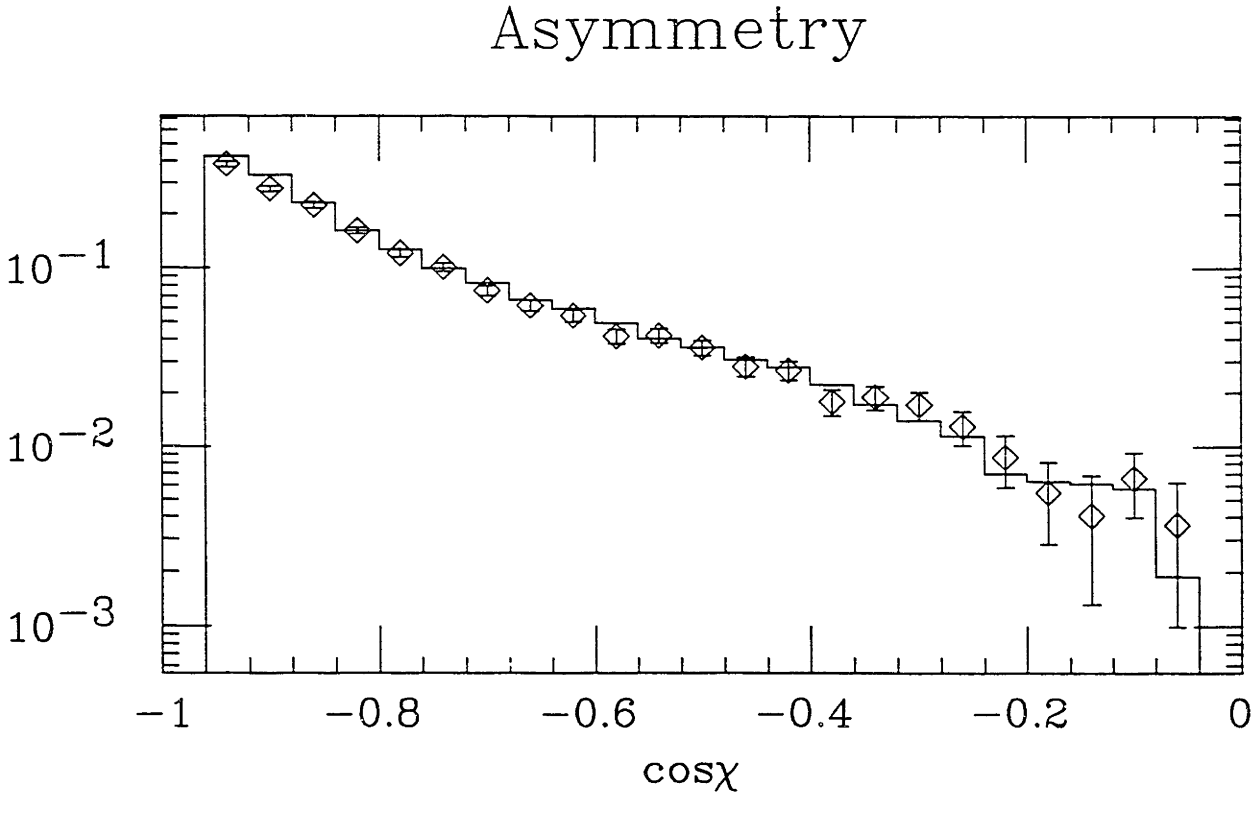
Asymmetry
10^{-1}
10^{-2}
10^{-3}
−1
−0.8
−0.6
−0.4
−0.2
0
cosχ

Figure 5.11

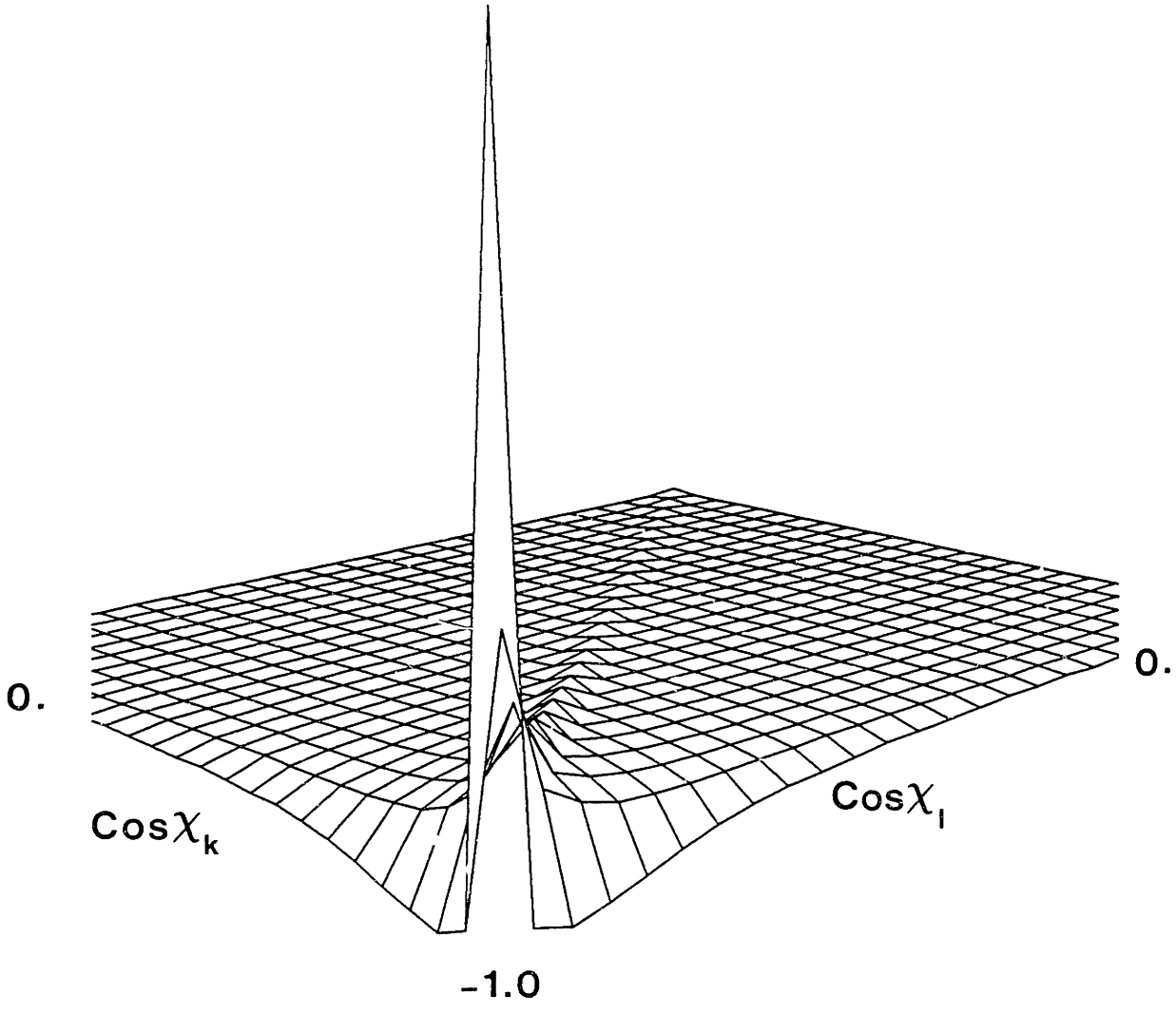

Asymmetry Correlation Matrix

Figure 5.12

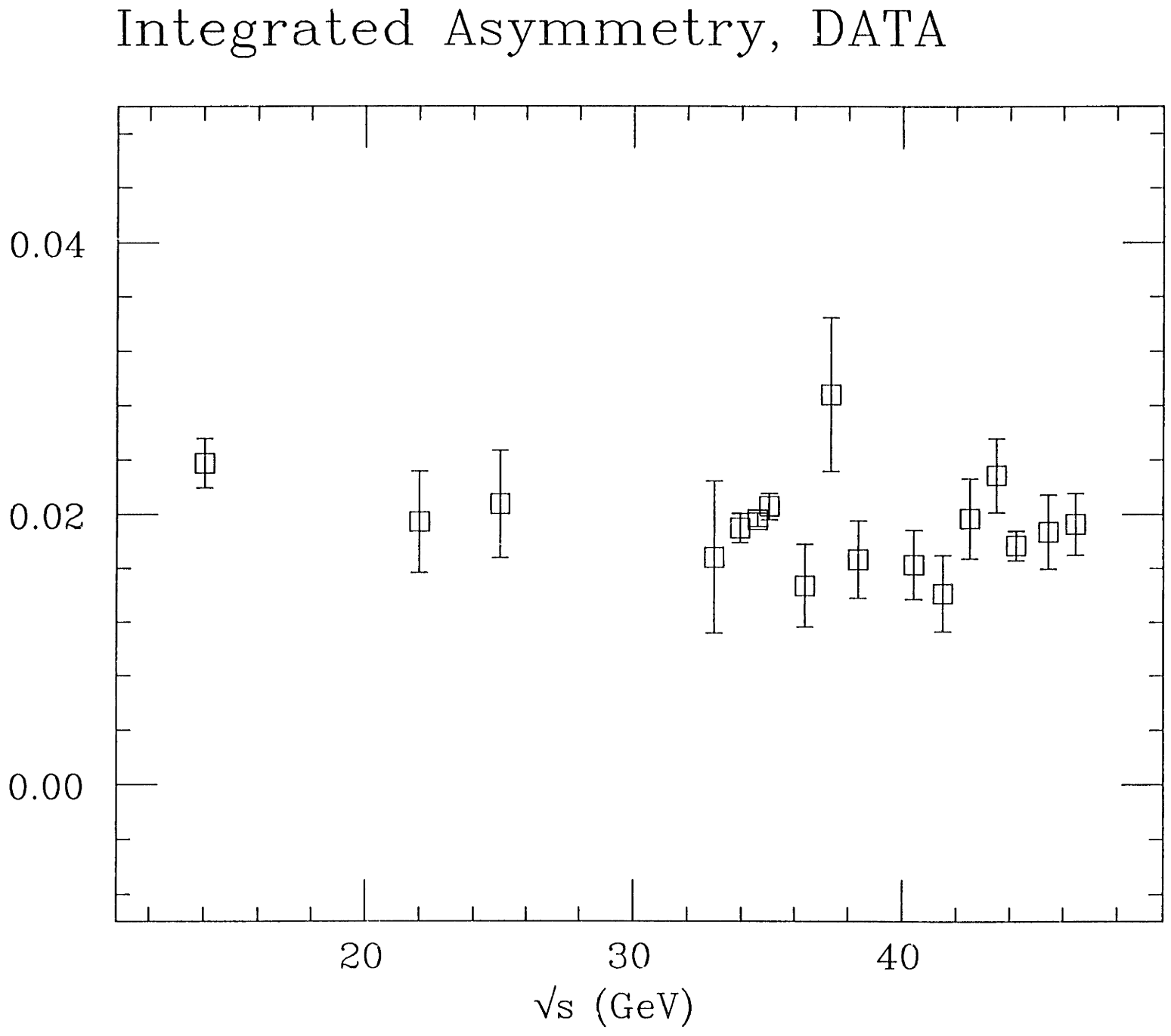

Figure 5.13

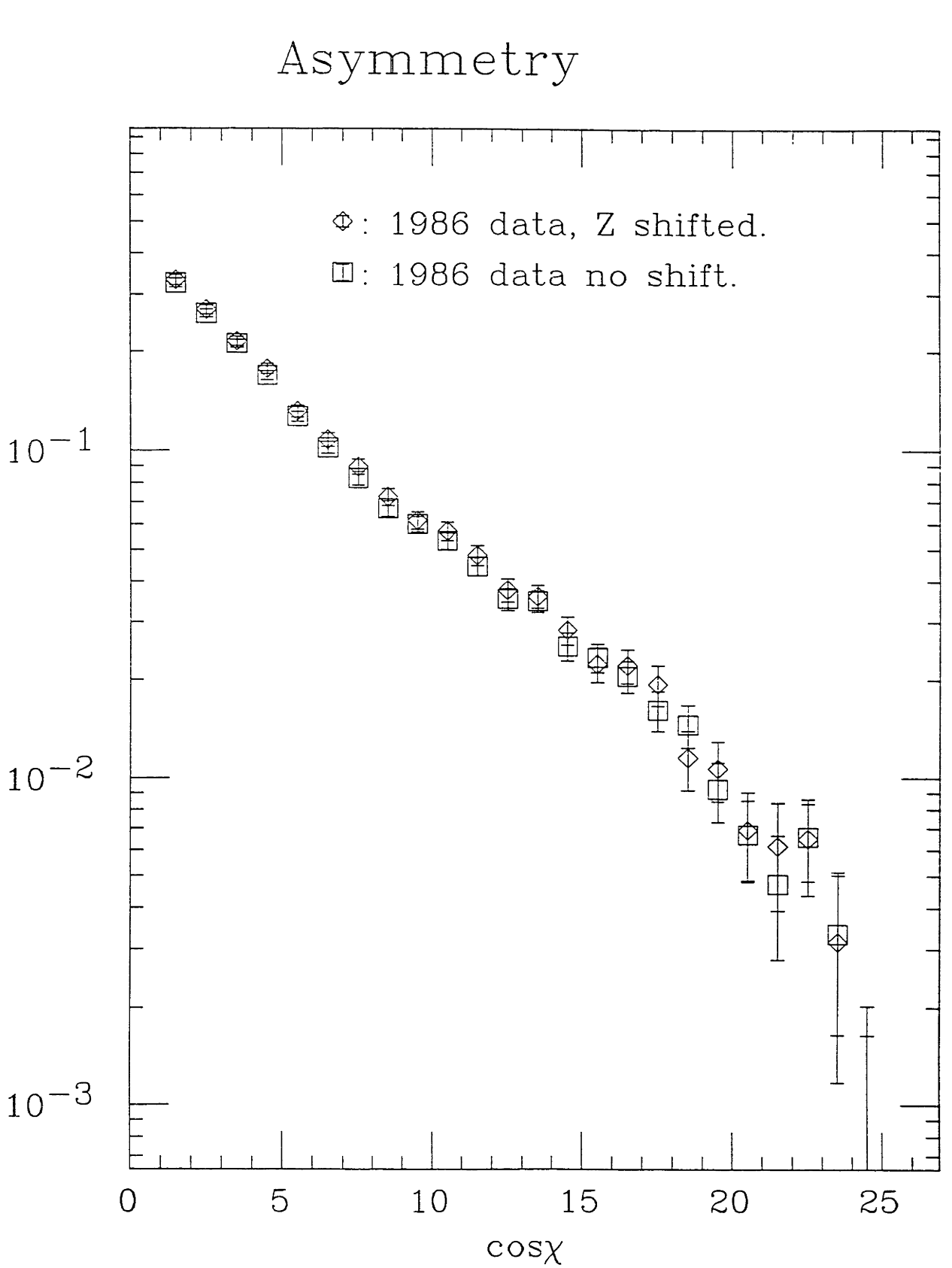
Asymmetry
◇: 1986 data, Z shifted.
□: 1986 data no shift.
10^{-1}
10^{-2}
10^{-3}
0
5
10
15
20
25
cosχ

Figure 5.14

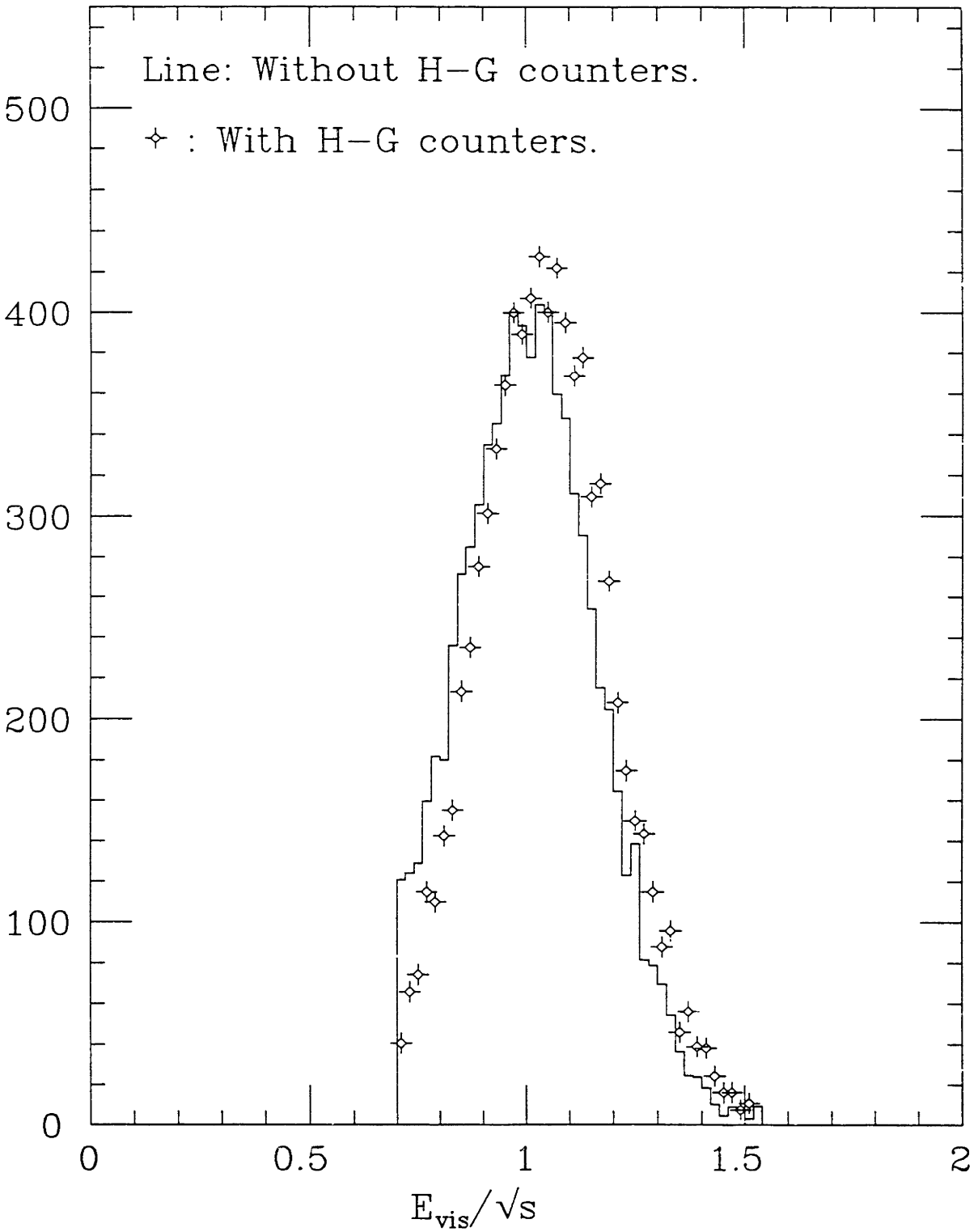
1986 Data
Line: Without H−G counters.
: With H−G counters.
500
400
300
200
100
0
0
0.5
1
1.5
2
$E_{vis}/\sqrt{s}$

Figure 5.15

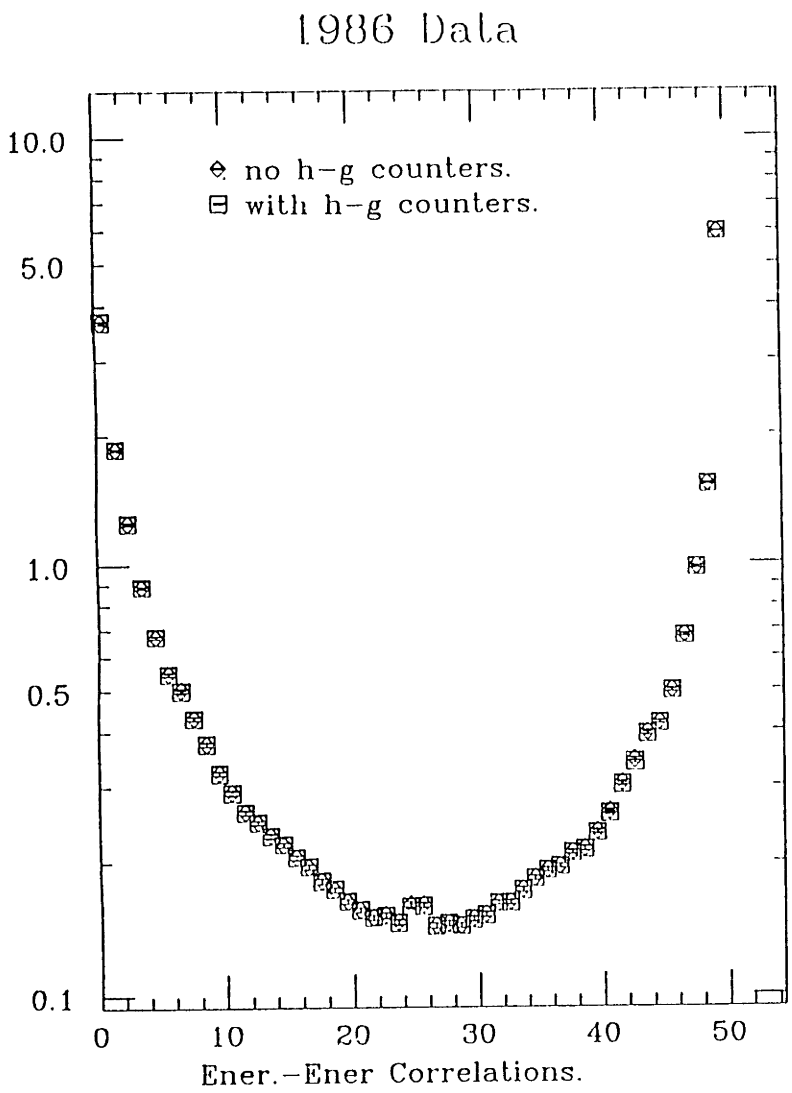
1986 Data
no h-g counters.
with h-g counters.
10.0
5.0
1.0
0.5
0.1
0
10
20
30
40
50
Ener.-Ener Correlations.

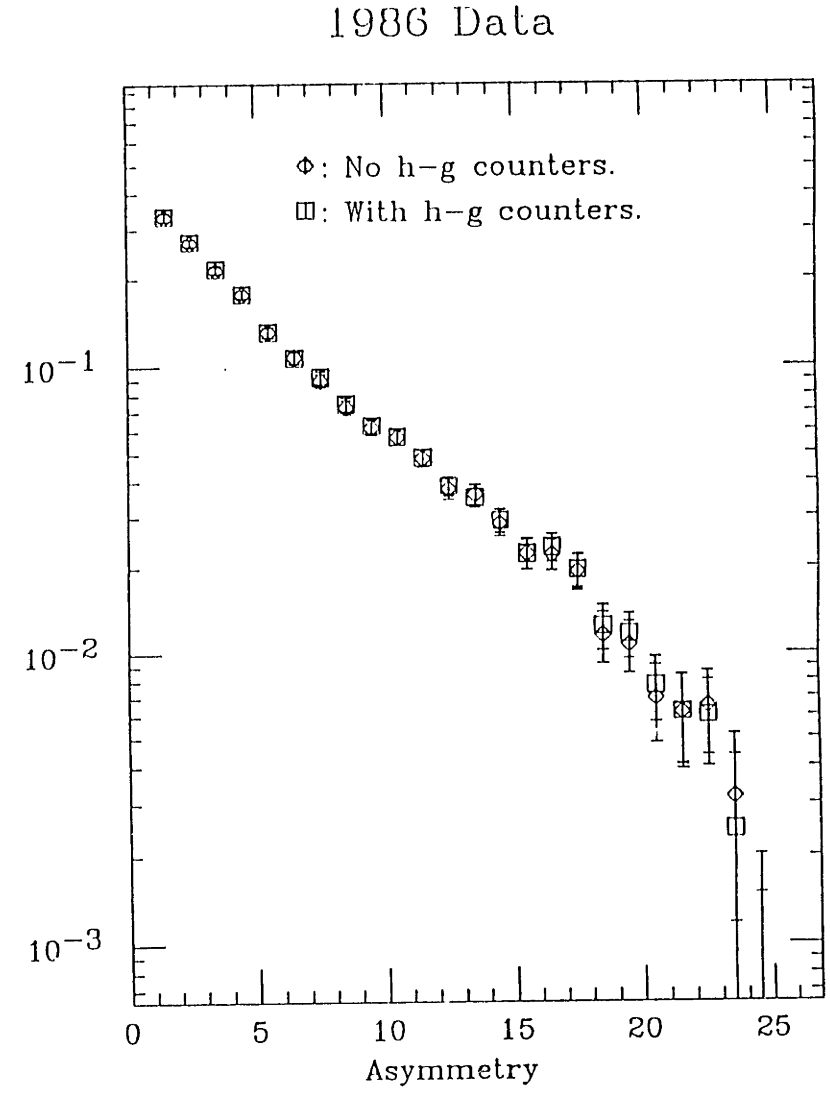
1986 Data
: No h-g counters.
: With h-g counters.
10^{-1}
10^{-2}
10^{-3}
0
5
10
15
20
25
Asymmetry

Figure 5.16

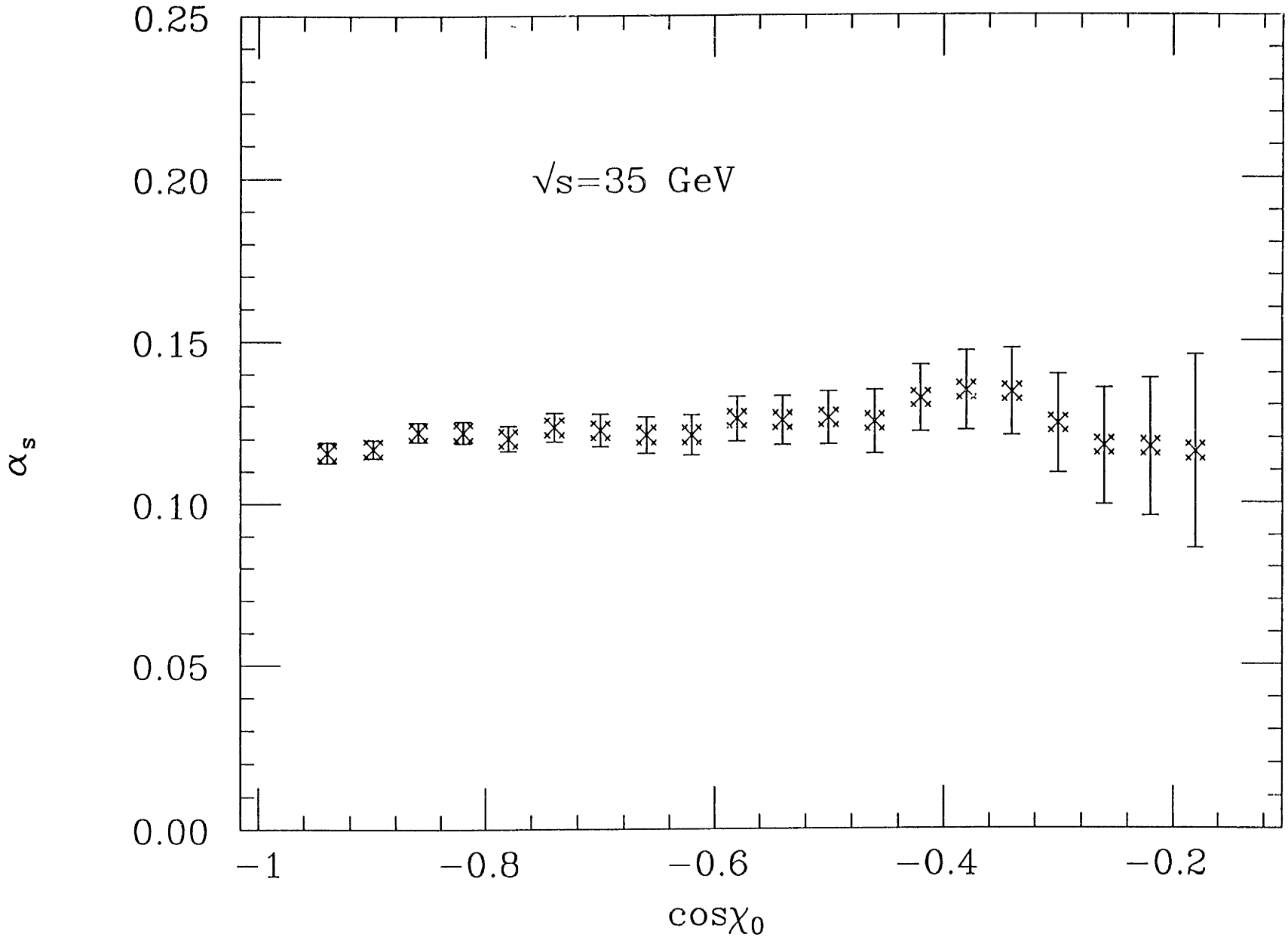
0.25
0.20
0.15
0.10
0.05
0.00
α_s
$\sqrt{s}$=35 GeV
−1
−0.8
−0.6
−0.4
−0.2
cosχ_0

Figure 5.17

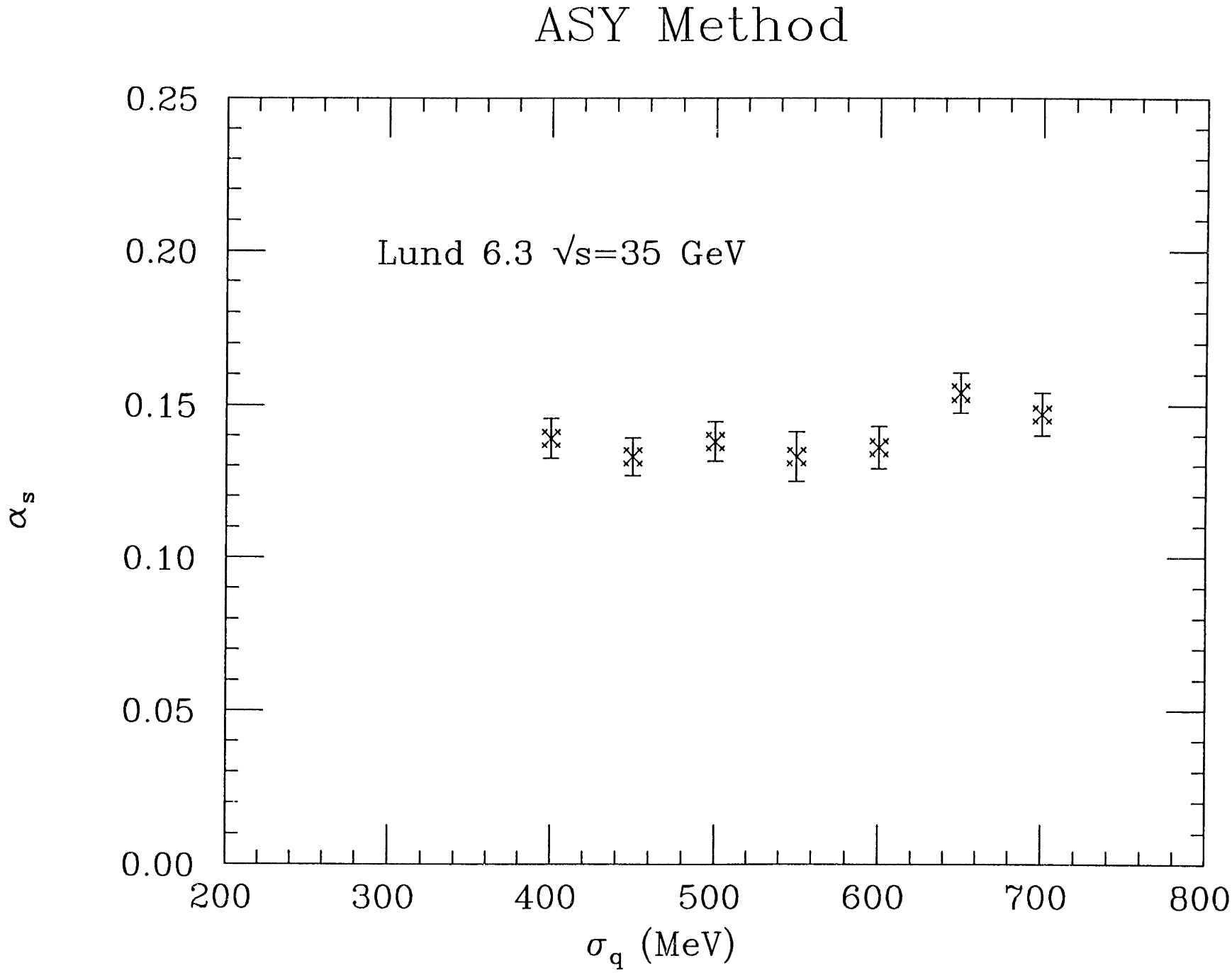
ASY Method
Lund 6.3 √s=35 GeV
0.25
0.20
0.15
0.10
0.05
0.00
α_s
200
300
400
500
600
700
800
σ_q (MeV)

Figure 5.18

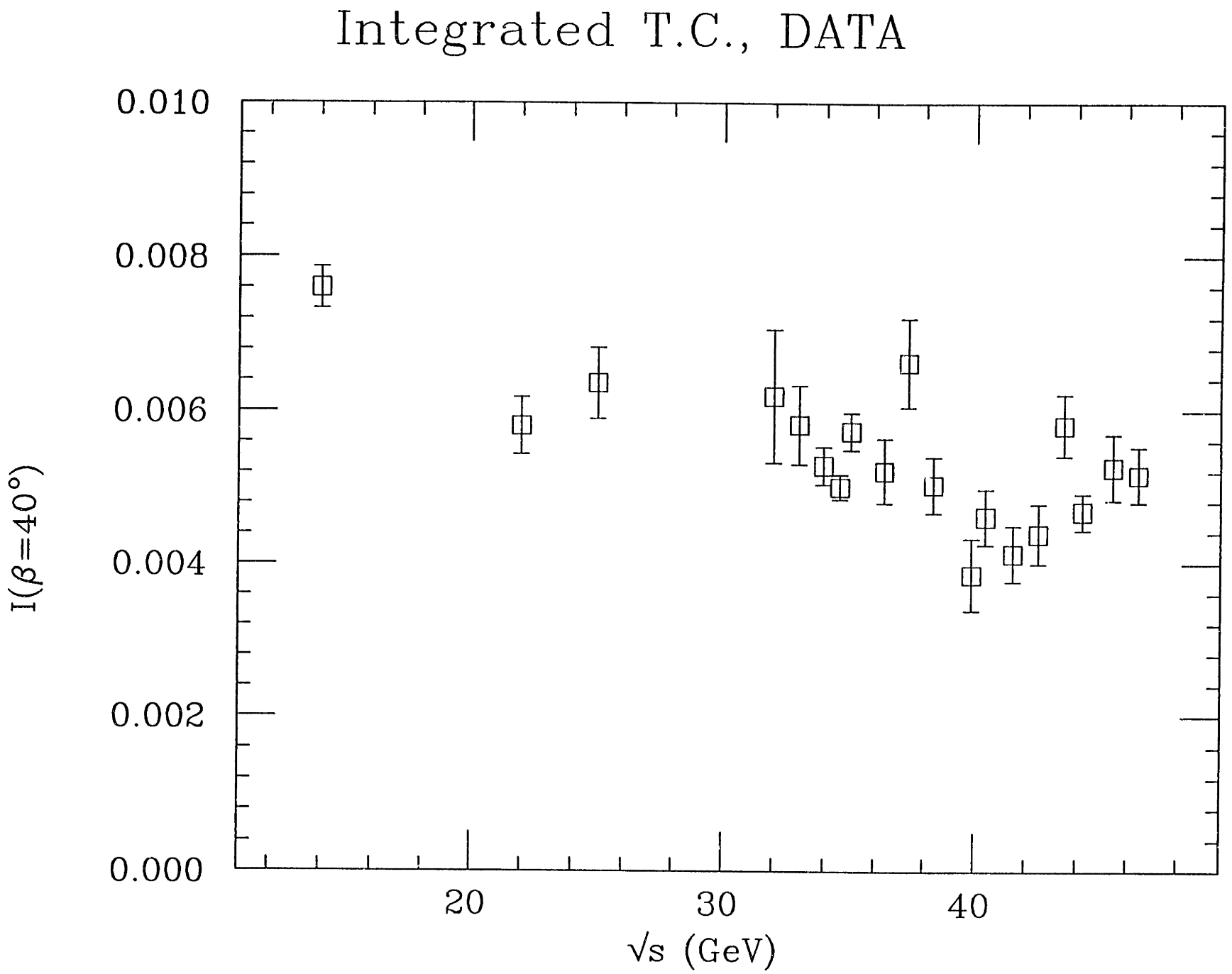
Integrated T.C., DATA
0.010
0.008
0.006
0.004
0.002
0.000
I(β=40°)
20
30
40
√s (GeV)

Figure 5.19

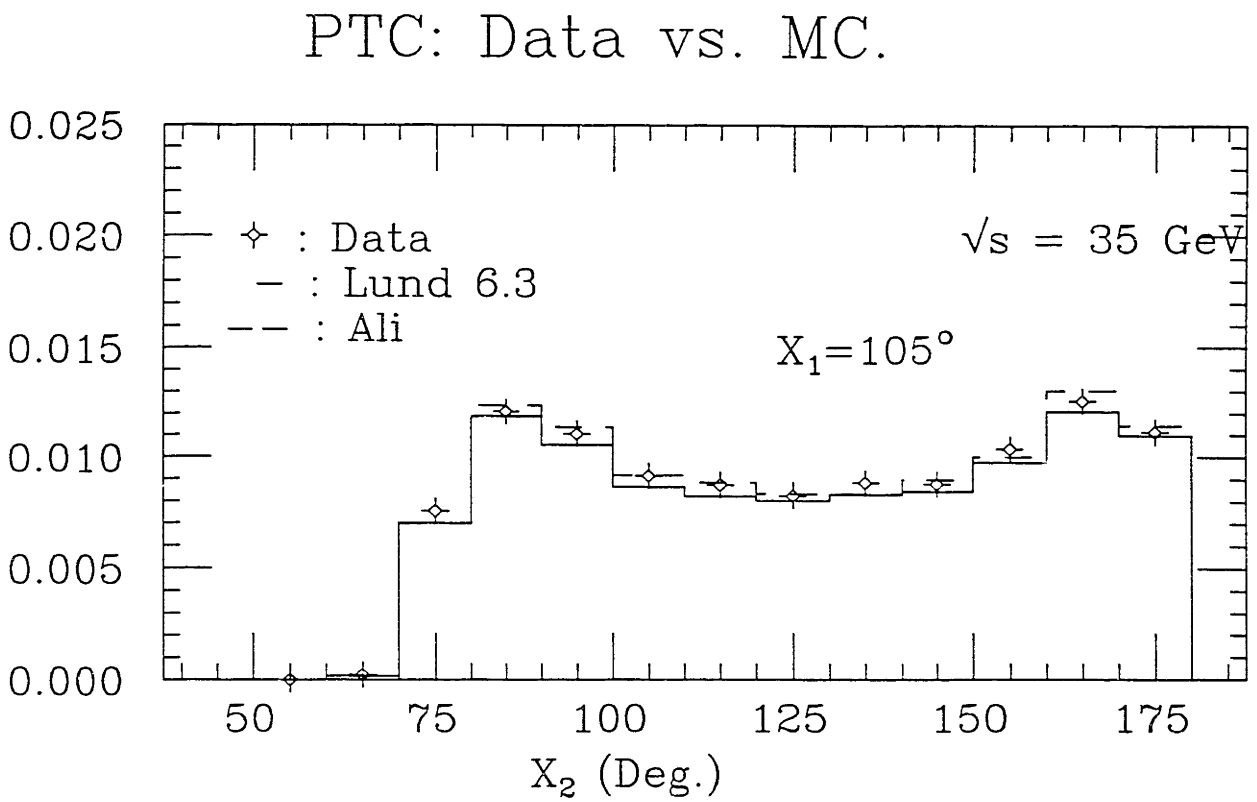
PTC: Data vs. MC.
0.025
0.020
0.015
0.010
0.005
0.000
: Data
: Lund 6.3
: Ali
√s = 35 GeV
X1=105°
50
75
100
125
150
175
X2 (Deg.)

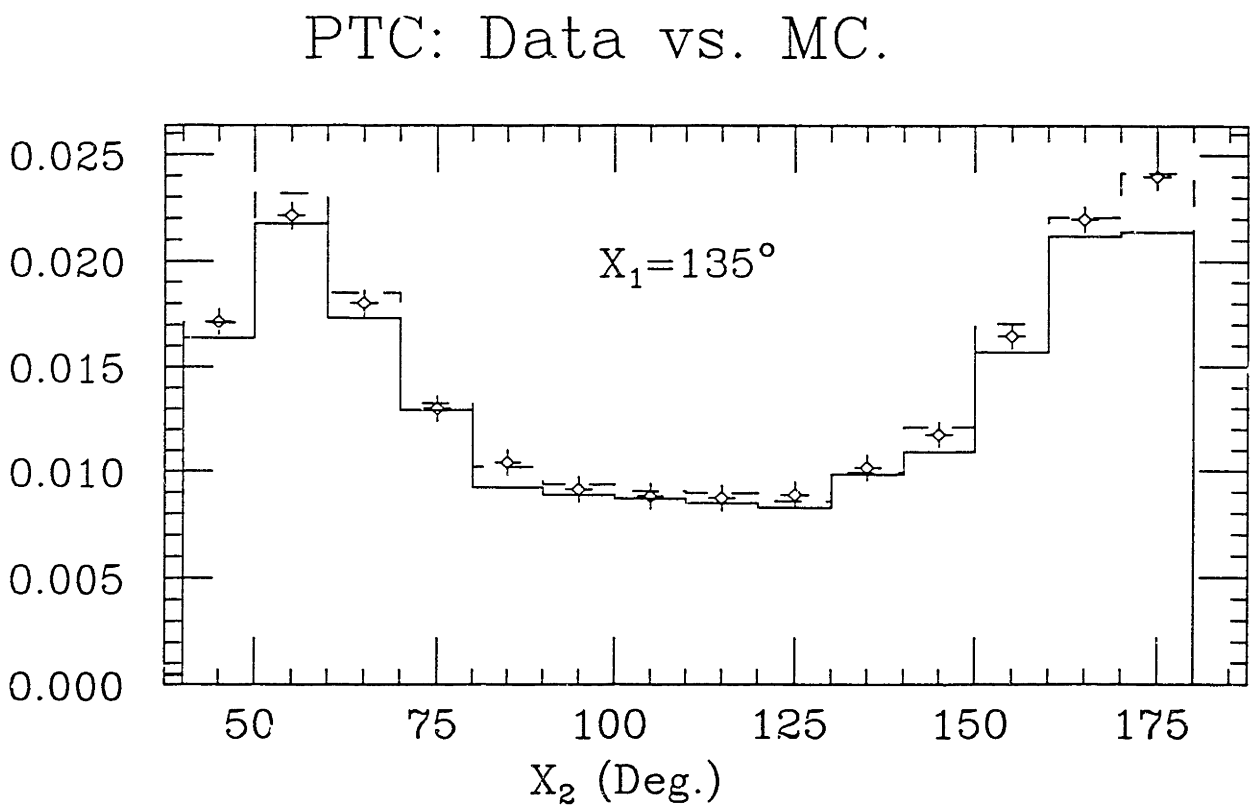
PTC: Data vs. MC.
0.025
0.020
0.015
0.010
0.005
0.000
X1=135°
50
75
100
125
150
175
X2 (Deg.)

Figure 5.20

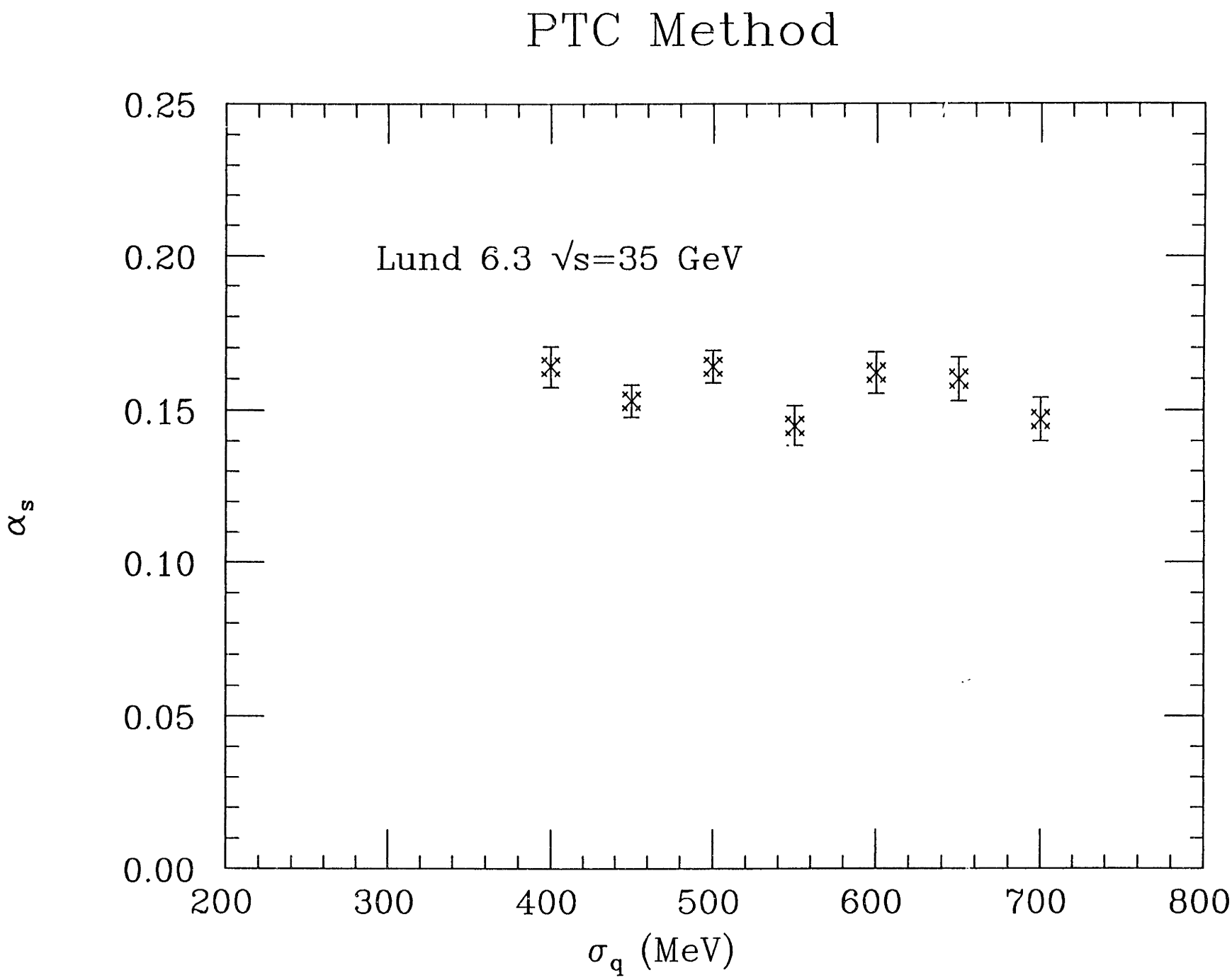
PTC Method
Lund 6.3 √s=35 GeV
0.25
0.20
0.15
0.10
0.05
0.00
α_s
200
300
400
500
600
700
800
σ_q (MeV)

Figure 5.21

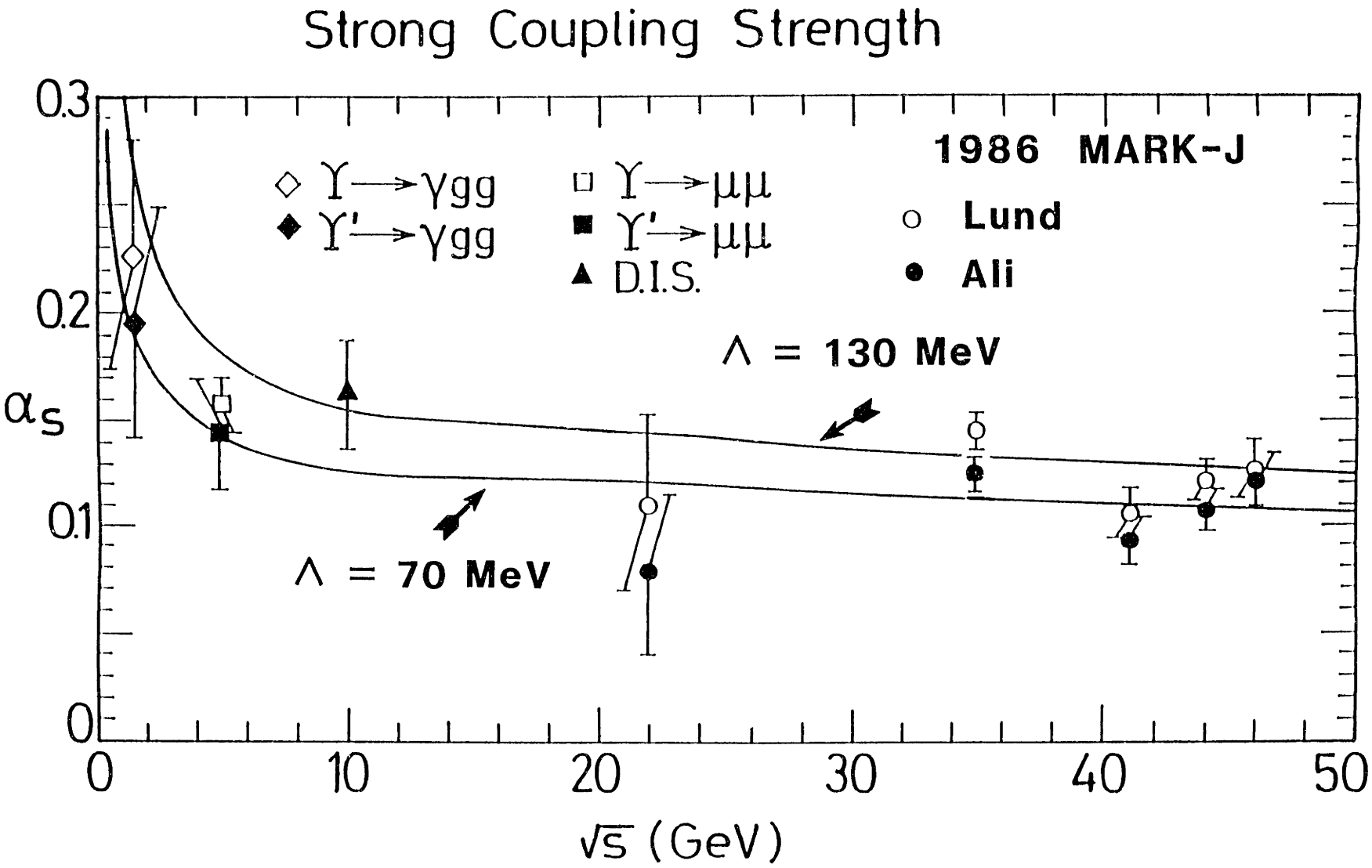
Strong Coupling Strength
1986 MARK-J
Υ → γgg
Υ' → γgg
Υ → μμ
Υ' → μμ
D.I.S.
Lund
Ali
Λ = 130 MeV
Λ = 70 MeV
α_s
0.3
0.2
0.1
0
0
10
20
30
40
50
$\sqrt{s}$ (GeV)

Figure 5.22

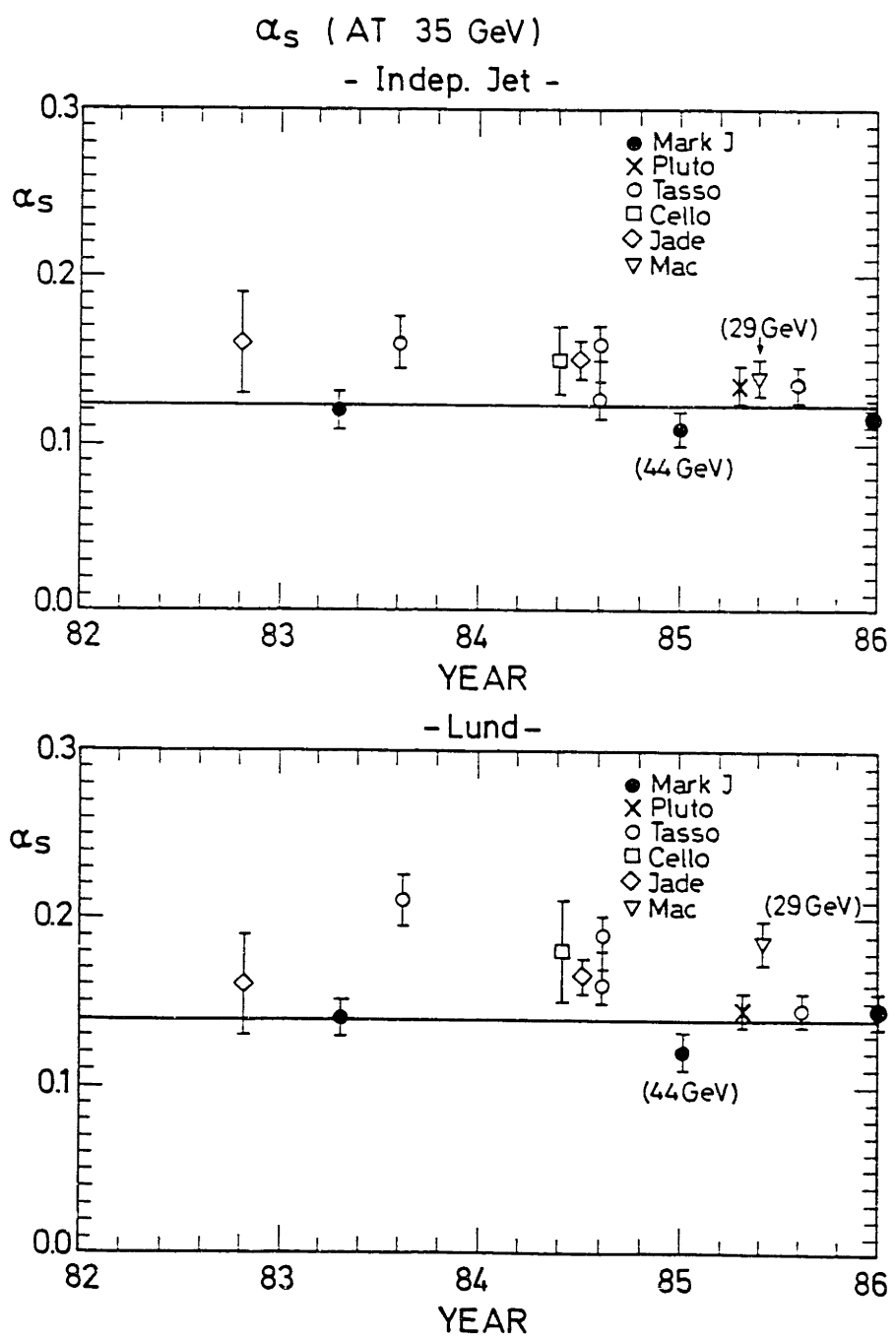
α_s (AT 35 GeV)
- Indep. Jet -
α_s
0.3
0.2
0.1
0.0
82
83
84
85
86
YEAR
Mark J
Pluto
Tasso
Cello
Jade
Mac
(29 GeV)
(44 GeV)
- Lund -
α_s
0.3
0.2
0.1
0.0
82
83
84
85
86
YEAR
Mark J
Pluto
Tasso
Cello
Jade
Mac
(29 GeV)
(44 GeV)

Figure A.1

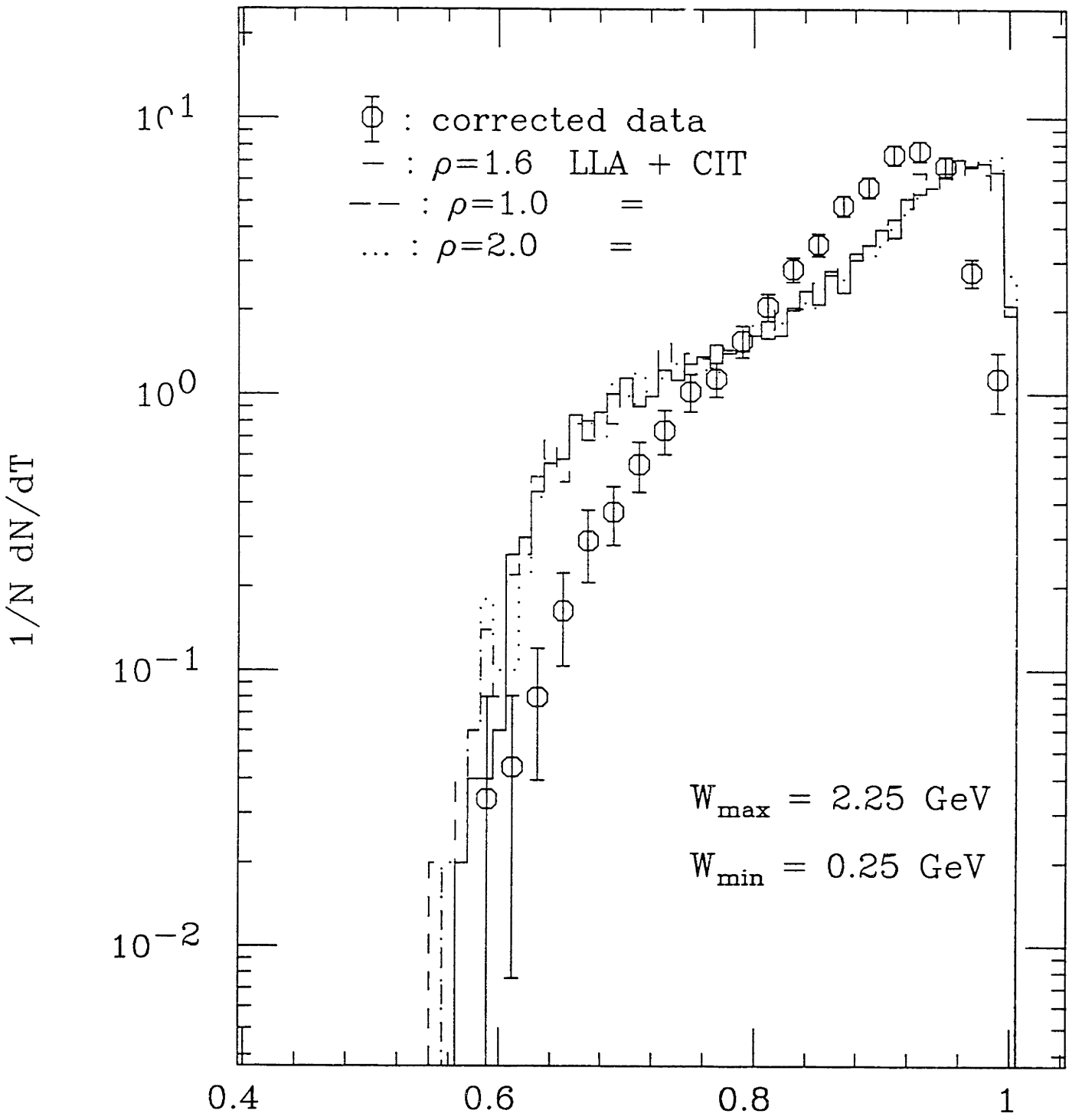
THRUST: 35 GeV
: corrected data
: ρ=1.6 LLA + CIT
: ρ=1.0 =
: ρ=2.0 =
1/N dN/dT
10^1
10^0
10^-1
10^-2
0.4
0.6
0.8
1
W_max = 2.25 GeV
W_min = 0.25 GeV

Figure B.1

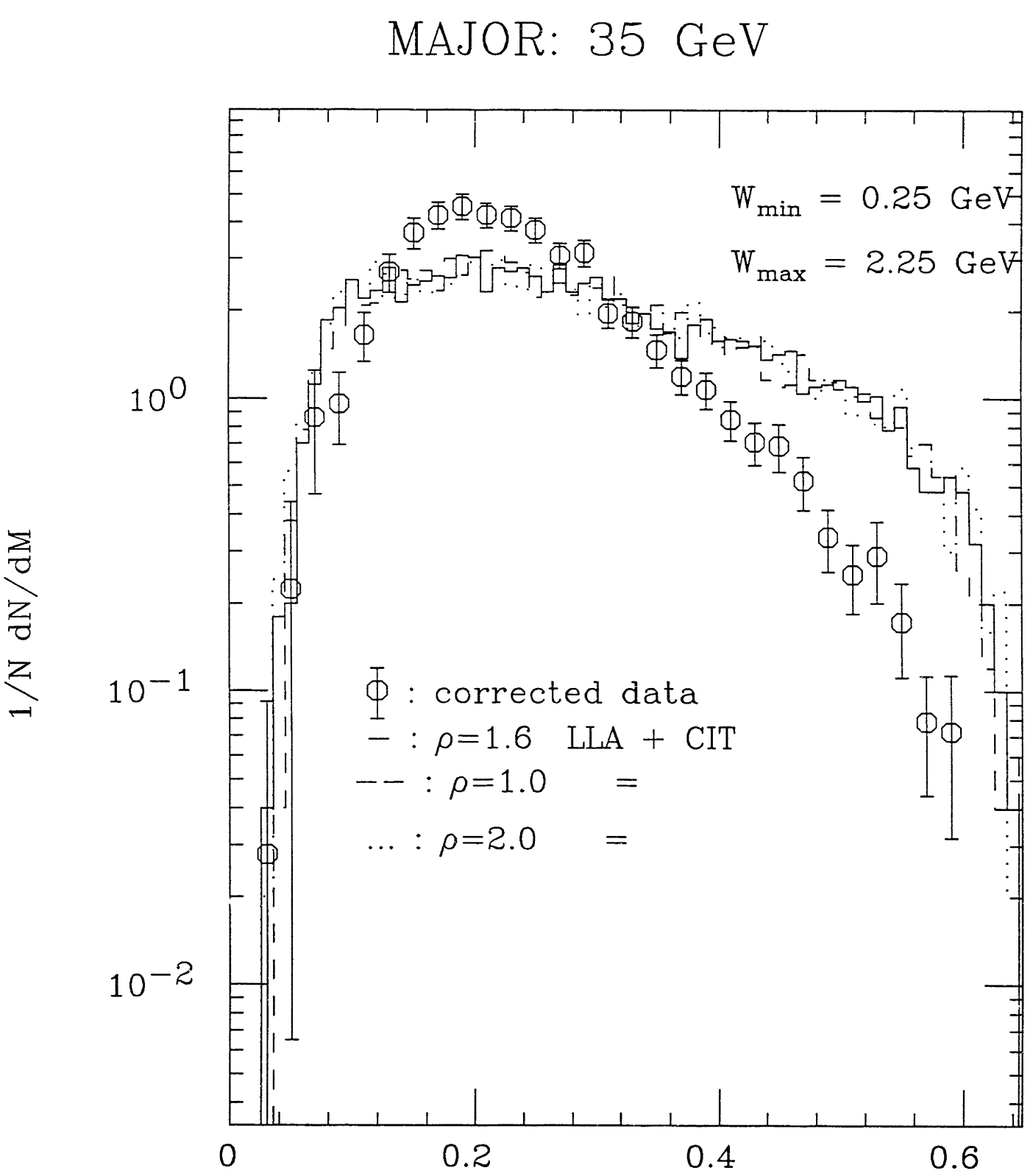
MAJOR: 35 GeV
W_{min} = 0.25 GeV
W_{max} = 2.25 GeV
1/N dN/dM
10^0
10^{-1}
10^{-2}
: corrected data
: ρ=1.6 LLA + CIT
: ρ=1.0 =
: ρ=2.0 =
0
0.2
0.4
0.6

Figure B.2

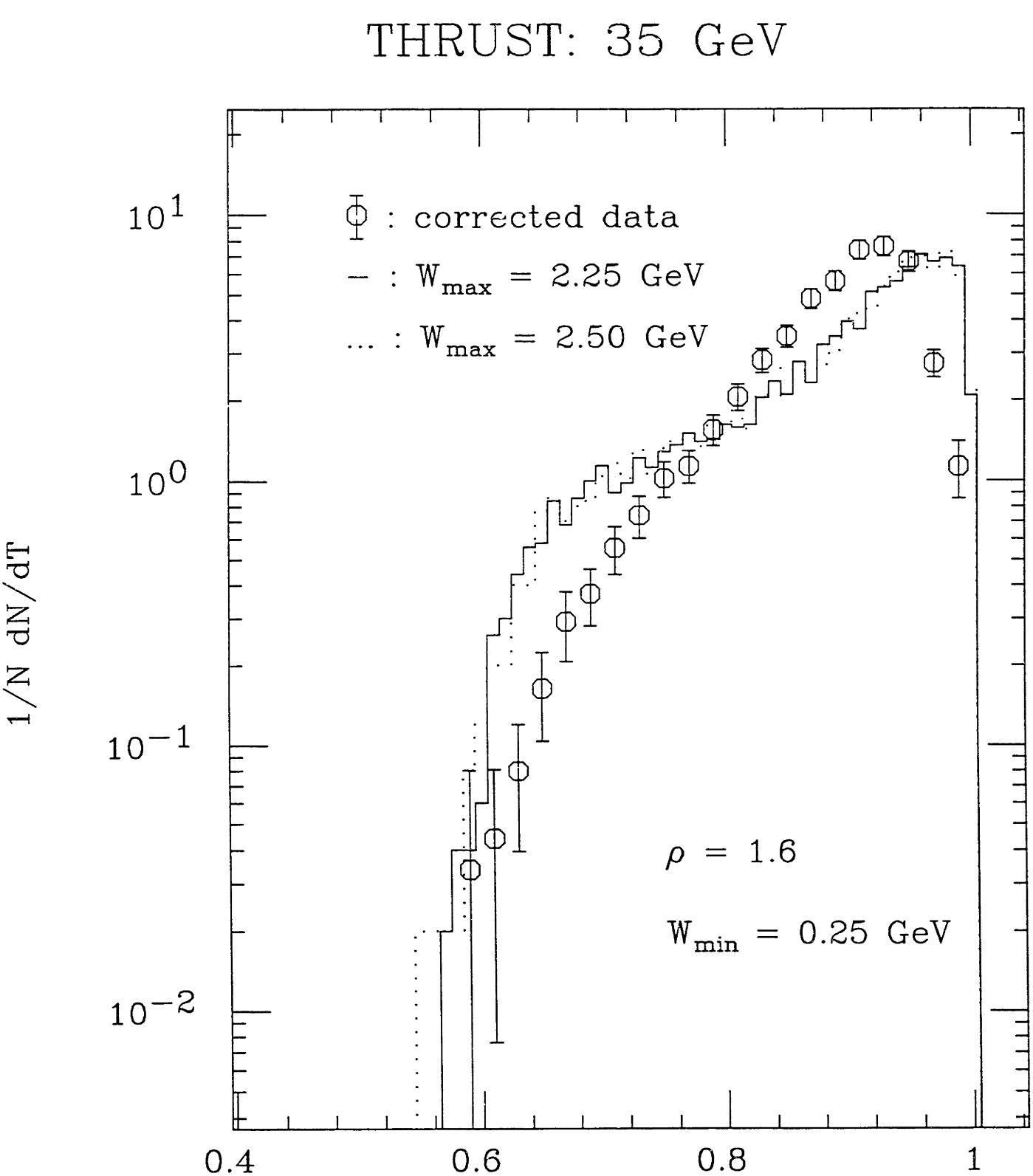
THRUST: 35 GeV
: corrected data
– : W_{max} = 2.25 GeV
... : W_{max} = 2.50 GeV
ρ = 1.6
W_{min} = 0.25 GeV
1/N dN/dT
10^1
10^0
10^{-1}
10^{-2}
0.4
0.6
0.8
1

Figure B.3

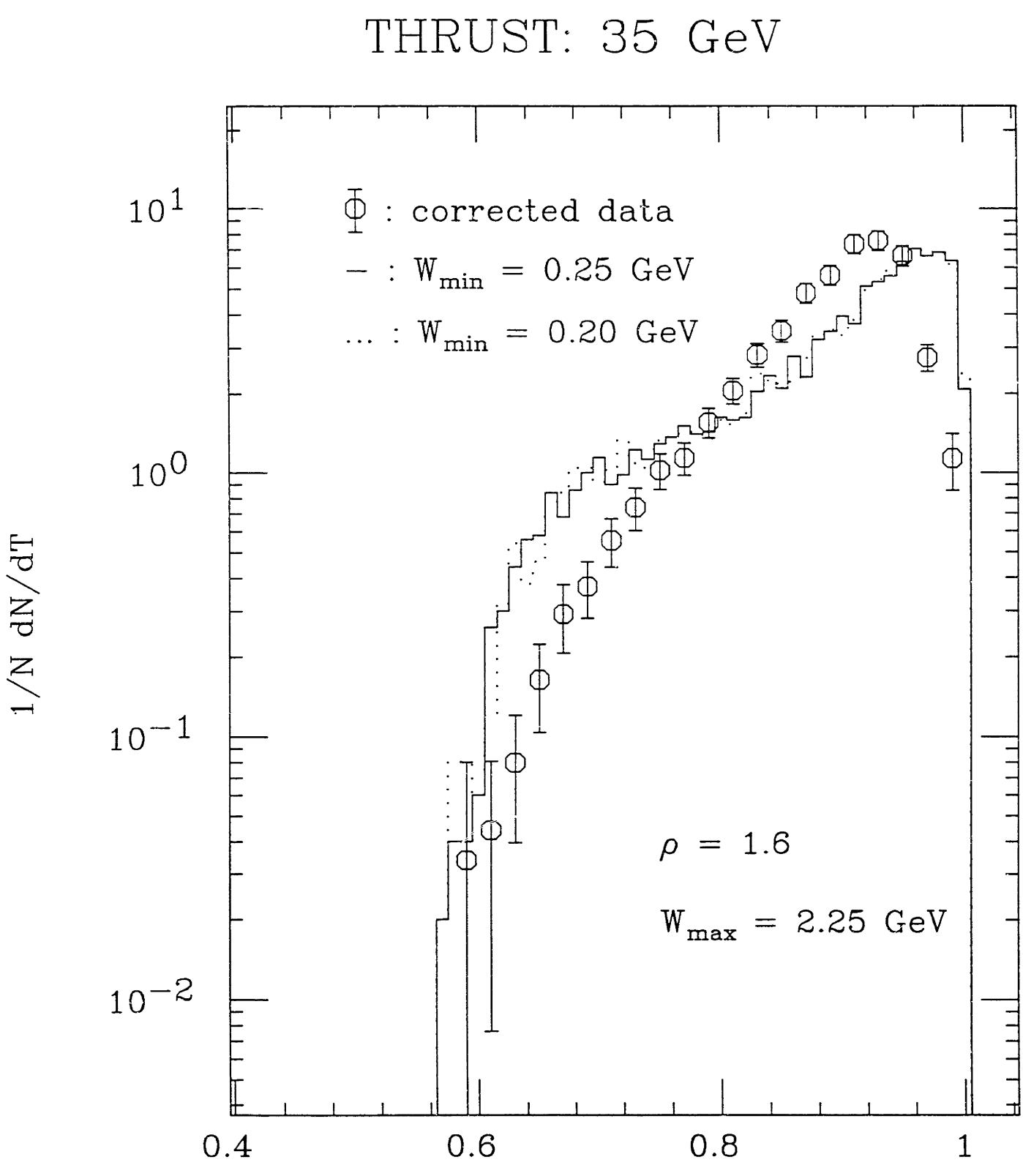
THRUST: 35 GeV
: corrected data
: W_{min} = 0.25 GeV
... : W_{min} = 0.20 GeV
ρ = 1.6
W_{max} = 2.25 GeV
1/N dN/dT
10^1
10^0
10^{-1}
10^{-2}
0.4
0.6
0.8
1

Figure B.4

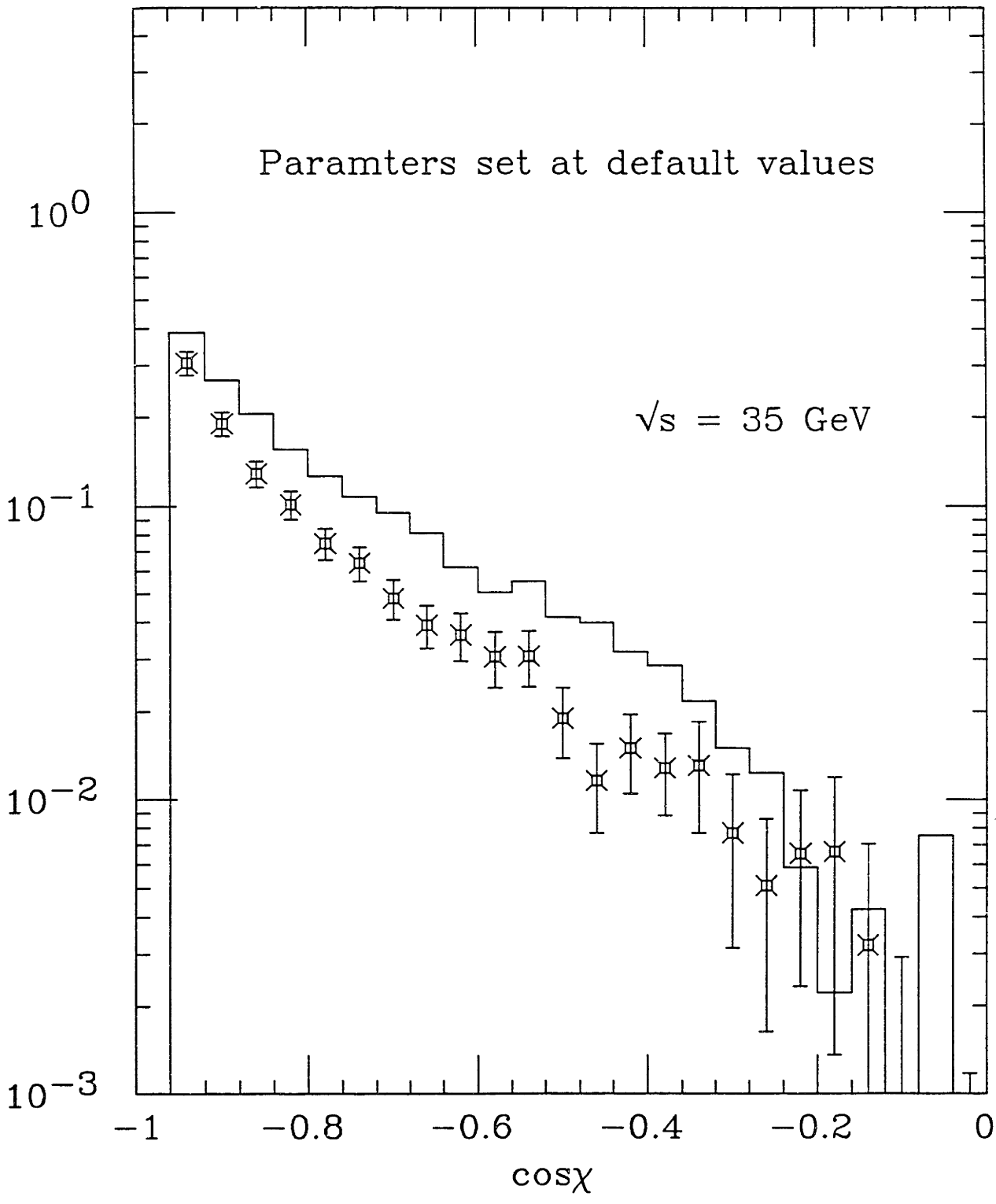

LLA + CIT vs. Corrected data.

Figure B.5

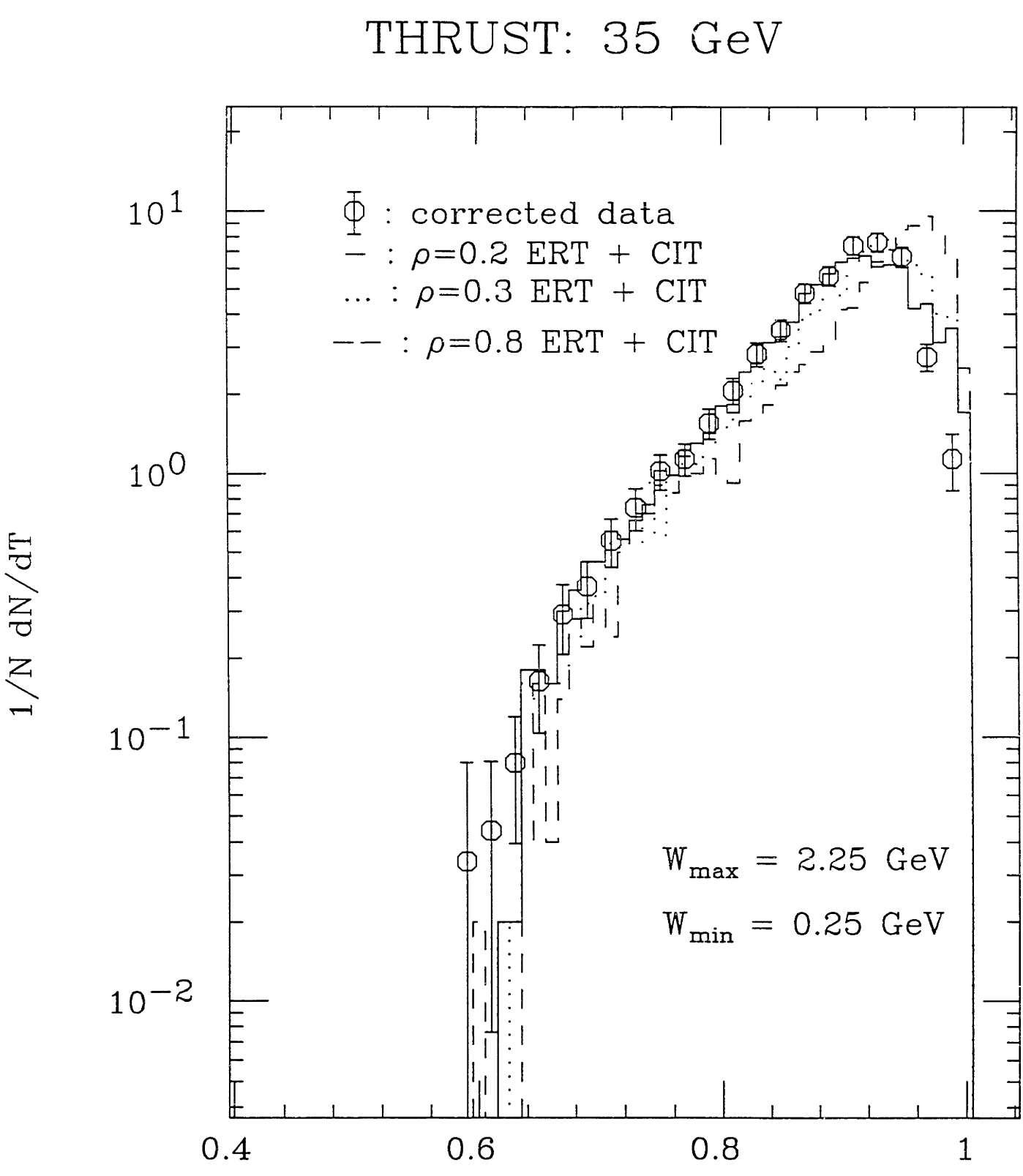
THRUST: 35 GeV
: corrected data
: ρ=0.2 ERT + CIT
: ρ=0.3 ERT + CIT
: ρ=0.8 ERT + CIT
W_max = 2.25 GeV
W_min = 0.25 GeV
1/N dN/dT
10^1
10^0
10^-1
10^-2
0.4
0.6
0.8
1

Figure B.6

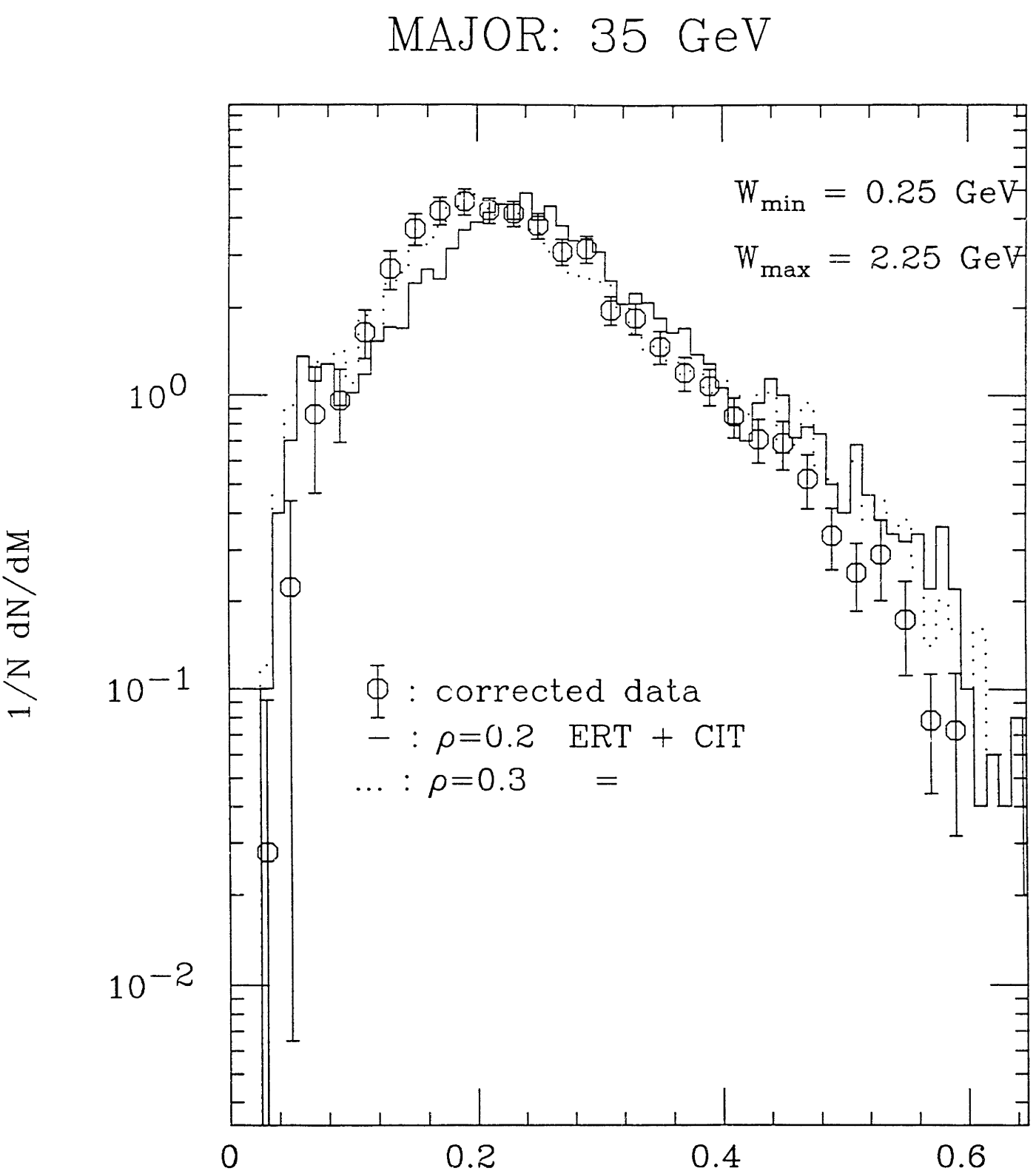
MAJOR: 35 GeV
W_{min} = 0.25 GeV
W_{max} = 2.25 GeV
1/N dN/dM
10^0
10^{-1}
10^{-2}
: corrected data
: ρ=0.2 ERT + CIT
... : ρ=0.3 =
0
0.2
0.4
0.6

Figure B.7

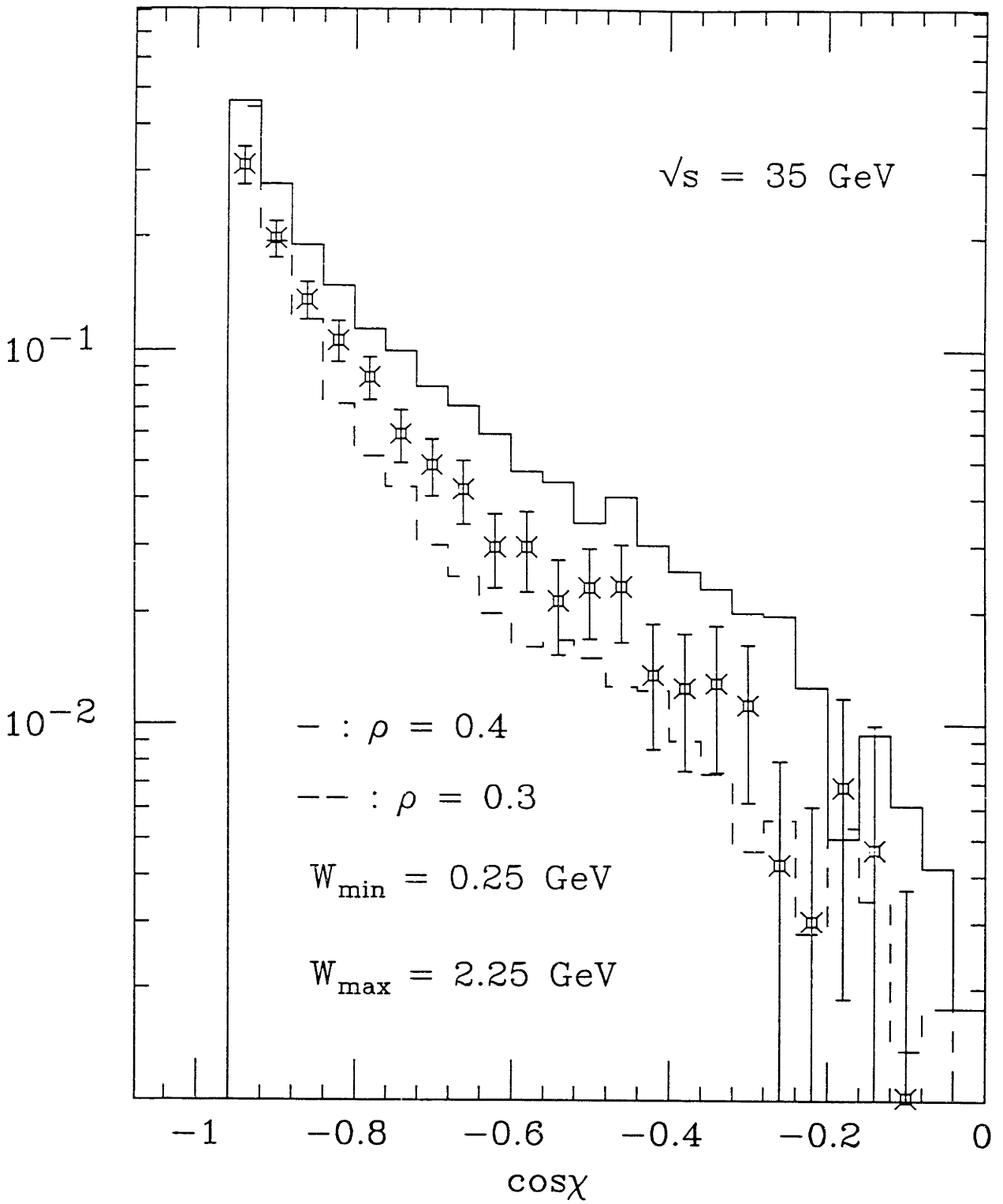

ERT + CIT vs. Corrected data.

Figure B.8

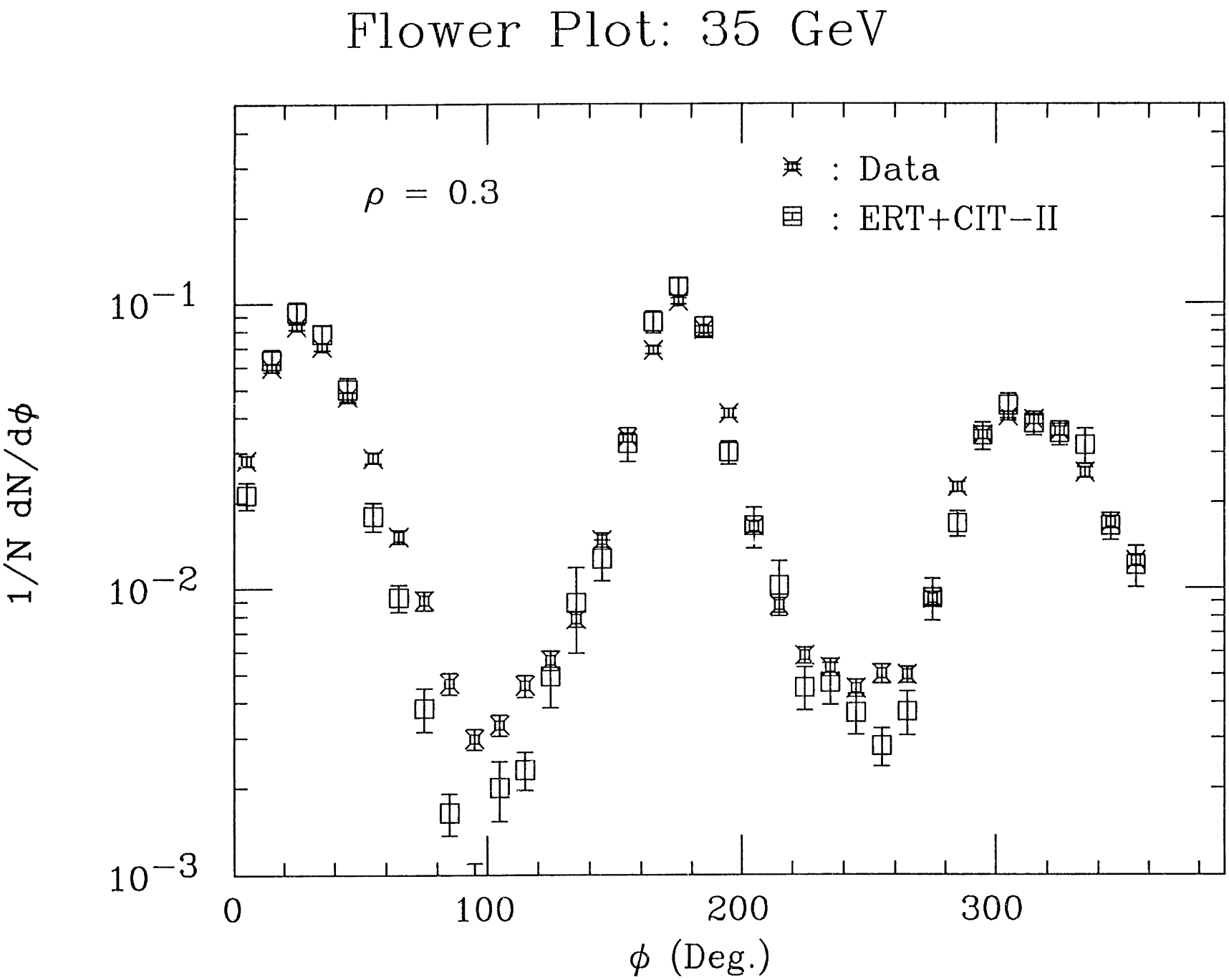
Flower Plot: 35 GeV
ρ = 0.3
: Data
: ERT+CIT−II
1/N dN/dφ
10^−1
10^−2
10^−3
0
100
200
300
φ (Deg.)

Figure B.9